DEVELOPMENT OF PROCESS-BASED MODEL AND NOVEL NANOCOMPOSITE CATION EXCHANGE MEMBRANES FOR SALINITY GRADIENT POWER PRODUCTION

A Dissertation
Presented to
The Academic Faculty

by

Jin Gi Hong

In Partial Fulfillment
of the Requirements for the Degree
Doctor of Philosophy in the
School of Civil and Environmental Engineering

Georgia Institute of Technology
May, 2015

DEVELOPMENT OF PROCESS-BASED MODEL AND NOVEL NANOCOMPOSITE CATION EXCHANGE MEMBRANES FOR SALINITY GRADIENT POWER PRODUCTION

Approved by:

Dr. Yongsheng Chen, Advisor
School of Civil and Environmental Engineering
Georgia Institute of Technology

Dr. Jian Luo
School of Civil and Environmental Engineering
Georgia Institute of Technology

Dr. John Crittenden
School of Civil and Environmental Engineering
Georgia Institute of Technology

Dr. Zhiqun Lin
School of Materials Science and Engineering *Georgia Institute of Technology*

Dr. Ching-Hua Huang
School of Civil and Environmental Engineering
Georgia Institute of Technology

Date Approved: [March 04, 2015]

To the most loving and supportive family anyone could ever have.
Thanks. I love you.

ACKNOWLEDGEMENTS

First of all, I would like to express my deepest gratitude to my thesis advisor, Dr. Yongsheng Chen, who provided the opportunity to pursue this research and lent his valuable assistance throughout my Ph.D. study. All the great help in guiding, teaching, mentoring and encouraging that he provided brought this thesis to fruition. His tremendous support, advice and guidance for my Ph.D. research and career development have been invaluable.

I would also like to thank my committee members Dr. John Crittenden, Dr. Ching-Hua Huang, Dr. Jian Luo, and Dr. Zhiqun Lin for their time and precious comments on my research. Their invaluable advice and discussions were of great help to shape my research.

My special thanks also go to every member in Dr. Chen's group. I would like to thank Dr. Wen Zhang, a former research engineer for his boundless help and feedback. Dr. Kungang Li, my best office mate and friend, for his tremendous help and heartfelt encouragement on my research and personal difficulties. I also appreciate my current office mate and collaborator, Bopeng Zhang for the great atmosphere in the office and discussions on our research. I also thank my former collaborators, Matt Gilstrap, Shira Glabman, and Reynold Curampez. I am also indebted to Dr. Guangxuan Zhu for his support on lab management.

Last but foremost, my biggest thanks and love go to my wife, Min Hee and lovely children, Lauren and Ryan. I also would like to thank my parents and parents-in-law for their support with endless heartfelt prayer and faith in me.

TABLE OF CONTENTS

LIST OF TABLES

LIST OF FIGURES

LIST OF SYMBOLS AND ABBREVIATIONS

a	Effective hydrated ion size
AEM	Anion exchange membrane
b	Width of a cell
CEM	Cation exchange membrane
CD	Charge density
C_S	Saline water concentration
C_F	Freshwater concentration
C_F	Freshwater concentration
D	Diffusion coefficient of an ion
DI water	Deionized water
D_{H2O}	Diffusion coefficient of water
ED	Electrodialysis
EDS	Energy-dispersive X-ray spectroscopy
Fd	Faraday number
F	Fresh water
FCD	Fixed charge density
FTIR	Fourier transform infrared spectroscopy
f	Obstruction factor
IEC	Ion exchange capacity
IEM	Ion exchange membrane
IS	Impedance spectroscopy
L	Length of a cell
OCV	Open circuit voltage

PPO	Poly(2,6-dimethyl-1,4-phenylene oxide)
R	Gas constant
R_{cell}	Total cell resistance
R_{cem}	CEM area resistance
R_{aem}	AEM area resistance
R_{mem}	Membrane resistance
R_{sol}	Resistance in the blank test
RED	Reverse electrodialysis
RO	Reverse osmosis
S	Saline water
SEM	Scanning electron microscopy
SD	Swelling degree
T	Temperature
TEM	Transmission electron microscopy
V_{H2O}	Molar volume of water
z	Valence of an ion
α_{cem}	Permselectivity of CEM
α_{aem}	Permselectivity of AEM
μ	Ionic strength of the solution
γ	Activity coefficient
δ_S, δ_F	Saline water and freshwater compartment thickness
δ_m	Membrane thickness
$\Lambda_{m,S}$	Molar conductivity of salt in saline water
$\Lambda_{m,F}$	Molar conductivity of salt in freshwater
$Ø_S$, $Ø_F$	Flow rates of saline water and freshwater

SUMMARY

Ocean salinity is a renewable energy source that has not been recognized and could provide an opportunity to capture significant amount of clean energy when it mixes with river water. One of the processes emerging as a sustainable method for capturing energy from seawater is reverse electrodialysis (RED), which generates power via the transport of the positive and negative ions in the water through selective ion exchange membranes (IEMs). RED power generation is relatively close to commercialization, but its application is often limited by system power efficiency in natural water conditions. Although various types of salt ions exist in environmental saline water, most efforts have been focused on sodium chloride as a single ionic source in the water and the effects of other common multivalent ions (e.g., magnesium and sulfate) on power generation remain unexplored. Moreover, the commercial feasibility of RED is highly challenged by the absence of specialized RED membranes. Currently available IEMs are not optimized for RED power conversion systems, but successful operation is highly dependent on the membranes used. Major advances in manufacturing of proper IEMs will be a critical pathway to accelerate large-scale energy conversion by RED.

Therefore, this study aimed at advancing our understanding of the RED power system for efficient and stable salinity gradient energy generation. Specifically, it is comprised of three parts. First, a mathematical model is developed for three different monovalent and multivalent ion combinations to determine the effect of different ionic compositions of the feed solution on the power density. Efforts are further made to optimize the RED system with respect to improving power density by investigating the

sensitivity of key response parameters such as flow rate ratios and intermembrane distance ratios. Second, novel organic-inorganic nanocomposite cation exchange membranes (CEMs) are synthesized for RED application by introducing functionalized inorganic materials into an organic polymer matrix. The effect of inorganic particle filler loading within the organic polymer matrix on physico- and electrochemical performance is investigated. The results revealed that the increase of functionalized nanoparticle loading controls the effective ion transport in the membrane structure and there exists an optimum amount of nanoparticles (i.e., charged groups), which performs the best in selectively exchanging counter-ions, while excluding co-ionic species. Third, the membrane structure modification is demonstrated to enhance ion transport while maintaining large surface-charged functional groups in the polymer matrix. We have synthesized custom nanocomposite CEMs to tailor porous membrane structures of various thicknesses, aging (evaporation) time, and inorganic nanoparticle loadings. We have further tailored the membrane structure by incorporating different inorganic particle filler sizes. These engineered design approaches are found to be highly effective in obtaining desired physico- and electrochemical properties, which allowed higher ionic current flow throughout the system. Furthermore, for the first time we showed the successful application of tailor-made nanocomposite CEMs in a RED stack and achieved superb power density, which exceeds the power output obtained with the commercially available membranes.

In summary, this dissertation has advanced our understanding of salinity gradient energy generation using RED technique. Specifically, computational modeling and simulation study investigates the development and optimization approaches of the RED

process for practical application of RED using natural water conditions. Furthermore, the RED membranes developed in this dissertation focuses on fabrication, characterization, and optimization of cation exchange membranes. Overall, the results of this study are anticipated to benefit the future optimization of energy-capturing mechanisms in RED and provide the better pathway for the sustainable salinity gradient power generation.

CHAPTER 1

INTRODUCTION

1.1. Background of salinity gradient power generation

The development of renewable and sustainable energy-conversion technology is widely recognized as an important strategy for global energy security and is becoming extremely important due to growing environmental concerns, such as pollution and global warming [1]. The ocean is a largely untapped renewable and clean energy resource. Mixing ocean water with freshwater creates free energy. More specifically, the chemical potential of sea and river water can be converted into electrical energy. The amount of available energy due to the salinity gradient of seawater mixed with river water is equivalent to the energy obtained from a waterfall that is ~270 m high [2, 3]. Salinity gradient energy has become recognized as a nonpolluting and sustainable energy source, and its viability is further assured by the abundance of river and seawater. The worldwide availability of salinity gradient power (SGP) makes it potentially the second-largest marine-based energy source, with an estimated global power production potential of ~2.6 TW [1, 4, 5]. A remarkable aspect of this membrane-based process is that it can also be used as an adequate treatment for excessive salt accumulation, such as that in agricultural irrigation return water and reverse osmosis (RO) reject waters. Proper disposal or utilization of these "leftover" salts has not yet received significant attention [6]. Furthermore, drinking water treatment and desalination processes generate highly concentrated saltwater (i.e., brine) as a by-product. Application of SGP has great potential to solve these salt problems while producing clean and sustainable electrical energy. Salinity gradient

energy remains a large untapped resource, and greater development of an engineered and optimized energy-capturing effort is needed. The two most promising approaches in capturing salinity gradient energy are 1) pressured-retarded osmosis (PRO), a membrane technology using semi-permeable membranes and 2) reverse electrodialysis (RED), which uses ion exchange membranes (IEMs). Each of these technologies is used in different salinity conditions. For example, mixing concentrated brines is suitable for PRO, and mixing sea and river water is favorable for RED [7]. Another possible salinity gradient energy source is obtainable by incorporating wastewater effluent with brines discharged from desalination plants; however, this technology needs more membrane and system optimization.

1.2. Principle of reverse electrodialysis (RED)

One of the most promising methods to capture salinity gradient energy is reverse electrodialysis (RED)[8-10], which generates power via the transport of the positive and negative ions in the water through selective ion exchange membranes (IEMs). RED is the inverse process of electrodialysis (ED). Unlike ED desalination process where a voltage is applied to produce freshwater through ion exchange process, RED utilizes salinity gradient to produce voltage (Figure 1.1). Thus, the device for ED and RED are similar, which typically consists of an alternating series of anion exchange membranes (AEMs) and cation exchange membranes (CEMs), as shown in Figure 1.2. The principle of ED was first demonstrated in 1890 by Maigrot and Sabates with the initial aim of demineralizing sugar syrup [11]. The principle of RED was first developed in 1954 by Pattle, who proved that mixing river water with seawater can be used as a power source [3].

Weinstein *et al*. proved RED power generation feasible by using a simple mathematical model that emphasized the importance of manufacturing RED IEMs and optimizing their operating conditions to advance RED technology for large-scale energy conversion [4]. In 1980, Lacey [12] concluded that membranes with low electrical resistance and high selectivity are necessary to maximize the net output voltage from RED cells. Lacey also stated that RED membranes should be durable, physically strong, and dimensionally stable for the lowest possible cost [12]. Jagur-Grodzinski *et al*. investigated the role of flow control using spacer patterns to generate higher power [13]. In 2007, Turek and Bandura [14] noted that the membrane size with shorter length, but wider width (i.e., shorter ionic flow path) results in more effective energy production in the industrial unit.

Daniilidis *et al.* [15] also emphasized that affordable membrane cost in combination with power performance is the key to successful RED commercialization. The current cost of IEMs is 2-3 times higher than reverse osmosis (RO) membranes used in desalination processes [2, 16]. However, cost reduction is possible as global demand increases. In the last decade, RO membranes have had a notable cost reduction owing to significant development in membrane materials and fabrication methods, resulting in an increased use of RO for water desalination application. Likewise, proper IEM development for RED is necessary to promote stable power generation in an RED cell.

A typical RED device consists of an alternating series of anion exchange membranes (AEMs) and cation exchange membranes (CEMs), as shown in Figure 1.2. Woven fabric spacers separate these membranes, forming thin compartments and fixing the intermembrane distance. In a RED, a highly concentrated salt solution (e.g., seawater) and a dilute salt solution (e.g., river water) are brought into contact through arrays of

polymeric AEMs and CEMs; this contact directly generates an electrochemical potential gradient. For the RED setting in Figure 1.2, the salinity difference between the two adjacent compartments drives cations toward the cathode and generate a positive potential on left side of the stack, where anions move in the opposite direction toward the anode and also cause a positive potential on the left side of the stack. The salinity gradient for seawater and river water results in a potential difference of 80-100 mV over each membrane. Thus, the total electric potential difference between the outer compartments of the RED cell is the sum of the potential differences over each membrane. At the electrodes, the ionic potential accumulates and induce electronic current via redox reactions [17, 18]. In this study, a homogeneous $K_4Fe(CN)_6/K_3Fe(CN)_6$ redox couple was selected, because it causes no net chemical reactions and thus the power losses are low. The ferricyanide ion reduces at the cathode and the ferrocyanide ion reoxidizes at the anodes as follows:

Cathode: $Fe(CN)_6^{3-} + e^- \rightarrow Fe(CN)_6^{4-}$ (1)

Anode: $Fe(CN)_6^{4-} \rightarrow Fe(CN)_6^{3-} + e^-$ (2)

To facilitate electroneutrality, electrons transfer from anode to cathode through an external electric circuit and generate power when an energy consumer (e.g., light bulb) is connected to the circuit.

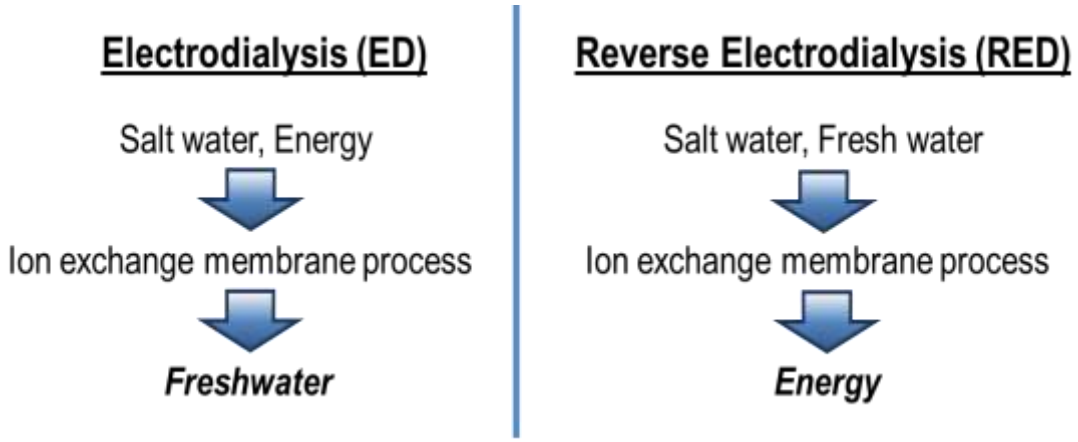

Figure 1.1. Simplified scheme flow for ED and RED processes.

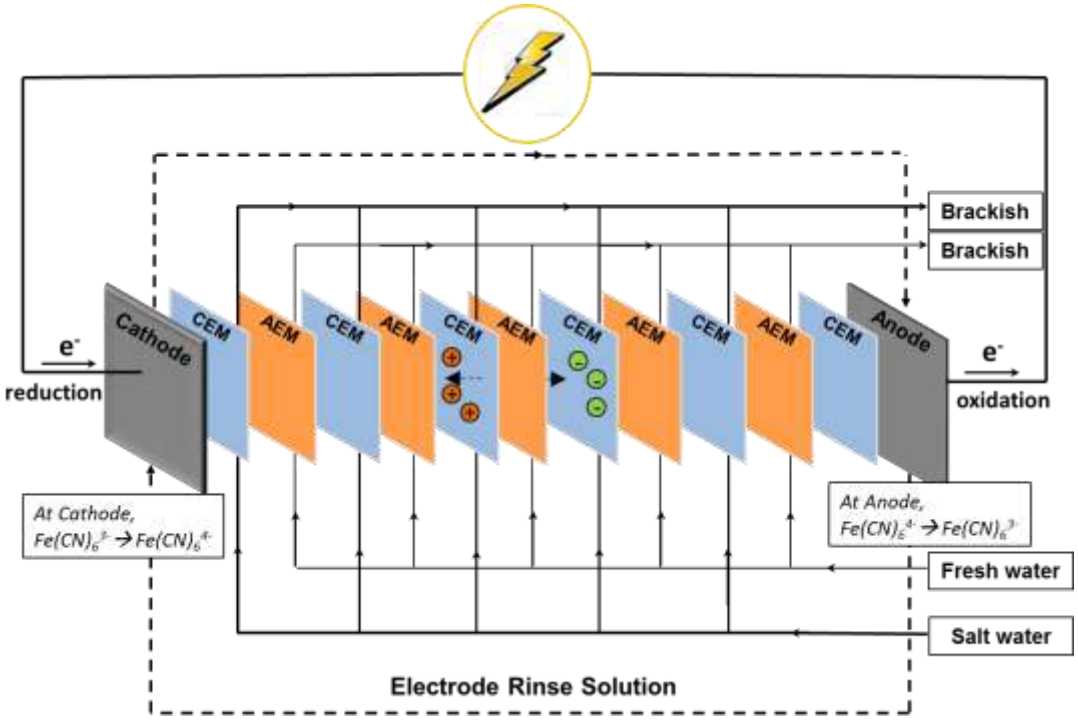

Figure 1.2. Simplified schematic view of an RED stack representing the fluid transport through the IEMs.

1.3. Natural salinity environments

Although RED has been investigated for more than 60 years [3], some challenges are associated with its application in natural water conditions. RED research has primarily focused on maximizing the power density and power efficiency by varying physical properties (e.g., membranes and spacers), structural or stack design, and operating conditions (e.g., residence time and electrical load). In most of the reported RED studies, sodium chloride was the only salt present in the saline water source used to create the salinity gradient [7, 9, 10, 17-25]. However, various types of salt ions exist in environmental saline water, including magnesium, calcium, sulfate, and bicarbonate (Table 1.1). There has been only very limited studies reported on the effect of other salts than NaCl for the RED power generation. Although a few studies have taken into account the presence of multivalent ions, they have tested salts that are majorly present in brines or Dead Sea water. For example, Lacey *et al*. investigated the behavior of multivalent ions such as ferrous iron, manganese, borates, and silicates in RED system [12]. He indicated that those multivalent ions may block the movement of preferred charged-ions, which would result negative impact on membrane permselectivity and resistance. Jagur-Grodzinski and Kramer tested CEMs with simulated Dead Sea water containing high concentrated magnesium solutions and observed significant increase of membrane resistance under magnesium rich solution. Moreover, Audinos also noted that the RED performs better with pure NaCl solutions than with multivalent ionic solutions such as zinc sulfates [26]. Finally, Post *et al*. showed experimentally that the presence of magnesium and sulfate in the feed solution has significant lowering effect on voltage generation due to higher membrane resistances [27]. The study that suggests proper approach for improving such

detrimental effect due to common multivalent ions of natural seawater is still rare. Thus, a process-based mathematical model that considers the key elements of RED system (e.g., electromotive force, internal stack resistance, salt and water flux, and concentration gradient) needs to be developed to evaluate the performance of multi-ionic salt solutions (monovalent and divalent ions) in an RED system.

Table 1.1. The composition of average seawater and river water.

Element	Seawater (mM)	River water (mM)
Na	468.0	0.26
Mg	53.1	0.17
Ca	10.3	0.38
K	10.2	0.07
Sr	0.09	-
Cl	546.0	0.22
SO_4^{2-}	28.2	0.11
HCO^{3-}	2.39	0.96
Br	0.84	-

1.4. Development of RED membranes

Another consideration for RED to become practical is the development of an RED-specific membrane. Currently available IEMs are not optimized for RED, whereas successful RED operation depends on the used IEMs. IEMs have attracted great interest and much research across fields including the bioindustries (food, pharmaceuticals, and biotechnology) [28-30], fuel cells [31-33], and desalination [34, 35]. Each application normally requires the membranes to have physical and electrochemical properties optimized to the specific situation. As in many other membrane processes, the membrane characteristics will primarily determine the performance in an RED system. In most reported RED studies, various commercially available membranes were tested (Table 1.2) and evaluated within an RED stack [9, 10, 21, 24, 36], but relatively little is known about the key membrane properties that determine membrane performance in power generation via RED. Recently, some efforts have been reported on designing RED IEMs showing the potential of IEM development for viable energy production [37-40]. The studies have focused on investigating the core electrochemical and physical properties of IEMs that directly influence RED performance. Recent efforts have made a valuable contribution in providing some insights of the key performance-determining membrane properties in RED stack. They have concluded that the development of RED-specific membranes with low electrical resistance and high selectivity is necessary [4, 12, 25, 41, 42]. Such conclusion aligns with its theoretical correlation of the power density with electrical resistance and permselectivity based on Nernst equation. However, it remains challenging to tailor membranes with such properties and dependency of the experimentally obtained power output on those properties often is not as straightforward as predicted by the theoretical

equation [43, 44]. Further physico- and electrochemical property analyses (e.g., ion exchange capacity, permselectivity, and resistance) are still needed for greater variety of membranes that are prepared with different methods and materials to be able to relate these properties to real power density generation. Therefore, it is worthwhile to investigate the key membrane properties necessary to maximize overall RED performance both to advance our understanding and to take steps toward the development of RED-specific membranes optimized for power generation.

Table 1.2. Properties of commercially available IEMs.

Membrane Product	IEC (meq g_{dry}^{-1})	Permselectivity (%) [a]	Resistance (Ω cm^2) [b]	Swelling degree (%)	Ref.
Cation Ion Exchange Membranes					
Homogeneous					
Fumasep® FKD	1.14	89.5	2.14	29	[8]
Fumasep® FKS	1.54	94.2	1.5	13.5	[42]
Qianqiu CEM	1.21	82.0	1.97	33.0	[42]
Neosepta® CMX	1.62	99.0	2.91	18	[25]
Neosepta® CMX	1.5-1.8	97	1.8-3.8	25-30	[45]
Selemion® CMV	2.0-2.4	95.0-98.8	2.3-2.9	20-25	[25, 45]
0.7wt% Fe_2O_3-SO_4^{2-} sPPO	1.40	87.7	0.97	26	[37]
SPEEK 40	1.23	95.3	2.05	23	[42]
SPEEK 65	1.76	89.1	1.22	35.6	[42]
JJC-82		99.6	3.1		[13]
Heterogeneous					
Ralex® CMH-PES	2.34	94.7	11.33	31	[25]
Anion Exchange Membranes					
Homogeneous					
Fumasep® FAD	1.42	86.0	0.89	34	[25; 42]
Neosepta® ACS	1.4-2.0	-	2.0-2.5	20-30	[46]
Neosepta® AMV	1.78-1.9	87.3	3.15	17.0	[45; 42]
Neosepta® AMX	1.4-1.7	90.7	2.0-3.5	25-30	[46, 47]
Selemion® ASV		97	3.7		[c]
Fumasep® FAS	1.12	89.4	1.03	8.0	[42]
Qianqiu AEM	1.33	86.3	2.85	35.0	[42]
PECH A	1.31	90.3	2.05	32.2	[38]
PECH B-1	1.68	86.5	0.82	49	[38]
PECH B-2	1.68	87.2	0.94	49	[38]
PECH B-3	1.68	87.0	1.32	49.1	[38]
PECH C	1.88	79.2	1.14	53.5	[38]
Heterogeneous					
JJA-72		99	3.0		[13]
Ralex® AMH-PES	1.97	89.3	7.66	56	[25]

a. Measured over the membrane between a 0.5 M and a 0.1 M solution
b. Measured in 0.5 M NaCl solution at 25°C
c. Manufacturer's specification

1.4.1. Key properties for RED membranes

There are many properties of IEM that affect its performance and application in the RED system. Essentially, all properties are the overall effect of the type and distribution of bulk material and fixed ion groups within the membrane entity. The study of IEM properties examines how they affect IEM performance under different circumstances [45, 48]. The durability of membrane material and fine physicochemical characteristics are of great importance in many applications. Thermal and chemical stabilities are good indicators of the durability of membranes. Transport related properties, such as swelling degree, permselectivity, ion exchange capacity (IEC), and ionic conductivity influence the electrochemical characteristics. Most of these properties can be determined experimentally. The rest of them can be calculated based on their relationship with other available parameters. It should be noted that the requirement for IEMs in RED applications is different from the requirement for other applications, especially ED applications, because the aim of RED is to generate electrical energy instead of separating substances as in ED [49]. Thus, ionic resistance and permselectivity are the most crucial properties while others that are not related to these two properties weigh less in RED power generation.

Thermal stability. The thermal stability of IEM depends on the crosslinking degree, thermal stability of inert polymers, and reinforcing fabric (e.g., poly(vinyl) chloride and polyethylene). The size of the counter-ion also affects the thermal stability of the membrane [50]. In general, the requirements ensuring thermal stability of IEMs used in RED are not high when compared to thermal stability requirements for more common

devices such as fuel cells [51]. The common temperature used for RED systems is generally around room temperature with a possible seasonal variation within 30 K.

Chemical stability. The chemical stability depends on the durability of the membrane in various acidic or alkaline solutions. In general, CEMs are more durable than AEMs in terms of both thermal stability and chemical stability in strongly acidic and strongly alkaline solutions because the quaternary ammonium groups in AEMs tend to decompose at elevated temperature and in concentrated alkali solutions [48, 52]. Chemical stability is important for ED processes because the electricity applied to the system would inevitably dissociate water molecules and generate proton and hydroxyl ions [53]. In specific ED application, such as acid and base manufacturing, the pH change in a solution flow by IEMs is significant. The chemical stability of IEMs to withstand harsh pH environments is important. In addition, the current density applied in most ED processes will often approach the limiting current density or even reach the over-limit current density range in order to achieve highest possible reaction rate. The high electrical field in the membrane bulk exerts a relatively strong force onto fixed charges. It is thus crucial to have a high stability of fixed charge groups in the membrane bulk [54]. In the case of RED application, the dissociation of water is limited to a negligible extent on the electrodes, so that pH of the rinse solution is expected to be stable. Feeding solutions (river and salt water) are close to neutral, and no significant process would alter or interfere with the pH throughout the residence time of the solution in each compartment. Consequently, the chemical stability of IEMs is not crucial in RED application [38, 45].

Mechanical strength. Membrane mechanical strength is necessary to maintain good durability under the flow of feed solutions creating hydraulic pressure over the membrane

in addition to the osmotic pressure caused by concentration gradient. However, in typical seawater/river water cases, the concentration difference is in the range of 0.01 M to 0.5 M (a bit over an order range). Some ED processing may encounter a gradient of several orders (e.g., deionization). The osmotic pressure exerted onto the membrane is quite different. On the other hand, the mechanical strength of the membrane is not as crucial in the RED system when compared with the PRO technique. In the latter case, membranes have to withstand tremendous hydraulic pressure given a water flux of 20-50 L m^{-2} h^{-1} [55].

Swelling degree. The swelling degree of the membrane is usually expressed as water content or water uptake of the membrane under a given condition. The swelling degree is dependent on the nature of the membrane structure and material as well as the outer solution condition [45, 56]. IEC represents the number of fixed charges on the membrane in a unit of membrane dry weight. Most CEMs incorporate sulfonic acid (–SO_3^{2-}) or carboxylic acid groups (-COO^-) in the membrane structure, while ammonium groups (–NR_3^+, –NH_4^+, –NH_2, =NH, ≡N) are common in AEMs. The type and distribution of these ion exchange groups classify different membranes. The IEC of IEMs are usually determined experimentally according to the titration method using a strong acid or base of HCl for CEMs and NaOH for AEMs, respectively.

Swelling is usually considered to be an adverse effect because it tends to decrease the permselectivity of ion exchange membranes, but it also decreases the membrane resistance in certain cases, especially for anion exchange membranes [25, 57, 58]. For applications such as RED, the loss of permselectivity may not be an adverse effect if a much lower resistance is achieved. For example, Geise *et al.* [57] made AEMs based on poly(phenylene oxide) and poly(sulfone) polymers. High swelling degrees led to

increases in resistance of more than three orders of magnitude, while the permselectivity decreased by only 6%. As will be discussed in the following section, the effect of the decrease of permselectivity on power output would be negligible because power density will increase significantly with a significantly lowered resistance.

Ion exchange capacity (IEC). A high IEC indicates more ion exchange groups in the membrane bulk, but swelling tends to dilute the concentration of these groups as distance between these ion exchange groups increase when the membrane is immersed in a solution. Therefore, the ratio of IEC and swelling degree, termed as the fixed charge density (or fixed ion concentration), depicts the overall effect of the swelling degree on IEC and provides a direct relationship between the two electrochemical properties of an IEM [25, 59]. The fixed charge density (meq g $_{H_2O}^{-1}$) is defined in equation (1) if the IEC and water uptake of a membrane are known [25, 42, 48]:

$$FCD = \frac{IEC}{w_u} \tag{1}$$

where *FCD* is the fixed charge density, and w_u is the water uptake.

The advantage of using fixed charge density is easily seen when IEC and water content do not change simultaneously. For example, increased IEC is reported to result in higher permselectivity of IEMs [60]; however, the water content in the membrane phase may vary under different solution concentrations due to osmosis deswelling and the decrease of free volume in the membrane phase [61]. As a result, the final membrane may exhibit lower permselectivity with the same IEC because its final fixed charge density is lower. This deswelling effect on the membrane is more pronounced in AEMs than in CEMs [25, 57, 61, 62].

Ionic resistance. Because the RED system is essentially a dialytic battery, the ionic resistance (or ionic conductivity since ions are actually conducting electricity) of an RED system is analogous to the internal resistance of a battery. As a major part of this internal resistance, the ionic resistance of IEM in the RED system is usually measured experimentally. Similar to the internal resistance of a battery, the ionic resistance determines the energy loss in an operating stack, which affects the power output of the system [25, 63]. The determination of membrane resistance is not straightforward because the measurement is usually taken while the membrane is in a solution as encountered in power generation applications. The ionic resistance of membranes is commonly measured using indirect methods (no direct contact of the electrodes and the membrane) in RED research [8, 25, 63-65]. The alternative current (AC) is preferable because it avoids electro-chemical reactions that may occur during measurement and is more accurate in differentiating the pure membrane resistance from common resistance, including the diffusion boundary layer (DBL) and double-layer effects. Direct current (DC) is also reported to be useful in the resistance measurement [63, 65, 66]. The membranes to be measured are immersed in sodium chloride or potassium chloride solutions of concentrations of 0.5 M or 1.0 M; however, the resistance may change with different external solutions and under different temperatures [48, 64]. In RED application, IEMs divide salt solutions of different concentrations. As a result, the apparent membrane resistance is significantly different from the measured value in a 0.5 M NaCl solution [64, 67]. Therefore, a more comprehensive measurement of membrane resistance considering the effect of the external solution concentration is critical in modeling the RED system. Two techniques, namely chronopotentiometry and electrochemical impedance

spectroscopy (EIS), have been used to solve the aforementioned difficulties during the membrane resistance measurement.

Chronopotentiometry is widely used to investigate kinetic effects and adsorption during the transport process in IEMs [68, 69]. Through chronopotentiometry studies, the time dependence of the concentration gradients and the thickness of DBL under different current density can be determined. Also, the validity of the Nernst-Planck equation and the Donnan theory are also confirmed under transient conditions [68, 70]; however, for measuring the double layer and quantifying its electrochemical effect on the membrane, chronopotentiometry is not sufficient.

EIS is a technique used for studying and characterizing the electrical properties of porous materials and can be used to characterize IEMs. EIS provides another perspective in the study of the IEM system by equating the system to an electrical circuit with capacitors and resistors [71, 72]. The existence of three sub-layers of the IEM system, including the membrane, the electrical double layers, and the DBLs, has been studied using the EIS technique, and the quantitative circuit model has been established [71]. By changing the frequency of the applied AC potential, the resistance of the solution and the electrical double layer can be differentiated [45, 65]. For example, when the applied AC frequency is low or when DC is applied to the membrane system, the resulting electrical equivalent circuit indicates the effect of the diffusion layer and the electrical double layers as well as their contribution to the total electrical resistance of the system. Finally, an analysis under a high frequency AC reveals the resistance attributed to the membrane polymer itself [73].

Permselectivity. Permselectivity describes the ability of a membrane to prevent co-ions from passing through the membrane. It is measured by transport number and related to the fixed charge concentration of the membrane and the external solution concentration. Theoretically, a perfect IEM would have a permselectivity of one when the complete exclusion of the co-ions from the membrane is achieved; however, according to Donnan's theory, a certain amount of co-ions could contribute to the transport current [62, 74]. Thus, the permselectivity would decrease below the ideal value of 1 as the solution concentration increases [48].

In practice, the apparent permselectivity is of more concern in RED because it determines the membrane potential (E_m) achievable under the given circumstances according to the following equation [75]:

$$E_m = \alpha_m \frac{RT}{F} \ln\left(\frac{\alpha_c}{\alpha_d}\right) \quad (2)$$

where α_m is the apparent membrane permselectivity, R is the gas constant (J mol^{-1} K^{-1}), T is the absolute temperature (K), F is the Faraday constant (C mol^{-1}), α_c is the activity (mol L^{-1}) of the concentrated salt solution, and α_d is the activity (mol L^{-1}) of the diluted salt solution.

The relationship between the permselectivity and the ionic resistance of the membrane is complicated because of the interactive effects from fixed charged groups and membrane swelling. Some researchers have concluded that it is not necessary to achieve both high permselectivity and low ionic resistance because an RED system can tolerate moderate permselectivity. After all, the main goal is to produce electricity and not to separate solutions [25]. The requirement of membrane resistance is stricter for an RED application than an ED application because the improvement of membrane

conductivity is a step in the process of optimization; however, efficiency is the major hurdle that a successful RED application must overcome. Thus, membrane resistance is central to this hurdle because it is the key parameter that determines system efficiency. On the other hand, the permselectivity is more important in the ED process, especially for continuous deionization in which the purity of the products is of greater concern [76, 77]. This allows the resistance to be sacrificed to some extent. In summary, the development and synthesis of IEMs with well-balanced permselectivity and low resistance is desirable to optimize the RED salinity gradient power generation process [57].

1.4.2. Preparation of ion exchange membranes

IEM determine the energy efficiency of a RED system, making membranes one of the most important components. IEMs contain negatively or positively charged groups, which are attached to the membrane backbone and discriminate between cations and anions. CEMs allow cations and exclude anions, and AEMs allow anions and exclude cations. In general, fewer steps are required to manufacture CEMs than AEMs [48, 78, 79]. For cation exchange materials, fixed ionic groups can be appended by acidic functional groups to give cation character to the membrane. The most common acidic functional groups are carboxylic and sulfonic groups, but phosphonic acid and phosphoric acid groups are also being investigated. The carboxylation process often involves the radiation grafting of either acrylic acid or methacrylic acids onto polymer films [80-82]. Carboxylic groups can be introduced by radiation-induced grafting of epoxy acrylate monomers followed by the subsequent conversion of an epoxy group to a carboxylic group by a ring opening reaction [83]. Sulfonation is another common chemical modification of base

polymers for various membrane processes such as water filtration, diffusion dialysis, electrodialysis, and water cleavage [84]. The sulfonation process is an electrophilic substitution that normally takes place on the aromatic ring to increase the desired charge density and the hydrophilicity of the polymer matrix. By enhancing the ionic charge transfer, this modification facilitates good electrical conductivity [85]. Typical sulfonating agents, such as sulfuric acid or chlorosulfonic acid, are often used for this treatment.

Of the existing polymeric materials for manufacturing CEMs, the perfluorinated or partially fluorinated materials are most frequently used in commercial applications. For example, Nafion® is the most commonly used perfluorosulfonic membrane in fuel cell technology. Although the Nafion® membrane has a high water selectivity and ion exchange capacity, it often presents poor conductivity. Moreover, adverse safety concerns and its high cost prevent its widespread application. The high cost stems from the fluorochemistry involved in the synthesis of perfluorosulfonic materials. Thus, omitting the fluorinate species in the polymer matrix (i.e., non-fluorinated) can significantly decrease the cost of manufacturing IEMs. Consequently, non-fluorinated hydrocarbons are often considered to be an alternative material [86]. Moreover, as for membrane performance, fluorinated materials show good thermal and chemical stability and mechanical properties; however, for the RED process, the thermal and chemical stability and mechanical properties of IEMs are not very crucial. Thus, the use of non-fluorinated hydrocarbon materials for the production of IEMs may be a promising option to lower the cost of the membranes and to retain the high performance of the fluorinated materials. As mentioned previously, the functionalization of non-fluorinated polymers can be readily used for ion exchange in the RED system. For example, Guler *et al.* [42]

investigated the bulk membrane properties of tailor-made membranes. For the synthesis of tailor-made CEMs, a non-fluorinated thermoplastic polymer, sulfonated polyetheretherketone (SPEEK), was used. Tailor-made CEMs under different sulfonation degrees performed well in the RED stack, producing excellent electrochemical properties and high power output.

A number of studies and various approaches have proposed methods for preparing AEMs to combine with the desired cationic moieties. The cationic moieties in the membrane can be introduced either prior to dissolving a polymer for casting the membrane or after dissolving a polymer for casting the membrane. Typical chemical modifications of polymer films for the preparation of AEMs usually consist of two steps: a chloromethylation followed by quaternary amination. Prior to the quaternary ammonium functionalization reaction, the polymer film can be modified by direct or indirect grafting of vinyl monomers (e.g., sodium p-styrene sulfonate) to introduce ionic characteristics. The commonly used chloromethyl methyl ether during the chloromethylation has some drawbacks; it is a highly toxic and carcinogenic reagent with a potential risk to human health, and it is difficult to control the position and the quantity of the methyl groups [87]. Several studies have avoided the use of chloromethyl methyl ether in preparing AEMs. The use of *N*-bromosuccinimide (NBS) as the halomethylation agent for bromomethylation [88] or para-formaldehyde and the use of concentrated hydrochloric acid as the chloromethylating agent for chloromethylation [89] were considered for use with methyl-containing polymers (e.g., polyepichlorohydrin (PECH), polysulfone, and polyphenylene) to be a safer and more controllable treatment. Direct grafting copolymerization of pyridine or vinylbenzylchloride onto polymer films or

copolymerization with other monomers could also serve as alternative routes to prepare AEM with a subsequent quaternary amination reaction [90, 91].

The quaternary ammonium functionalization groups can be grafted as charge carriers onto the polymer backbone by using either strongly basic (e.g., tertiary ammonium) or weakly basic (e.g., primary, secondary or tertiary amine) groups. The cast membranes are often immersed into an appropriate functionalizing agent for quaternization; however, the quaternization of the dried (cast) membranes limits the degree of desired functionality [87]. Zhao *et al.* [87] used a more quantitative method of quaternization to prepare the alkaline AEMs. Instead of quaternizing the membranes in the solid state, the homogeneous amination method was used by adjusting the addition of trimethylamine (TMA), which is an aminating agent. The homogeneous amination method can achieve good results in a more controllable and selective fashion. This quaternization method has been optimized to work faster and easier in controlling the degree of functionalization, resulting in an improved selectivity and IEC of the membrane.

In order to obtain the required mechanical and chemical stability of a functionalized polymer, the crosslinking reaction is critical; however, the use of excess crosslinking often decreases the ionic conductivity of the membranes [92]. Increasing the degree of crosslinking narrows the path of ion transport in the membrane, which can lead to poor ionic conductivities. Thus, the addition of crosslinking should be optimized depending on the polymers and applications. In addition, the application of tertiary diamines biquaternization should also be considered. Komkova *et al.* [85] treated the AEM casting solution with diamines to introduce positively charged groups into the polymer (i.e.,

monoquaternization) and to carry out a crosslinking reaction (i.e., bi-quaternization); however, it is important to note that the type and the amount of the quaternization agent (or crosslinker) applied in the AEM preparation should be optimized to obtain desirable electrochemical properties specific to RED application. In general, an excess of diamines is preferable with a short chain length of alkyl groups to achieve high permselectivity and low membrane resistance [93], but an excess of diamines with a long aliphatic chain of the alkyl groups has exhibited a decrease in IEC and permselectivity and an increase in membrane resistance [85]. Thus, the quaternization and the crosslinking reaction in the case of a long chain of alkyl groups (i.e., bonded to amine nitrogen) requires less diamines to obtain AEMs with a low membrane resistance and a high permselectivity, which is more favorable to the RED system. Note that in this dissertation, we have mainly focused on the preparation and optimization of cation exchange membranes for RED application.

1.4.3. Membrane material: Poly (2,6-dimethyl-1,4-phenylene oxide)

In IEM applications, membrane characteristics are mainly dependent on the amount of charged species groups and their distribution within the membranes [48]. Different properties of commercially available IEMs were investigated in order to evaluate their potential performance under RED conditions by Dlugolecki *et al.* [25]. In this study, membranes were selected based on their low resistance and high selectivity. In general, membranes used in electrochemical systems, such as RED, are characterized based on their IEC, permselectivity, electrical resistance, charge density, and swelling degree [25, 42]. These electrochemical properties are directly affected by their structure (thickness and porosity), the preparation procedure (phase inversion and functionalization), and the

chemical composition of the membranes. An evaluation of the basic properties of the membranes and their interconnectedness is necessary to optimize the performance of IEMs for efficient power generation. At the same time, appropriate membrane materials should also be used to lower the cost of membrane manufacturing. An ongoing challenge in this field is to develop cost-competitive membranes with the desired properties for RED applications. The cost of RED membrane materials is expected to be reduced as the energy conversion system matures.

As previously mentioned, the ideal RED IEMs can be selected based on their electrochemical properties, which are mainly determined by the concentration of mobile ions in the membranes and the mobility of the ions in the membrane phase. Polymer-based IEMs are expected to possess both chemical stability and excellent conductivity when the polymers are incorporated into charged groups. Although, in theory, all IEMs can be used for RED, current commercially available IEMs are not ideal for RED application because they often lack the abilities to enhance power output. The desired membranes should not only possess low resistance and high selectivity but should also be easy to prepare and cost competitive. Therefore, the desired or competitive polymer materials for RED IEM preparation must have several characteristics. First, the polymers should be functionalized easily, making it possible to bind the main chain of the polymer with charged groups. Second, the polymer preparation process should be simple and manageable, meaning they can dissolve at room temperature and will not release toxic substances during membrane preparation. Third, the polymeric materials should be affordable based on the cost of RED membranes and systems in large scale applications according to economies of scale. In this regard, one of the most frequently used low-cost

IEM material (i.e., Poly (2,6-dimethyl-1,4-phenylene oxide)) is selected in this dissertation.

Poly (2,6-dimethyl-1,4-phenylene oxide) (PPO) is a prospective RED membrane material because of its low cost, high film-forming properties, good mechanical, thermal, and chemical stability, low-moisture uptake, and high glass transition temperature [94]. The basic form of PPO consists of an aromatic ring, two methyl groups, and a phenol group (Figure 1.3). The simple structure of PPO allows for various structural modifications. For example, the benzene rings and the methyl groups of the PPO chains can be functionalized through electrophilic or radical substitutions, capping, and coupling. These functionalizations introduce desired charged groups into the PPO polymer matrix, which makes the polymer more adequate for ion exchange. In the case of CEMs, sulfonated PPO (sPPO) is often prepared by functionalizing the aromatic rings of the polymer chains with charged groups, typically from sulfonic acid. sPPOs have been widely used in various industrial applications due to their excellent electrochemical characteristics [81, 95].

In addition to pure PPO-based membranes, PPO-based organic-inorganic hybrid IEMs have also been well-studied for enhanced thermal stability and mechanical strength. It is reported that SiO_2 was blended into PPO through a sol-gel process of the polymer precursors PPO–Si $(OCH_3)_3$ using tetraethoxysilane (TEOS) as the Si source. Also, this membrane was found to possess enhanced hydroxyl (OH^-) conductivity, which is useful for alkaline fuel cells. The membranes exhibited higher swelling-resistant properties, and the hydroxyl ion (OH^-) conductivity values were comparable to previously reported fluoropolymer-containing membranes (0.012-0.035 S cm^{-1} in the temperature range 30–90 °C). In addition, if these membranes were heat-treated at 120-140 °C for different

times during its preparation, the physicochemical properties of the membranes, including IEC, hydrophilicity, OH^- conductivity, and tensile strength, could be easily controlled by adjusting the heating temperature and time [96].

In addition to inorganic particle-blended PPO membranes, PPO can also be blended with organic materials. The sPPO and PVA were crosslinked by double crosslinking agents, monophenyl triethoxysilane (EPh) and tetraethoxysilane (TEOS), through the sol-gel process [97]. Wu *et al*. [83] prepared the cation exchange hybrid membranes for application in a diffusion dialysis (DD) process. The sPPO membranes often perform poorly in aqueous separation processes (e.g., DD process) and easily erode in organic solvents. Thus, sPPO-based IEMs can be modified by mixing them with other polymers that are potentially more stable in organic solvents with a high membrane forming ability (e.g., PVA). This type of PPO-based membrane formation is reported to enhance IEC by providing thermal and mechanical stability, resistivity to organic solvents, and ion transport characteristics (from the use of silanes as crosslinkers) [97].

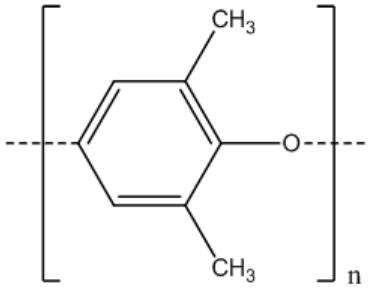

Figure 1.3. Basic chemical structure of poly (2,6-dimethyl-1,4-phenylene oxide).

1.4.4. Nanocomposite membranes for RED

The successful implementation of RED as a feasible sustainable technology for power generation depends on optimizing membrane characteristics and minimizing cost. Currently, commercially available IEMs are not ideal for RED because they lack enhancement in certain membrane properties necessary for this application. Various preparation methods and materials for RED membrane synthesis have been explored. The synthesis of custom-made RED membranes in recent years has improved membrane properties, leading to higher power density yields. A composite structure formed by introducing inorganic nanomaterial into an organic polymer matrix can also be a potential candidate for RED. Nanocomposite IEMs allow extra ion exchangeable functional groups into the structure, which is advantageous in enhancing the electrochemical characteristics of the membrane. Many membrane studies have focused on combining and deriving the unique features of various inorganic nanoparticles with those of organic materials, particularly in electrodialysis, fuel cell, and water treatment applications (Table 1.3). Although the listed examples in Table 1.3 were not prepared for RED application, some of the characteristics reported are beneficial in facilitating the ionic current in an RED stack, which can be helpful for power generation. For example, the studies of Al_2O_3/PVA [98] and ZrO_2/Nafion [99] nanocomposite membranes showed some beneficial features that directly affect the power density, that is, a membrane area resistance of 0.2-0.4 Ωcm^2 (Al_2O_3/PVA) and 0.13-0.15 Ωcm^2 (ZrO_2/Nafion). Moreover, the combination of multi-walled carbon nanotube/PVA [100] and SiO_2/PVDF [101] also exhibited a high degree of IEC with the controlled amount of nanomaterial used. Such studies support that both physico-

and electrochemical properties (e.g., IEC, swelling degree, resistance) of resultant membranes were highly dependent on the nanoparticle amount applied in the polymer matrix.

Table 1.3. Existing nanocomposite membranes of various applications.

Nano material	Organic material	Swelling degree (%)	IEC (meq/g)	Conductivity / Resistance	Applications	Ref.
Al_2O_3	PVA	-	-	0.2-0.4 Ωcm^2	Quaternized composite membrane for alkaline DMFC	98
CeO_2	Nafion	17-22	-	0.018 S/cm	Chemically durable proton exchange membrane for fuel cell	102
$Cu_3(PO_4)_2$ $Ni_3(PO_4)_2$	PVC	-	-	-	Electrochemical evaluation of two composite IEMs	103
Fe_2O_3	Nafion	22.9-40.7	-	-	High proton conductivity composite membrane for DMFC	104
Fe_2NiO_4	PVC	17-23	1.5-1.6	9.1-12.8 Ωcm^2	Performance evaluation of heterogeneous CEM	105
MWCNT	PVA	38.2-284.0	0.7-2.25	-	Crosslinked nanocomposite membrane for DMFC	100
SiO_2	PPO	45.2-325.9	1.3-2.0	0.001–0.0085 S/cm	AEM for alkaline fuel cells: Effect of heat treatment	96
SiO_2	PVA	-	1.0-1.26	-	Electrochemical characterization of AEM	106
SiO_2	PPO	20-27	0.7-1.0	-	Fuel cell application	107
SiO_2	PVA	32-54	0.6-1.2	0.004-0.014 S/cm	Thermally stable CEMs for fuel cell and chlor-alkali application	108
SiO_2	PVA/PPO	100-475	0.5-1.35	-	Double organic phases for diffusion dialysis (alkali recovery)	97
SiO_2	PVDF	10-26.2	1.25-2.0	0.0026-0.0041 S/cm	Electrochemical characterization of CEM	101
SiO_2	Nafion	3-9	-	-	Proton conducting membrane for DMFC	109
SiO_2	Nafion	20-35	-	-	Investigation of composite membrane for PEMFC	110
SiO_2	PES	9.7-14.3	0.74-1.1	0.00007-0.00024 S/cm	Electrodialysis IEM for desalination	34
SiO_2	PPEK	28-70	-	-	Proton exchange membrane for DMFC	32
SiO_2	PAES	26-37.5	-	0.08-0.13 S/cm	Fuel cell application	31
SiO_2	PS	-	0.48-1.3	0.00007-0.0003 S/cm	Performance evaluation: Proton and methanol transport	111
SiH_4	PEO	127-203	0.4-0.99	-	Thermally stable negatively charged NF membrane	112
TiO_2	PES	-	-	-	UV-irradiated TiO_2 for modification of UF membrane	113
TiO_2	PES	-	-	-	Performance evaluation of PES composite membrane	114
TiO_2	Nafion	30-36.5	-	0.0705-0.0947 S/cm	Solid superacid composite membrane for DMFC	115
TiO_2	Nafion	-	-	-	Electrochemical performance for DMFC	116
TiO_2	PVA	20-130	-	-	Pervaporation separation of water-isopropanol mixture	117
TiO_2	PVDF	-	-	-	Anti-fouling performance and water treatment	118
TiO_2	PES/PVA	40-110	-	-	Flux and salt rejection of NF membrane	119
ZrO_2	Nafion	-	-	-	Asymmetric hybrid membrane for gas permeability	120
ZrO_2	Nafion	21-27	0.9-1.13	-	Conductive composite membrane for PEMFC	121
ZrO_2	Nafion	-	-	0.13-0.15 Ωcm^2	Solid polymer electrolyte electrolyzer application	99
ZrO_2	PVDF	-	-	-	Performance evaluation of UF membrane	122
ZrO_2	Nafion	20-30	0.84-0.92	-	Performance at high temperature/low humidity for PEMFC	123
ZrO_2	Nafion	-	-	-	Proton conductivity for high temperature DMFC	124

PPO: Poly (2,6-dimethyl-1,4-phenylene oxide); PVA: Polyvinyl alcohol; PVDF: Polyvinylidene fluoride; PVC: Polyvinyl chloride; PES: Polyethersulfone; PPEK: Poly (phthalazinone ether ketone); PAES: Poly(arylene ether sulfone); PS: Polystyrene; PEO: Polyethylene oxide; MWNT: Multi-walled carbon nanotube; PEM: Polymer electrolyte membrane; PEMFC: Proton exchange membrane fuel cell; DMFC: Direct methanol fuel cell; NF: Nanofiltration; UF: Ultrafiltration.

CHAPTER 2

RESEARCH OBJECTIVES

2.1. Research objectives

The overarching objective of my research is to optimize the RED system for efficient and stable salinity gradient power generation. Reliable process-based models must be first developed in order to make this technology feasible for large-scale application. Furthermore, detailed studies on the performance of IEMs that are most suitable for RED based power generation are necessary. This research aims to accomplish these objectives by: 1) developing a new model that uses the key elements to evaluate the performance of multi-ionic salt solutions (monovalent and divalent ions) in an RED system; 2) preparing and synthesizing of novel organic-inorganic nanocomposite cation exchange membranes; and 3) determining their potential for use in RED systems for salinity gradient power generation through characterization studies on synthesized IEMs. Considering these objectives, we consider the following hypotheses:

i. RED performance is greatly affected by the operational (e.g., flow rate) and physical parameters (e.g., intermembrane distance) of an RED stack. Power output can be improved by applying different conditions to each saline and freshwater compartment under realistic salinity conditions (presence of both mono- and multivalent ions) and it is feasible to model the process by computing the stack voltage, cell resistance, and power density.

ii. Addition of functionalized (i.e., sulfonation) nanoparticles onto the organic polymer will enhance the effective fixed-charge density of the RED ion exchange membrane.

iii. The optimum amount of functionalized nanoparticles within the polymer matrix can improve ionic transport properties (IEC, permselectivity) of the membranes.

iv. Structural alterations (membrane thickness, porosity, nanoparticle size) of nanocomposite membranes can enhance electrochemical properties (e.g., membrane resistance) of the membrane and could be correlated with its RED power generation.

2.2. Organization of this dissertation

Chapter 1 briefly introduced the background of salinity gradient power generation focusing on RED process. The mechanisms of the RED technique and how it has been developed were reviewed. I discussed the need of developing a predictive model considering the coexistence of mono- and multivalent ions in natural water systems. Due to the crucial role that IEMs play in the RED power generation, I specifically reviewed in detail the key properties of potential RED membranes, preparation method for IEMs, and selection of the polymeric material. I further discussed the available nanocomposite membranes for various applications and its potential to be applied in RED application. Chapter 2 outlined the research objective, organization of the dissertation, and important contributions.

Chapter 3 investigated the effect of realistic salinity conditions of the natural water environment on RED power generation. I developed a new process-based model to quantify the power generation with coexisting monovalent and multivalent salt ions.

Considering high resistivity with the presence of multivalent ions that retards high power output, the model prediction suggested the optimized approach of module design and operations.

Chapter 4 presented the preparation of a new type of organic-inorganic nanocomposite cation exchange membranes and its performance characteristics. The combination of functionalized iron (III) oxide (Fe_2O_3-SO_4^{2-}) with the sulfonated poly (2,6-dimethyl-1,4-phenylene oxide) (sPPO) polymer matrix showed great potential of nanocomposite membranes specifically for power generation by RED. Various inorganic filler loadings were tested within the composite membranes to demonstrate the optimal amount for the enhanced performance in RED.

Chapter 5 investigated the effect of structural modification of the nanocomposite membranes on electrochemical performance and salinity gradient power generation. Porous nanocomposite cation exchange membranes were prepared via a two-step phase inversion technique. The structural variation (porosity) of the polymeric membranes was controlled by phase inversion technique and membrane thickness under various inorganic particle filler loadings.

Chapter 6 further investigated the effect of membrane structure with different sizes of inorganic particle filler at various loading concentrations. The preparation of tailor-made nanocomposite CEMs containing sulfonated PPO and sulfonated silica (SiO_2-SO_3H) was presented. The effect of particle size variation on pore formation and membrane structure was examined with a special focus on its polymer/filler interactions and demonstrated its electrochemical characteristics and RED power performance.

Chapter 7 summarized findings in the dissertation and recommended future research direction to advance the development of RED system with regard to effective membrane and stack design. In brief, future work to advance the RED power generation may include the following crucial issues: (a) Identify cost-competitive membrane materials for RED application. (b) Investigation of appropriate RED-specific membrane preparation methods. (c) Development of carefully optimized membrane design for specific conditions (natural salinity environment) and solutions for the RED process. (d) Investigation of the optimized stack configurations and operating conditions to minimize the overall stack resistance for maximizing the power generation.

2.3. Originality and merit of research

The findings of this dissertation are original and aimed at achieving better understandings of salinity gradient power generation and optimizing RED power system for maximum electricity production. The most important message to deliver from this study is to stress the significance of untapped energy resource of our nature that is often wasted. Specifically, the knowledge gained from this dissertation is dedicated to the development of salinity gradient energy research from the following four major aspects:

(1) Development of process-based predictive model for large scale application in natural water system;

(2) Optimization of module scale design and operation;

(3) Development of RED-specific nanocomposite membranes;

(4) Optimization of target membrane properties (tailor-made) for RED.

CHAPTER 3

EFFECT OF NATURAL SALINITY CONDITIONS ON THE REVERSE ELECTRODIALYSIS POWER GENERATION

3.1. Abstract

Sodium chloride alone has been widely used to create power via salinity gradients in lab-scale RED systems. In an effort to simulate realistic salinity conditions in the natural water environment, in this study a new RED model was developed to quantify the power generation with coexisting monovalent and multivalent salt ions. The effects of different flow rate ratios (saline water flow, $Ø_S$, over freshwater flow, $Ø_F$) and intermembrane distance ratios on power density (amount of power per unit membrane area) were investigated. Our results indicated that magnesium sulfate, sodium sulfate, and magnesium chloride in the feed solutions of the RED system led to a 15–43% lower power density than when sodium chloride was the single ion source, largely because of the higher internal stack resistance of the multivalent ions. Higher power densities could be achieved with higher flow rates in the saline water compartment and shorter intermembrane distances in the freshwater compartment. For example, the power density increased by approximately 11% when the flow rate ratio was 5 compared with 1; similarly, an intermembrane distance ratio of 8 yielded an approximately 74% increase in power density compared with a ratio of 1. To the best of our knowledge, this work is the first to develop a quantitative model for the power generation of RED system in the presence of natural salinity compositions, which consist of mono- and multivalent ions.

3.2. Introduction

Although RED has been investigated for more than 60 years [3], some challenges are associated with its application in realistic water resource conditions. RED research has primarily focused on maximizing the power density and power efficiency by varying physical properties (e.g., membranes and spacers), structural or stack design, and operating conditions (e.g., residence time and electrical load). In most of the reported RED studies, sodium chloride was the only salt present in the saline water source used to create the salinity gradient [7, 9, 10, 17-24, 125]. However, various types of salt ions exist in environmental saline water, including magnesium, calcium, sulfate, and bicarbonate. Although a few studies have taken into account the presence of multivalent ions, they have used ferrous iron, manganese, zinc sulfate, or highly concentrated magnesium in ionic conditions that are present only in brines or Dead Sea water. The effects of other common multivalent ions (e.g., magnesium and sulfate) on power generation remain unexplored. Thus, it is important to comprehensively investigate the common multivalent ions in realistic natural concentrations in RED research. Specifically, the chemical potential of different compositions and concentrations of ions in feed solutions may vary the power density significantly. Accordingly, optimization of response parameters (e.g., operational and physical parameters) is critical to maximizing the power generation. These issues, however, have not been well addressed yet owing to our limited understanding of the chemical influences and mechanisms of multivalent and monovalent ions together in a RED system.

In this study, we developed a mathematical model that uses the key elements of electromotive force, internal stack resistance, salt and water flux, and concentration

gradient to evaluate the performance of multi-ionic salt solutions (monovalent and divalent ions) in a RED system. RED performance was quantified by stack voltage, cell resistance, and power density with the key parameters optimized for improving the RED performance. This model is used to examine the effects on the stack open circuit voltage (OCV) and power density generation of magnesium sulfate, sodium sulfate, and magnesium chloride together with sodium chloride in feed solutions. Moreover, the effects of various flow rate ratios and intermembrane distance ratios on the power density were evaluated.

3.3. Model development

In this model, the applied salt ions presumably travel uniformly through their respective membranes as plug flow [19]. Thus, as salt ions from the saline water compartment traverse to freshwater compartments, a concentration gradient is created that leads to a steady decrease in the saline water concentration. As the freshwater moves in the direction opposite that of the saline water, the salt concentration in the freshwater increases. To determine the effect of different ionic compositions of the feed solution on the power density, we developed a model for three different monovalent and multivalent ion compositions. In each combination, $MgSO_4$, Na_2SO_4, and $MgCl_2$ were added to a standard NaCl solution at different concentrations based on typical average seawater and river water compositions. These combinations of monovalent and multivalent ions, which reflect realistic salinity conditions, were introduced in this model to predict electromotive force, salt/water flux, and internal cell resistance and ultimately to estimate the power generation.

First, we developed mathematical expressions for the electromotive force of the mixture of monovalent and multivalent ions to estimate the voltage the system can generate. Then the ion flux of salts and water and the changes in salt concentrations in the saline waters and freshwaters were calculated. Finally, the internal cell resistance of saline water and freshwater compartments was determined, which is a key factor in the voltage and power density generation. Most parameters used in this modeling were extracted from the reported literatures as shown in Table 3.1, but membrane parameters such as permselectivity (α) and area resistance (R) were adopted from provided manufacture specification. In this study, only co-current operation was considered even though counter-current operation is often more efficient. This decision was based on reports [10, 19] indicating that co-current operation leads to higher power density without the higher risk of leakage owing to smaller local pressure differences between the saline water and freshwater compartments.

The model assumes the following:

(a) The RED system has a single cell.

(b) Power density generation is under the maximal power condition of equal internal and external resistance [10, 22].

(c) The system operates in co-current mode.

3.3.1. Electromotive force

Diffusion of cations (Na^+ and Mg^{2+}) through the CEMs and anions (Cl^- and SO_4^{2-}) through the AEMs will create a potential difference owing to the charge accumulation on both sides of the membrane stack, and the Nernst potential equation can be used to

calculate the expected electromotive force of a modular cell unit (E). The total electromotive force of the cell is the sum of the potential differences that are generated over the stack. The contributions of the activities to the electromotive force for mixtures of different salts can be expressed, according to the Nernst equation [13], as follows:

For the model of saline water and freshwater containing NaCl + $MgSO_4$,

$$E_{cell}(x) = \alpha_{CEM}\frac{RT}{Fd}\left[\ln\left(\frac{\gamma_S^{Na^+}(x)C_S^{Na^+}(x)}{\gamma_F^{Na^+}(x)C_F^{Na^+}(x)}\right)\right] + \alpha_{AEM}\frac{RT}{Fd}\left[\ln\left(\frac{\gamma_S^{Cl^-}(x)C_S^{Cl^-}(x)}{\gamma_F^{Cl^-}(x)C_F^{Cl^-}(x)}\right)\right]$$

$$= \alpha_{CEM}\frac{RT}{Fd}\left[\ln\left(\frac{\gamma_S^{Mg^{2+}}(x)C_S^{Mg^{2+}}(x)}{\gamma_F^{Mg^{2+}}(x)C_F^{Mg^{2+}}(x)}\right)^{\frac{1}{2}}\right] + \alpha_{AEM}\frac{RT}{Fd}\left[\ln\left(\frac{\gamma_S^{SO_4^{2-}}(x)C_S^{SO_4^{2-}}(x)}{\gamma_F^{SO_4^{2-}}(x)C_F^{SO_4^{2-}}(x)}\right)^{\frac{1}{2}}\right] \quad (1)$$

For the model of saline water and freshwater containing NaCl + Na_2SO_4,

$$E_{cell}(x) = \alpha_{CEM}\frac{RT}{Fd}\left[\frac{1}{Z_i}\ln\left(\frac{\gamma_S^{Na^+}(x)C_S^{Na^+}(x)}{\gamma_F^{Na^+}(x)C_F^{Na^+}(x)}\right)\right]$$

$$+\alpha_{AEM}\frac{RT}{Fd}\left[\frac{1}{Z_i}\ln\left(\frac{\gamma_S^{Cl^-}(x)C_S^{Cl^-}(x)}{\gamma_F^{Cl^-}(x)C_F^{Cl^-}(x)}\right) + \frac{1}{Z_i}\ln\left(\frac{\gamma_S^{SO_4^{2-}}(x)C_S^{SO_4^{2-}}(x)}{\gamma_F^{SO_4^{2-}}(x)C_F^{SO_4^{2-}}(x)}\right)^{\frac{1}{2}}\right] \quad (2)$$

For the model of saline water and freshwater containing NaCl + $MgCl_2$,

$$E_{cell}(x) = \alpha_{CEM}\frac{RT}{Fd}\left[\frac{1}{Z_i}\ln\left(\frac{\gamma_S^{Na^+}(x)C_S^{Na^+}(x)}{\gamma_F^{Na^+}(x)C_F^{Na^+}(x)}\right) + \frac{1}{Z_i}\ln\left(\frac{\gamma_S^{Mg^{2+}}(x)C_S^{Mg^{2+}}(x)}{\gamma_F^{Mg^{2+}}(x)C_F^{Mg^{2+}}(x)}\right)^{\frac{1}{2}}\right]$$

$$+\alpha_{AEM}\frac{RT}{Fd}\left[\frac{1}{Z_i}\ln\left(\frac{\gamma_S^{Cl^-}(x)C_S^{Cl^-}(x)}{\gamma_F^{Cl^-}(x)C_F^{Cl^-}(x)}\right)\right] \quad (3)$$

where α is the permselectivity of the membrane, R is the gas constant, T is the absolute temperature, Fd is the Faraday constant, and z is the valence. The subscript i refers to individual ions, S and F refer to saline water and freshwater, and γ and C represent the activity coefficient and concentration of each ion, respectively.

The activity coefficients can be estimated by the Debye-Hückel theory and its extensions, expressed as follows [126]:

$$\log\gamma(x)=\frac{-Az^2\sqrt{\mu(x)}}{1+(a\sqrt{\mu(x)}/B)} \quad (4)$$

where a is the effective ion size (pm); μ the ionic strength of the solution (mol/L); and A and B are constants, 0.509 and 328 (at 25°C), respectively. It should be noted that for the case of high salinity condition (i.e., >3.5% salinity), the Pitzer theory is known to be more appropriate to estimate the activity coefficient [127].

3.3.2. Salt and water flux

In the RED system, salt flux migrates from the saline water to the freshwater compartment and water flux from the freshwater to the saline water compartment. Salt transport primarily arises from the amount of electrical charge carried by the current *(I)*, expressed as I/Fd [128]. In addition, co-ion transport through the membranes must be considered a salt flux [21]. Co-ion transport occurs because the ion exchange membranes are permeable to ions with the same charge. The membrane-phase co-ion transport can simply be represented by the diffusion coefficient of ions (D) and the concentration

gradient (ΔC) over the membrane thickness (δ_m). The salt-ion fluxes (J) are thus defined as:

$$J_{Na^+}(x) = \frac{I(x)}{Fd} + \frac{D_{Na^+}}{\delta_m}\left[C_S^{Na^+}(x) - C_F^{Na^+}(x)\right] \quad (5)$$

$$J_{Cl^-}(x) = \frac{I(x)}{Fd} + \frac{D_{Cl^-}}{\delta_m}\left[C_S^{Cl^-}(x) - C_F^{Cl^-}(x)\right] \quad (6)$$

$$J_{Mg^{2+}}(x) = \frac{I(x)}{Fd} + \frac{D_{Mg^{2+}}}{\delta_m}\left[C_S^{Mg^{2+}}(x) - C_F^{Mg^{2+}}(x)\right] \quad (7)$$

$$J_{SO_4^{2-}}(x) = \frac{I(x)}{Fd} + \frac{D_{SO_4^{2-}}}{\delta_m}\left[C_S^{SO_4^{2-}}(x) - C_F^{SO_4^{2-}}(x)\right] \quad (8)$$

where I is the current density (A/m^2), D is the ionic diffusion coefficient (m^2/s), and δ_m is the membrane thickness (m). The term I can be defined by Ohm's law as follows [53]:

$$I(x) = \frac{E_{cell}(x)}{R_{\text{int}}(x) + R_{ext}(x)} \quad (9)$$

where the total resistance is composed of an internal (R_{int}) and an external (R_{ext}) resistance. Theoretically, the maximal power can be achieved when the external resistance is equal to the internal resistance [18].

The water flux (J_{H2O}) moves from the freshwater compartment to the saline water compartment through the membrane owing to osmosis. The water flux is doubled, because water can permeate through two membrane pathways, and the negative sign (–) indicates the flow direction, which is opposite to the salt flux. The water flux for the mixture of NaCl/$MgSO_4$ (eq. 10), NaCl/Na_2SO_4 (eq. 11), and NaCl/$MgCl_2$ (eq. 12) can be expressed by Fick's law as follows:

$$J_{H_2O}(x) = -\frac{2D_{H_2O}}{\delta_m}\begin{bmatrix}\left(C_S^{Na^+}(x)+C_S^{Cl^-}(x)+C_S^{Mg^{2+}}(x)+C_S^{SO_4^{2-}}(x)\right)\\-\left(C_F^{Na^+}(x)+C_F^{Cl^-}(x)+C_F^{Mg^{2+}}(x)+C_F^{SO_4^{2-}}(x)\right)\end{bmatrix} \quad (10)$$

$$J_{H_2O}(x) = -\frac{2D_{H_2O}}{\delta_m}\begin{bmatrix}\left(C_{S1}^{Na^+}(x)+C_S^{Cl^-}(x)+C_{S2}^{Na^+}(x)+C_S^{SO_4^{2-}}(x)\right)\\-\left(C_{F1}^{Na^+}(x)+C_F^{Cl^-}(x)+C_{F2}^{Na^+}(x)+C_F^{SO_4^{2-}}(x)\right)\end{bmatrix} \quad (11)$$

$$J_{H_2O}(x) = -\frac{2D_{H_2O}}{\delta_m}\begin{bmatrix}\left(C_S^{Na^+}(x)+C_{S1}^{Cl^-}(x)+C_S^{Mg^{2+}}(x)+C_{S2}^{Cl^-}(x)\right)\\-\left(C_F^{Na^+}(x)+C_{F1}^{Cl^-}(x)+C_F^{Mg^{2+}}(x)+C_{F2}^{Cl^-}(x)\right)\end{bmatrix} \quad (12)$$

As the salt ions migrate along both water compartments and permeate through the ion exchange membranes, the saline water concentration decreases and the freshwater concentration increases across the membrane. The changes in saline water and freshwater concentrations depend on the salt (J) and water (J_{H2O}) fluxes (toward the membrane surface) as the solution moves along the solution compartment according to the mass balance. The concentration of saline water and freshwater changes during the transport of ions and are determined by the mass balance equations as follows:

For the case of saline and freshwater containing $NaCl+MgSO_4$,

$$\frac{dC_S^{Na^+}(x)}{dx} = -\frac{b}{\phi_S}J_{Na^+}(x) + C_S^{Na^+}(x)\frac{bJ_{H_2O}(x)}{\phi_S}V_{H_2O} \quad (13)$$

$$\frac{dC_S^{Cl^-}(x)}{dx} = -\frac{b}{\phi_S}J_{Cl^-}(x) + C_S^{Cl^-}(x)\frac{bJ_{H_2O}(x)}{\phi_S}V_{H_2O} \quad (14)$$

$$\frac{dC_S^{Mg^{2+}}(x)}{dx} = -\frac{b}{\phi_S}J_{Mg^{2+}}(x) + C_S^{Mg^{2+}}(x)\frac{bJ_{H_2O}(x)}{\phi_S}V_{H_2O} \quad (15)$$

$$\frac{dC_S^{SO_4^{2-}}(x)}{dx} = -\frac{b}{\phi_S}J_{SO_4^{2-}}(x) + C_S^{SO_4^{2-}}(x)\frac{bJ_{H_2O}(x)}{\phi_S}V_{H_2O} \quad (16)$$

$$\frac{dC_F^{Na^+}(x)}{dx} = \frac{b}{\phi_F} J_{Na^+}(x) - C_F^{Na^+}(x) \frac{bJ_{H_2O}(x)}{\phi_F} V_{H_2O} \tag{17}$$

$$\frac{dC_F^{Cl^-}(x)}{dx} = \frac{b}{\phi_F} J_{Cl^-}(x) - C_F^{Cl^-}(x) \frac{bJ_{H_2O}(x)}{\phi_F} V_{H_2O} \tag{18}$$

$$\frac{dC_F^{Mg^{2+}}(x)}{dx} = \frac{b}{\phi_F} J_{Mg^{2+}}(x) - C_F^{Mg^{2+}}(x) \frac{bJ_{H_2O}(x)}{\phi_F} V_{H_2O} \tag{19}$$

$$\frac{dC_F^{SO_4^{2-}}(x)}{dx} = \frac{b}{\phi_F} J_{SO_4^{2-}}(x) - C_F^{SO_4^{2-}}(x) \frac{bJ_{H_2O}(x)}{\phi_F} V_{H_2O} \tag{20}$$

For the case of saline and freshwater containing $NaCl+Na_2SO_4$,

$$\frac{dC_{S2}^{Na^+}(x)}{dx} = -\frac{b}{\phi_S} J_{Na2}(x) + C_{S2}^{Na^+}(x) \frac{bJ_{H_2O}(x)}{\phi_S} V_{H_2O} \tag{21}$$

$$\frac{dC_S^{SO_4^{2-}}(x)}{dx} = -\frac{b}{\phi_S} J_{SO_4^{2-}}(x) + C_S^{SO_4^{2-}}(x) \frac{bJ_{H_2O}(x)}{\phi_S} V_{H_2O} \tag{22}$$

$$\frac{dC_{F2}^{Na^+}(x)}{dx} = \frac{b}{\phi_F} J_{Na2}(x) - C_{F2}^{Na^+}(x) \frac{bJ_{H_2O}(x)}{\phi_F} V_{H_2O} \tag{23}$$

$$\frac{dC_F^{SO_4^{2-}}(x)}{dx} = \frac{b}{\phi_F} J_{SO_4^{2-}}(x) - C_F^{SO_4^{2-}}(x) \frac{bJ_{H_2O}(x)}{\phi_F} V_{H_2O} \tag{24}$$

For the case of saline and freshwater containing $NaCl+MgCl_2$,

$$\frac{dC_S^{Mg^{2+}}(x)}{dx} = -\frac{b}{\phi_S} J_{Mg^{2+}}(x) + C_S^{Mg^{2+}}(x) \frac{bJ_{H_2O}(x)}{\phi_S} V_{H_2O} \tag{25}$$

$$\frac{dC_{S2}^{Cl^-}(x)}{dx} = -\frac{b}{\phi_S} J_{Cl2}(x) + C_{S2}^{Cl^-}(x) \frac{bJ_{H_2O}(x)}{\phi_S} V_{H_2O} \tag{26}$$

$$\frac{dC_F^{Mg^{2+}}(x)}{dx} = \frac{b}{\phi_F} J_{Mg^{2+}}(x) - C_F^{Mg^{2+}}(x) \frac{bJ_{H_2O}(x)}{\phi_F} V_{H_2O} \tag{27}$$

$$\frac{dC_{F2}^{Cl^-}(x)}{dx} = \frac{b}{\phi_F} J_{Cl2}(x) - C_{F2}^{Cl^-}(x) \frac{bJ_{H_2O}(x)}{\phi_F} V_{H_2O} \quad (28)$$

where b is the width of a cell, $Ø_S$ and $Ø_R$ are the flow rates of saline and freshwater and V_{H2O} is the molar volume of water. Note that Na^+ and Cl^- equations (13, 14: saline and 17, 18: fresh) also applies for the cases of NaCl+Na_2SO_4 and NaCl+$MgCl_2$.

3.3.3. Internal cell resistance

The total cell resistance (R_{int}) of an ideal stack consists of four components [18]:

$$R_{\text{int}}(x) = R_S(x) + R_F(x) + R_{AEM} + R_{CEM} \quad (29)$$

where R_S and R_F are the compartment resistances of the saline and freshwater compartments, and R_{AEM} and R_{CEM} are the membrane area resistances for the AEM and CEM, respectively.

The cell resistance of an aqueous solution can be expressed as a function of conductivity (κ) and water compartment thickness (δ). The conductivity (κ) is equal to the product of the molar conductivity of the solution (Λ_m) and C_{ave} [129]. The cell resistance can be expressed as follows [53]:

For the case of saline and freshwater containing NaCl+$MgSO_4$,

$$R_S(x) = f\left(\frac{\delta_S}{\left[\lambda_{m,S}^{NaCl}(C_{S,ave}^{Na^+} + C_{S,ave}^{Cl^-})/2\right] + \left[\lambda_{m,S}^{MgSO_4}(C_{S,ave}^{Mg^{2+}} + C_{S,ave}^{SO_4^{2-}})/2\right]}\right) \quad (30)$$

$$R_F(x) = f\left(\frac{\delta_F}{\left[\lambda_{m,F}^{NaCl}(C_{F,ave}^{Na^+} + C_{F,ave}^{Cl^-})/2\right] + \left[\lambda_{m,F}^{MgSO_4}(C_{F,ave}^{Mg^{2+}} + C_{F,ave}^{SO_4^{2-}})/2\right]}\right) \quad (31)$$

For the case of saline and freshwater containing NaCl+Na_2SO_4,

$$R_S(x) = f\left(\frac{\delta_S}{\left[\lambda_{m,S}^{NaCl}(C_{S1,ave}^{Na^+} + C_{S,ave}^{Cl^-})/2\right] + \left[\lambda_{m,S}^{Na_2SO_4}(C_{S2,ave}^{Na^+} + C_{S,ave}^{SO_4^{2-}})/2\right]}\right) \quad (32)$$

$$R_F(x) = f\left(\frac{\delta_F}{\left[\lambda_{m,F}^{NaCl}(C_{F1,ave}^{Na^+} + C_{F,ave}^{Cl^-})/2\right] + \left[\lambda_{m,F}^{Na_2SO_4}(C_{F2,ave}^{Na^+} + C_{F,ave}^{SO_4^{2-}})/2\right]}\right) \quad (33)$$

For the case of saline and freshwater containing NaCl+$MgCl_2$,

$$R_S(x) = f\left(\frac{\delta_S}{\left[\lambda_{m,S}^{NaCl}(C_{S,ave}^{Na^+} + C_{S1,ave}^{Cl^-})/2\right] + \left[\lambda_{m,S}^{MgCl_2}(C_{S,ave}^{Mg^{2+}} + C_{S2,ave}^{Cl^-})/2\right]}\right) \quad (34)$$

$$R_F(x) = f\left(\frac{\delta_F}{\left[\lambda_{m,F}^{NaCl}(C_{F,ave}^{Na^+} + C_{F1,ave}^{Cl^-})/2\right] + \left[\lambda_{m,F}^{MgCl_2}(C_{F,ave}^{Mg^{2+}} + C_{F2,ave}^{Cl^-})/2\right]}\right) \quad (35)$$

where $C_{S,ave}$ and $C_{F,ave}$ represent the average ion concentrations of saline and freshwater, respectively and f is the obstruction factor. The obstruction factor, f was introduced to describe the negative shielding effects of the spacer that cause the electrical resistance to increase [19]. The spacers used in the experiment occupy 46% of the area in a plane projection, leading an obstruction factor of 1/(1 – 0.46) = 1.9 [20].

Finally, the power density can be calculated as follows:

$$P_d(x) = \frac{1}{2} I^2(x) R_{ext}(x) \quad (36)$$

The power density is halved because of the two ion exchange membranes in a cell. The maximum P_d is then expressed as:

$$P_d(x) = \frac{1}{2}\left(\frac{E(x)}{2R_{ext}(x)}\right)^2 R_{ext}(x) \quad (37)$$

Table 3.1. Model input parameters used in the RED power generation model.

Input parameter	Symbol	Value	Unit
Permselectivity of CEM	α_{cem}	0.99	dimensionless
Permselectivity of AEM	α_{aem}	0.96	dimensionless
Gas constant	R	8.3143	$Jmol^{-1}K^{-1}$
Temperature	T	298	K
Faraday number	Fd	96,485	C mol^{-1}
Effective Na^+ size	a_{Na+}	358 [130]	pm
Effective Cl^- size	a_{Cl^-}	332 [130]	pm
Effective Mg^{2+} size	a_{Mg2+}	428 [130]	pm
Effective SO_4^{2-} size	$a_{SO4^{2-}}$	379 [130]	pm
Saline and fresh water compartment thickness	δ_S, δ_F	500	µm
Molar conductivity of NaCl in saline water	$\Lambda_{m,S}^{NaCl}$	0.0107 [131]	$m^2\ ohm^{-1}\ mol^{-1}$
Molar conductivity of $MgSO_4$ in saline water	$\Lambda_{m,S}^{MgSO4}$	0.0093 [131]	$m^2\ ohm^{-1}\ mol^{-1}$
Molar conductivity of Na_2SO_4 in saline water	$\Lambda_{m,S}^{Na2SO4}$	0.009 [131]	$m^2\ ohm^{-1}\ mol^{-1}$
Molar conductivity of $MgCl_2$ in saline water	$\Lambda_{m,S}^{MgCl2}$	0.0097 [131]	$m^2\ ohm^{-1}\ mol^{-1}$
Molar conductivity of NaCl in fresh water	$\Lambda_{m,F}^{NaCl}$	0.0124 [131]	$m^2\ ohm^{-1}\ mol^{-1}$
Molar conductivity of $MgSO_4$ in fresh water	$\Lambda_{m,F}^{MgSO4}$	0.0125 [131]	$m^2\ ohm^{-1}\ mol^{-1}$
Molar conductivity of Na_2SO_4 in fresh water	$\Lambda_{m,F}^{Na2SO4}$	0.0126 [131]	$m^2\ ohm^{-1}\ mol^{-1}$
Molar conductivity of $MgCl_2$ in fresh water	$\Lambda_{m,F}^{MgCl2}$	0.0126 [131]	$m^2\ ohm^{-1}\ mol^{-1}$
CEM area resistance	R_{cem}	5.0×10^{-4}	ohm m^2
AEM area resistance	R_{aem}	2.5×10^{-4}	ohm m^2
Diffusion coefficient of Na^+	D_{Na^+}	1.33×10^{-9} [132]	$m^2\ s^{-1}$
Diffusion coefficient of Cl^-	D_{Cl^-}	2.03×10^{-9} [132]	$m^2\ s^{-1}$
Diffusion coefficient of Mg^{2+}	$D_{Mg^{2+}}$	7.06×10^{-10} [132]	$m^2\ s^{-1}$
Diffusion coefficient of SO_4^{2-}	$D_{SO4^{2-}}$	1.06×10^{-9} [132]	$m^2\ s^{-1}$
Diffusion coefficient of water	D_{H2O}	1.0×10^{-9} [132]	$m^2\ s^{-1}$
Width of a cell	b	0.04	m
Length of a cell	L	0.09	m
Membrane thickness	δ_m	30	µm
Molar volume of water	V_{H2O}	1.8×10^{-5}	$m^3\ mol^{-1}$

3.4. Experimental

3.4.1. Stack configuration

The RED stack used in this study consists of 10 cell pairs, each containing an FKB cation exchange membrane and an FAB anion exchange membrane (Fumatech, Germany). Each membrane has an effective area of 4 cm × 9 cm. A CEM was placed at each end of the stack as a shielding membrane. Titanium mesh end electrodes coated with iridium plasma were used as the anode and cathode. Woven fabric spacers (wire diameter 250 µm, porosity 60%) with a thickness of 250 µm were inserted between each membrane to create water compartments for saline water and freshwater solutions to pass through.

3.4.2. Synthetic saline water and freshwater

In this experiment, the synthetic saline water had a concentration of 0.5 M for each Na^+ and Cl^- ions and 0.05 M for each Mg^{2+} and SO_4^{2-} ions. The synthetic freshwater had a concentration of 0.012 M for each Na^+ and Cl^- ions and 0.0002 M for each Mg^{2+} and SO_4^{2-} ions. These concentrations were selected on the basis of the natural composition of typical seawater and river water. During each experiment, one of three combinations of salts was tested: (1) NaCl with $MgSO_4$, (2) NaCl with Na_2SO_4, or (3) NaCl with $MgCl_2$. For the electrode rinse solution, we used a pure NaCl solution with a concentration of 0.003 M, which is the mean salt concentration of the saline water and freshwater used here. The feed solutions for both waters were pumped through the RED stack at various flow rates to investigate the effect on stack OCV.

3.5. Results and discussion

The simple forward Euler algorithm was used in Matlab 2010a to numerically simulate the RED model described above, including the effects of (1) multivalent ions ($MgSO_4$, $MgCl_2$, and Na_2SO_4) on stack OCV, (2) multivalent ions on power density generation, (3) various saline water to freshwater flow rate ratios on RED power output, and (4) various saline water to freshwater compartment intermembrane distance ratios with three different salt combinations.

3.5.1. Stack open circuit voltage (OCV)

At zero current, the stack OCV can be obtained from the inflow concentration of feed solutions. The stack OCV is a measure of the maximum voltage that can be achieved by the RED system. The theoretical OCV value is the sum of the potential difference across each membrane and can be predicted from equations (1–3). Measured and calculated OCV are plotted as a function of the feed solution flow rates in Figure 3.1. The experimentally measured RED stack OCV is normally 92–98% of the theoretical values derived from the Nernst equation at high flow rates [24, 133].

The solution flow rate had a noticeable effect on stack OCV. For instance, at low flow rates, the OCV can decrease significantly, probably due to the concentration polarization that occurs at the membrane-solution interface, and can cause higher internal resistance and a lower concentration gradient for salt and water flux [8]. The resulting phenomenon will eventually lead to a lower OCV. However, the concentration polarization and the internal cell resistance become weaker at higher flow rates, which results in a higher OCV [134]. The concentration gradient equations also describe this result,

as with lower concentration gradients a flow rate decrease will result in considerably smaller OCVs in equations (1–3) and vice versa for higher flow rates. Note that the measurement in low flow rate region (0-1.0 cm/sec) was not implemented due to mechanical control limit of in-flow.

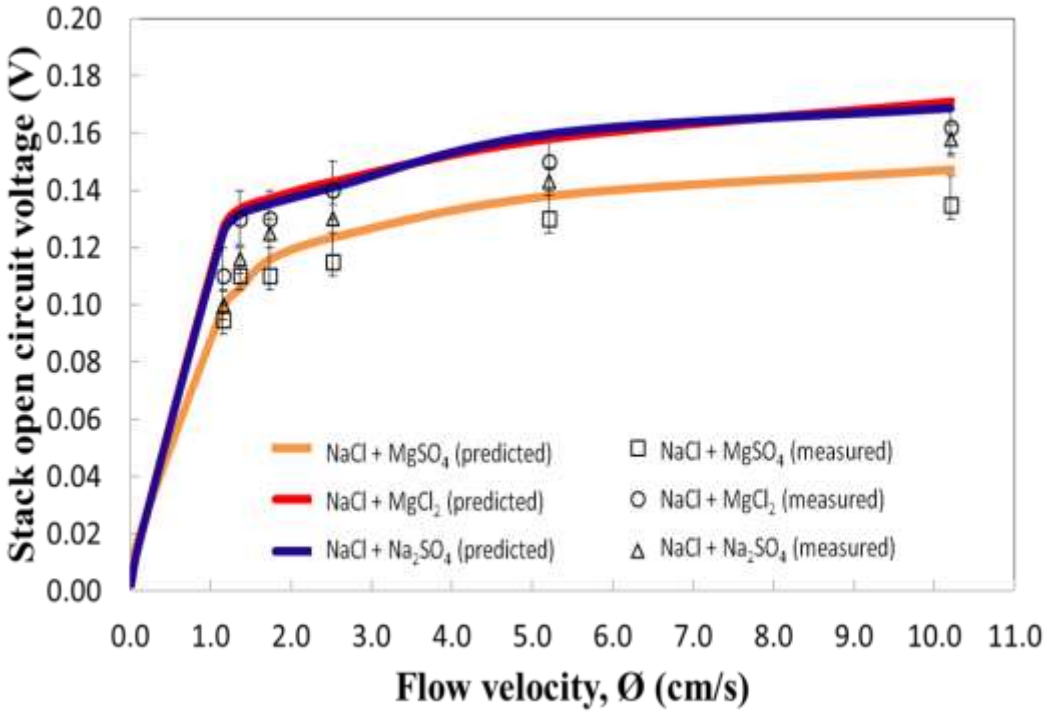

Figure 3.1. OCV at different solution flow rates for three different combinations of salts. The measured data are indicated by open symbols and the calculated values by solid lines.

3.5.2. Power density with different ionic compositions

Figure 3.2a shows the calculated power density using (a) NaCl and $MgSO_4$, (b) NaCl and $MgCl_2$, and (c) NaCl and Na_2SO_4. Clearly, pure NaCl generated a greater power density than any of the multivalent ion combinations. Post *et al.* [27] showed experimental data and some modeling results using different grades of membranes to support multivalent ions lowering power density. Even though the presented model did not consider the implications of the specific membrane selectivity on multivalent ion passage, the result resembles previous studies, indicating that the presence of multivalent ions will likely decrease the magnitude of the power density [27]. The results indicated a 43% decrease with $MgSO_4$, 15% with $MgCl_2$, and 20% with Na_2SO_4 compared with the maximum power density with NaCl.

The location where the maximum power density levels were achieved shifted slightly to the outlet of the ion flow. This is closely related to the changes in internal stack resistance along the ion flow path, as shown in Figure 3.2b. A sharp decrease of the resistance over up to approximately 5 mm of ion flow path caused the power to increase initially but then turn downward as the amount of resistance slowly levels out. The resistance of the pure NaCl solution was remarkably lower than those of the multi-ionic solutions. However, the internal stack resistances of all multi-ionic solutions were comparable, although a mixture of $MgSO_4$ exhibited a slightly higher resistance along the membrane. In fact, the electrical resistance of the freshwater compartment is considered the main cause of the internal stack resistance [10]. The difference of internal stack resistance observed between the monovalent and multivalent ions is caused by the different ionic transport against the activity gradient that limits the electrical current and

power when multivalent ions are present, with higher resistance observed mainly in the freshwater compartment [27]. Therefore, considering the power density generation results in Figure 3.2a, these expected resistance curves are reasonably fitted.

In addition, the power density generated in RED system is influenced by operating residence time. As shown in Figure 3.3, the power density is higher at shorter residence time (i.e. higher flow rates). Though, larger hydrodynamic power losses occur at higher flow rates, the internal stack resistance generated by the concentration polarization will be less significant and thus the power density can be increased. However, as the residence time becomes longer (i.e. lower flow rates), the resistance increases due to the occurrence of severe concentration polarization, which will lead the power density reduced. Therefore, the effect of residence time on power density generation is mostly likely due to its internal stack resistance.

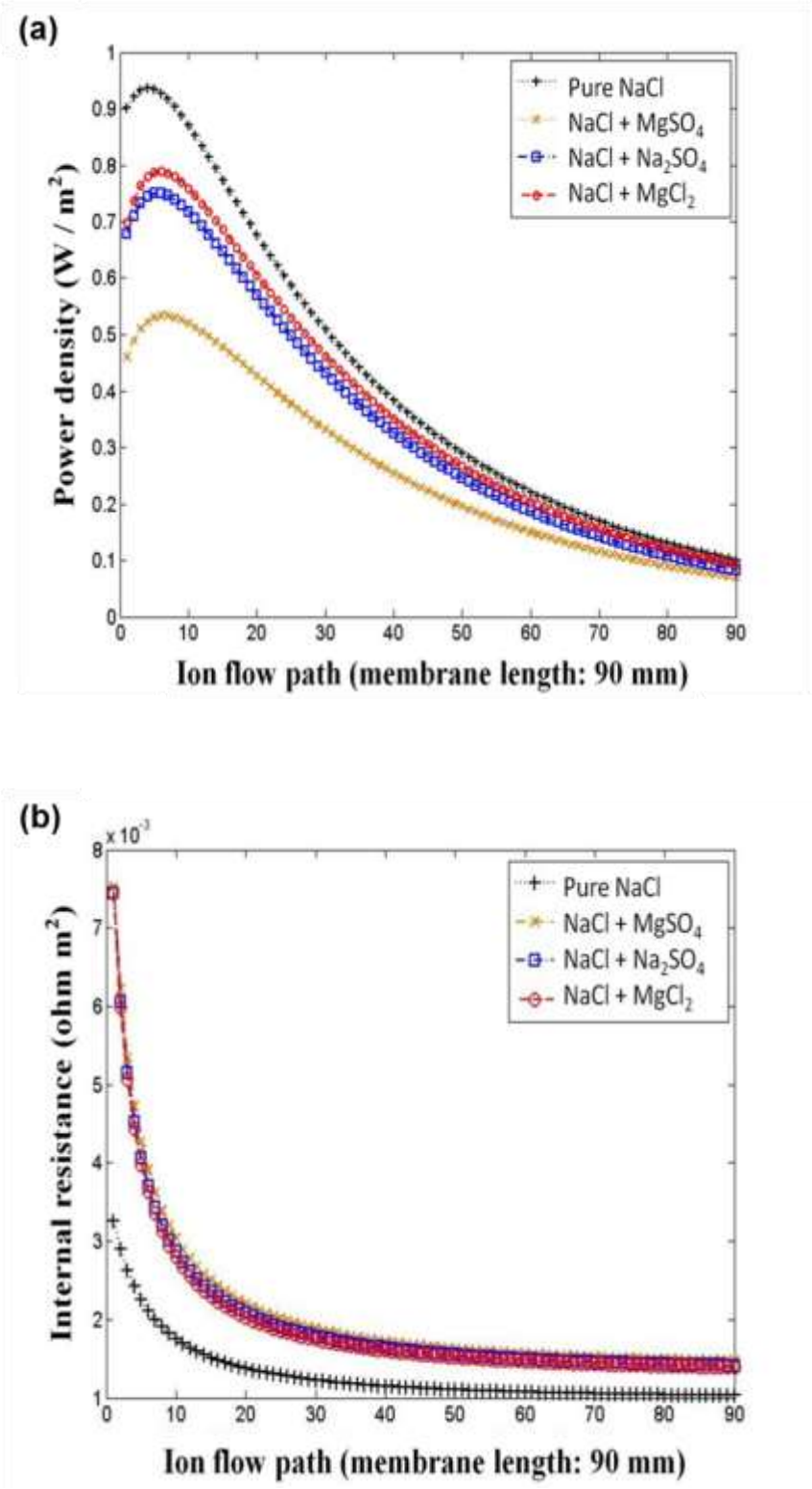

Figure 1.2. Effect of multivalent ions on power density generation (a) and internal stack resistance (b) compared with those of a monovalent ion (pure NaCl) according to modeling predictions.

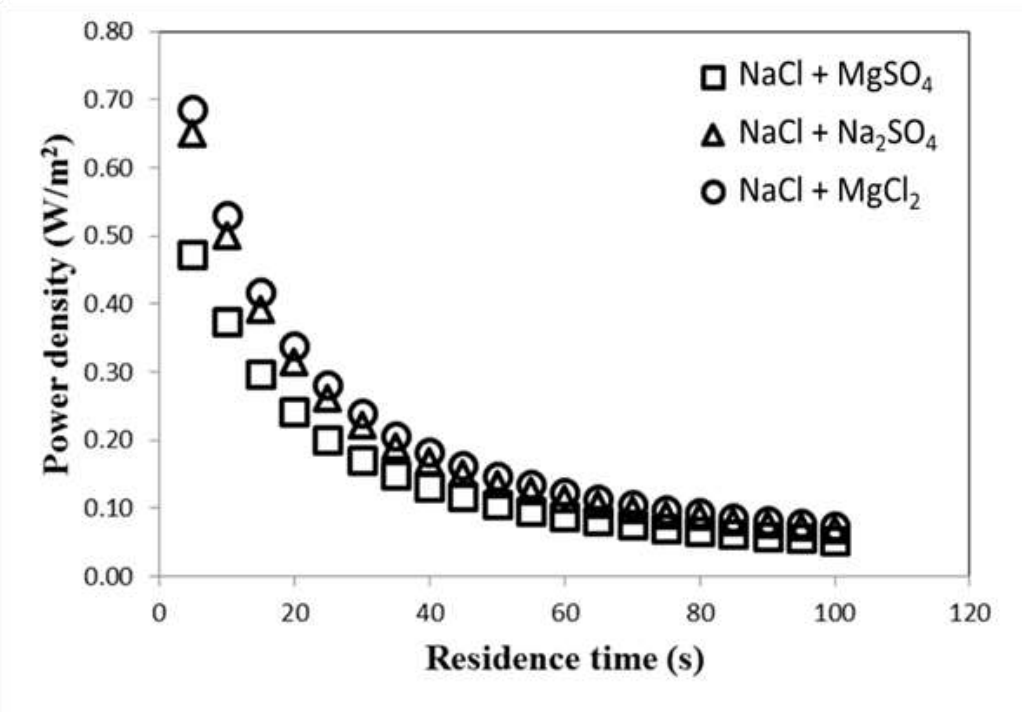

Figure 3.3. Effect of multivalent ions on power density generation (average) as a function of the residence time.

3.5.3. Effects of different flow rate ratios

To study the theoretical limits of RED performance and to quantify the contribution of the flow rates, we tested various saline water to freshwater flow rate ratios using the model. Figure 3.4 shows the maximum and average power densities at various saline water to freshwater flow rate ratios ($Ø_S/Ø_F$). The maximum power density was the point where the internal resistance is equal to the external resistance along the ionic path over the membrane length, whereas the average power was defined as the total developed power over by the membrane area. All of the multivalent ions generated similar patterns of curves at slightly different levels.

Both the maximum and the average power density decreased with higher freshwater flow rates ($Ø_S < Ø_F$) and slightly increased with higher saline water flow rates ($Ø_S > Ø_F$), though the average power density decreased more drastically at lower flow rate ratios. In this case the higher flow rate of saline water reduces the concentration polarization and electrical resistance, which allows higher power output. At high saline water flow rates, higher power generation is reasonable because the concentration gradient at the membrane-solution interface is almost unaffected by the rapid transport of salts through the membrane, which permits the system to maintain a high electromotive force (V) across the membrane according to the model equations (1–3). Moreover, the electrical cell resistance is generally determined by the freshwater compartment when both compartments use the same spacers [19, 25]. Thus, optimal performance can be achieved with higher flow rates in the saline water compartment. However, the maximum allowable increase in saline water flow rate should be further investigated considering its negative impact on the total energy recovery even though greater power density is

achieved. Furthermore, at high flow rates, hydrodynamic resistance leads to higher pressure losses. Consequently, the power density increased slowly as flow rate ratio increased owing to the larger hydraulic loss at the higher saline flow rate. However, at a lower flow rate ratio ($Ø_S/Ø_F < 1$), the power density drops as the total electrical resistance of the saline water compartment becomes greater than that of the freshwater compartment.

3.5.4. Effect of different intermembrane distance ratios

Several studies have investigated the effect of different intermembrane distances (spacer thicknesses) on power density generation [9, 18, 24]. However, such experiments were aimed at adjusting both intermembrane distances to be the same optimal thickness. Studies examining the influence of different intermembrane distance ratios for each saline water and freshwater compartment in a RED system are still rare. Considering the thickness of spacers in our experiment (i.e., 250 μm), intermembrane distance ratio (δ_S/δ_F) was varied with fixing either one of the compartment at 250 μm as maximum distance. Thus, it was either by adjusting the distance of fresh water compartment with fixed saline water compartment thickness for increases in ratio or vice versa for decreases in ratio. Figure 3.5 shows the simulated maximum and average power densities of multivalent ion solutions at different intermembrane distance ratios. All three multi-ionic solutions showed similar trends with minor power density differences. Both maximum and average power densities were observed to increase with a longer saline water than freshwater compartment intermembrane distance ($\delta_S > \delta_F$). The longer intermembrane distance in the saline water compartment seemed to affect the maximum power density

predictions more than the averages. Better performance is expected with a longer saline water intermembrane distance because the hydrodynamic resistance of the saline water compartment becomes much lower than that of the freshwater compartment. A higher ratio ($\delta_S/\delta_F > 1$) also leads to lower electrical resistance in the freshwater compartment, which plays a dominant role with respect to power density generation, leading to greater power density, as shown in Figure 3.5. Increases in both maximum and average power density with longer intermembrane distances of the freshwater compartment ($\delta_S < \delta_F$) were also observed. The power density increase resulting from lower ratios can be attributed to hydrodynamic resistance, which should be reduced with a longer freshwater intermembrane distance. However, electrical resistance also occurs in the freshwater compartment according to model equations (31, 33, and 35) that results insignificant power increase at lower ratios.

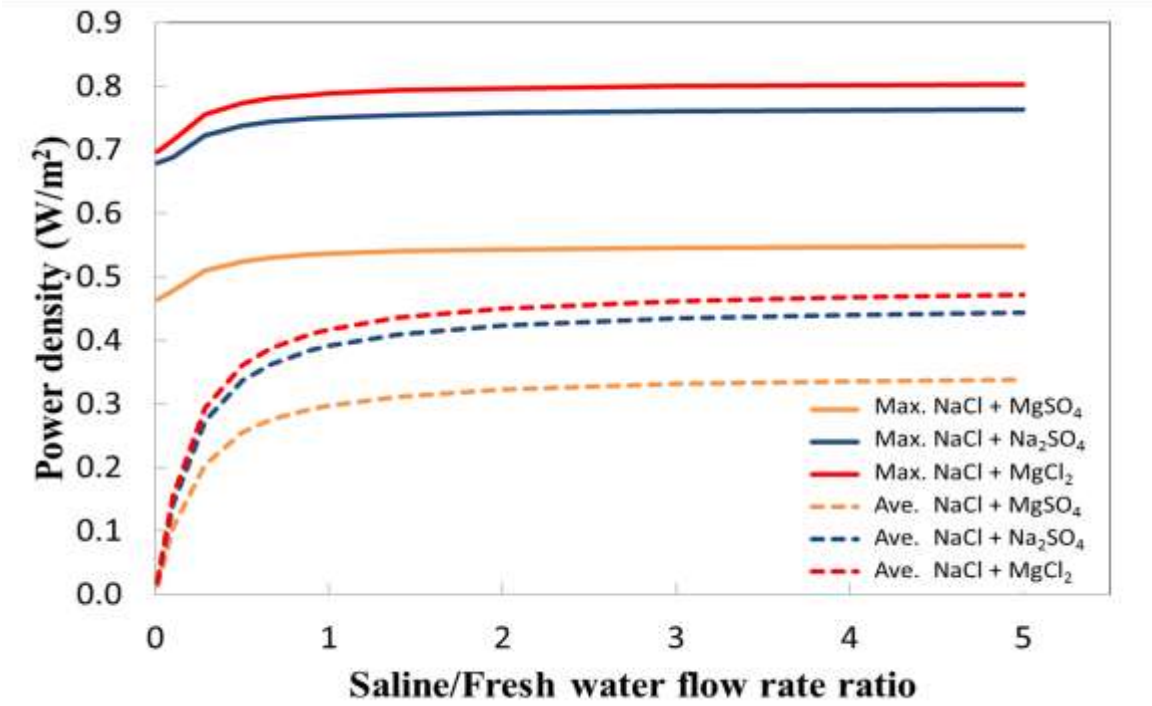

Figure 3.4. Effect of saline water and freshwater flow rate ratios ($Ø_S$ and $Ø_F$) on maximum and average power density modeling predictions using multivalent ions.

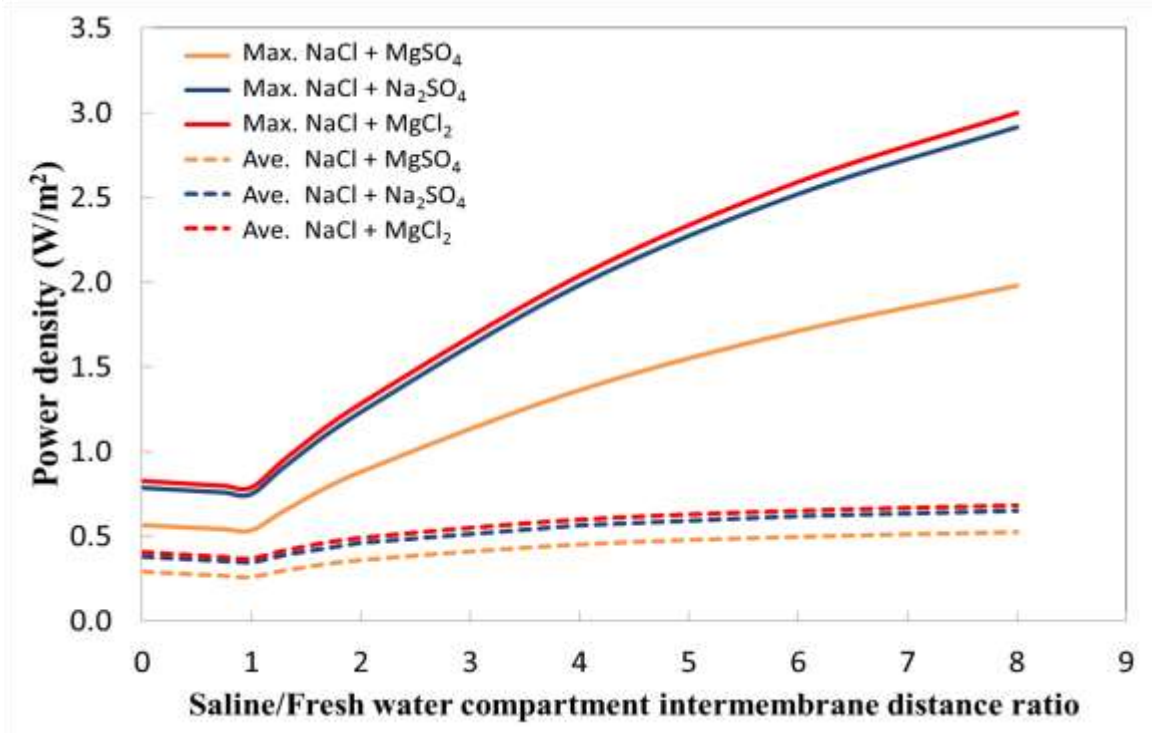

Figure 3.5. Effect of intermembrane distance ratios in saline water and freshwater compartments (δ_S/δ_F) on maximum and average power density modeling predictions using multivalent ions.

3.6. Conclusions

This work is the first attempt to develop a mathematical model of a RED system using multivalent ions for power density generation. The new model illustrates a process-based approach to RED operation with the purpose of simulating more practical feed solutions by incorporating three common multivalent ions ($MgSO_4$, Na_2SO_4 and $MgCl_2$). In this work, the model shows that the power density of a RED system responds to the multi-ionic composition of the aqueous solutions. The model simulation quantified the power output in terms of stack OCV and power density as well as the system's internal cell resistance. The importance of specific parameters such as flow rate ratio and intermembrane distance ratio in the optimal performance of the RED system were illustrated.

The model predictions for stack OCV agreed well with those obtained experimentally. As expected, the stack OCV of the RED system was sensitive to flow rate variation in the presence of multivalent ions. Furthermore, the power density obtained with multivalent ions was fairly lower (15–43%) than that when using a monovalent ion (i.e., NaCl) due to higher internal cell resistance. Higher power density was gained by applying higher flow rates in the saline water compartment than in the freshwater compartment. Moreover, RED performance was significantly improved by using a saline water compartment thicker than the freshwater compartment. The applied conditions provide a better understanding of the RED process, especially the internal cell resistance. Further modeling to optimize the power density generation should be accompanied by a net energy efficiency investigation, especially for realistic environmental salinity conditions. Also, for the large-scale application of real seawater

and river water in RED, the effect of fouling on the membrane, hydrostatic and viscous pressure on feed water transport need to be further investigated and incorporated into the model developed here.

CHAPTER 4

SYNTHESIS OF NOVEL NANOCOMPOSITE REVERSE ELECTRODIALYSIS ION EXCHANGE MEMBRANES

4.1. Abstract

Despite the important role of ion exchange membranes (IEMs) in RED systems, the current absence of proper ion-exchange membranes delays the sustainable development of the RED process for salinity gradient power generation. This chapter presents the preparation of a new type of organic-inorganic nanocomposite cation exchange membranes and its performance characteristics. The combination of functionalized iron (III) oxide (Fe_2O_3-SO_4^{2-}) as an inorganic filler with the sulfonated poly (2,6-dimethyl-1,4-phenylene oxide) (sPPO) polymer matrix proved to have great potential for power generation by RED. The results showed that an optimal amount of Fe_2O_3-SO_4^{2-} (0.5–0.7 wt%) enhanced the key electrochemical properties of the ion-exchange membranes including a permselectivity up to 87.65 % and an area resistance of 0.87 Ω cm^2. The nanocomposite membrane containing 0.7 wt% Fe_2O_3-SO_4^{2-} achieved a maximum power density (amount of power per unit membrane area) of 1.3 W m^{-2}, which is relatively higher than that of the commercially available CSO (Selemion^{TM}, Japan) membranes. The goal of this work is to maximize the salinity gradient power generation by developing RED-specific nanocomposite IEMs. The results show the potential of new design of the nanocomposite IEMs for viable energy generation by RED.

4.2. Introduction

The important membrane properties for power generation particularly that by electrochemical processes such as RED, are IEC, swelling degree (SD), membrane resistance, and permselectivity. Composite membranes created by introducing inorganic materials into an organic polymer matrix are viable candidates for RED, as it allows carrying extra ion-exchangeable functional groups by modulating the membrane structure. Also, organic-inorganic composites combine the unique features of inorganic materials with those of organic materials and have received increasing attention for more than a decade owing to their remarkable synergized properties.[101] Here we focus on the development of organic-inorganic nanocomposite IEMs based on sulfonated poly (2,6-dimethyl-1,4-phenylene oxide) (sPPO) and sulfonated iron oxide (Fe_2O_3-SO_4^{2-}) created via the blending method. PPO is a commonly used polymer in membranes for gas separation, RO, ultrafiltration, and ion exchange [84, 94, 135, 136] because of its excellent membrane-forming properties; good chemical, thermal, and hydrolytic stability; high glass transition temperature (t_g = 210°C); and low cost.[136-138] However, the hydrophobicity of PPO often hinders its dissolution in conventional dipolar solvents. To make the polymer more ion-exchangeable, a conventional electrophilic substitution is often applied to introduce charged groups (i.e., anionic or cationic moieties), typically from a sulfonic acid. Introduction of sulfonate groups ($-SO_3^-$) to the polymer chain of PPO via a sulfonating agent such as chlorosulfonic acid causes PPO to become highly hydrophilic.[139]

Recently, several studies have incorporated sulfonated mesoporous iron (III) oxide (Fe_2O_3-SO_4^{2-}) into proton conductive membranes (PCMs) for fuel cell applications.[104, 140,

[141] The studies revealed that sulfonated Fe_2O_3 facilitates not only conductivity but also strong hydrophilicity and large specific surface area. Sulfonated Fe_2O_3 is expected to be a good filler material because of its high versatilities such as: 1) high specific surface area (decreases crystallites size when functionalized), 2) widely used and cost-effective (easy to produce), 3) high ability to adsorb various inorganic and organic materials, 4) easy to be coated on various surfaces, and 5) high hydrophilicity [104, 142-146]. Moreover, embedding such functionalized inorganic filler in the structure can be considered as a homogeneous ion-exchange resin up to certain level of loading.[35] It is important to have a homogeneous ion exchange resin, because the fixed charge groups are more evenly distributed over the entire membrane matrix in homogeneous membranes, while heterogeneous membranes have distinct region of uncharged polymer of ion exchange resin in the membrane matrix. Therefore, charge density in heterogeneous IEMs is relatively low compared to homogeneous membranes and resistance is higher owing to its membrane structure where uncharged domain exists in the polymer matrix [25]. Therefore, the sulfonated Fe_2O_3 particles are primarily introduced to increase ion-exchangeable functional groups in the membrane, which results in enhanced ion-exchange capacity, hydrophilicity and ion conductivity. Note that the introduction of negatively charged groups (thus, increase in charge density) increase proton conductivity as well as sodium conductivity, but increase in sodium conductivity may not necessarily be the same as that of proton conductivity. However, until now, no research exploring the use of Fe_2O_3-SO_4^{2-} in the PPO polymer matrix has been reported in any fields. In this chapter, we introduce our design strategy for the development of a new type of composite RED membranes: incorporation of

Fe_2O_3-SO_4^{2-} and sPPO polymer. The effect of Fe_2O_3-SO_4^{2-} loading is also investigated to optimize the membrane performance in RED.

4.3. Materials and methods

4.3.1. Materials

Poly (2,6-dimethyl-1,4-phenylene oxide) (PPO) (Aldrich, analytical standard), was used as received. Chloroform (Aldrich, anhydrous, 99%) was used as a solvent. Chlorosulfonic acid (Aldrich, 99%) and sulfuric acid (Aldrich, 98%) were used without purification. Dimethylsulfoxide (DMSO) (ACS grade, 99.9%) was obtained from VWR. Iron (III) oxides (Aldrich, <50nm) was used as received for sulfonation.

4.3.2. Sulfonation of PPO (sPPO)

PPO was sulfonated with chlorosulfonic acid as the sulfonating agent and chloroform as the solvent. PPO of 6 wt% was dissolved in chloroform by mechanical mixing at room temperature for 30 min. 8 wt% solution of chlorosulfonic acid in 50 ml of chloroform was slowly added to the PPO solution over the period of 30 min while stirring the solution vigorously at 25-30 °C until the sulfonated PPO is precipitated. The sulfonated precipitate was washed multiple times with DI water until pH became approximately 5-6. The polymer was then filtered and dissolved in methanol. The solution was poured into a Pyrex glass tray forming a thin film of about 1-2 mm thickness, and allowed to dry in air for 24 h at room temperature. The dried polymer sheet was shredded into small particles and washed with DI water. The sPPO was then filtered and dried in room temperature.

4.3.3. Sulfonation of Fe_2O_3 (Fe_2O_3-SO_4^{2-})

The powder of Fe_2O_3 nanoparticles was sulfonated by concentrated H_2SO_4 (98%). The required amount of Fe_2O_3 was dissolved in 0.25 M concentrated H_2SO_4 at room temperature for 24 h. The concentrated H_2SO_4 treated Fe_2O_3 was then filtered and dried at 80 °C in a vacuum oven. Finally, the powder was calcined at 500 °C for 3 h to obtain the red sulfonated Fe_2O_3 powder.

4.3.4. Membrane preparation

IEMs were prepared by the solvent evaporation technique. Sulfonated PPO polymer was dissolved in Dimethylsulfoxide (DMSO) to obtain 19 wt% solutions. Then 0-2 wt% of sulfonated Fe_2O_3 was mixed with the polymer solution at 40 °C for 24 h while stirring. The solution was vibrated in an ultrasonic bath for 10 min to obtain an optimal dispersion of the particle in the solution. The resulting mixture was cast on a glass substrates using doctor blade method to obtain the desired thickness of the membrane (100 μm). The obtained solid composite membrane was then dried in a vacuum oven at 60 °C for 24 h and at 80 °C for another 24 h to remove residual solvents. The prepared membrane was treated in warm water (40-50 °C) and then in 1 M HCl for 24 h. Finally, the membranes were rinsed with DI water and stored in 0.5 M NaCl solution.

4.3.5. Membrane characterization

FTIR spectroscopy. The chemical structures of composite membranes were investigated using Fourier Transform Infrared (FTIR) Spectra. FTIR spectra of sPPO membranes were acquired with FTIR Spectrometer (Digilab FTS7000) equipped with a microscope (Digilab UMA600), collecting 32 scans per sample at a 4 cm^{-1} resolution and a spectral range of 4000-700 cm^{-1}. The spectrum of ambient air was used as background.

Membrane morphology. Scanning electron microscopy (SEM, Zeiss Ultra60 FE-SEM) was used to observe the morphology and structure of the prepared membranes. For the cross-sectional surface, the samples were prepared in liquid nitrogen and cut manually to obtain sharp cross-section. Membrane samples were then dried overnight to preserve their structure.

Swelling degree. The swelling not only determines mechanical properties and dimensional stability of the membrane, it also influences its ability of ion selectivity and electrical resistance. The SD simply refers to the amount of water content in the membrane per unit weight of dry membrane. To determine the SD of a membrane, a sample was equilibrated in DI water for at least 24 h. The membrane was then taken out and surface water was removed from the sample with blotting paper. The wet weight of the swollen membrane was measured. The membrane was then dried at 50 °C in a vacuum oven until a constant dry weight was obtained. The SD of a membrane was calculated in weight percent by:

$$SD = \frac{W_{wet} - W_{dry}}{W_{dry}} \times 100\% \quad (1)$$

where W_{wet} (g) and W_{dry} (g) are the weight of the wet and the dry membrane, respectively.

Ion exchange capacity. The ion-exchange capacity, which is the number of fixed charges per unit weight of the membrane, was measured using a titration method [53]. Firstly, the cation exchange membrane was equilibrated in 1 M HCl for at least 15 h, and then rinsed free from chloride with DI water. After that, the membrane was immersed into 1 M NaCl solution for another 6 h. The displaced hydrogen ions from the membrane were then

titrated with 0.01 M NaOH solution using phenolphthalein as an indicator. The IEC of membranes were then calculated by using equation (2):

$$IEC = \frac{C_{NaOH} \times V_{NaOH}}{W_{dry}} \quad (2)$$

where C_{NaOH} is the concentration of NaOH solution (mol L^{-1}), V_{NaOH} is the volume of NaOH solution (L) used and W_{dry} is the dry weight (g) of the membrane.

Fixed-charge density. Fixed-charged groups are attached to the polymer backbone in ion-exchange membranes. The counter ion transport and ion permselectivity through the membrane are determined by the fixed charge density in the membrane. The fixed charge density, expressed in milliequivalent of fixed groups per volume of water in the membrane (meq. L^{-1}) can be determined by the IEC over the SD of the membrane.

$$C_{fix} = \frac{IEC}{SD} \quad (3)$$

Electrical resistance. The electrical resistance of the membrane was measured in a two-compartment cell using 0.5 M NaCl aqueous solutions. Titanium electrodes, coated with Ru-Ir mixed metal oxides were used (Jing Run Beijing Science and Technology Research Institute Company, China). The resistance of membranes was measured at room temperature by impedance spectroscopy (IS) using Autolab PGSTAT302N, Metrohm in a frequency range from 10-10^5 Hz with an oscillating voltage of 0.1 V amplitude. [45] The resistance was measured based on the intercept of x-axis (Z', the real part of the transfer function) in the Nyquist plot. Then the membrane resistance (R_{mem}) was determined by subtraction of the resistance measured in the blank test (R_{sol}) from the resistance

measured with the membrane under investigation (R_{cell}), based on the total cell resistance composition (i.e., $R_{cell}=R_{sol}+R_{mem}$).

Permselectivity. The apparent permselectivity of an ion-exchange membrane was determined using a static membrane potential measurement. The experimental set up consists of a two-compartment cell separated by the testing membrane with an effective area of 4.8 cm^2. Two aqueous solutions of 0.1 M and 0.5 M NaCl were placed in each cell along the sides of the test membrane. The potential difference over the membrane was measured at room temperature with two Ag/AgCl reference electrodes (Hanna Instruments, USA) using a multimeter (Tektronix, USA). The permselectivity can be calculated from the ratio of the measured membrane potential ($\Delta V_{measured}$) over the theoretical membrane potential ($\Delta V_{theoretical}$) as shown in equation (4):

$$\alpha(\%) = \frac{\Delta V_{measured}}{\Delta V_{theoretical}} \times 100 \quad (4)$$

where α is the membrane permselectivity (%), $\Delta V_{measured}$ is the measured membrane potential (V) and $\Delta V_{theoretical}$ is the theoretical membrane potential. Note that the theoretical membrane potential is the membrane potential for an ideal 100% permselective membrane, which was estimated to be 0.0379 V from the Nernst equation.[38]

4.3.6. RED membrane performance

The RED performance of the synthesized membranes was tested in a RED stack described in previous study.[147] The RED stack used in this study initially consists of three

cell pairs, each containing a cation exchange membrane (CSO) and an anion exchange membrane (ASV) (Selemion, Japan) and the CSO membranes were replaced later with the synthesized membranes for a comparison. Each membrane has an effective area of 4 cm × 9 cm. A CEM was placed at each end of the stack as a shielding membrane. Titanium mesh end electrodes coated with iridium plasma were used as the anode and cathode. For the electrode rinse solution, we used a solution of NaCl (0.25 M) with $K_4Fe(CN)_6$ (0.05 M) and $K_3Fe(CN)_6$ (0.05 M). The intermembrane distance was determined by woven fabric spacers (porosity 60%) at a thickness of 250 μm, which was placed between each membrane to form water compartments for the synthetic seawater and river water solutions to pass through. The synthetic feed water had a concentration of 0.5 M NaCl for seawater and 0.017 M NaCl for river water. The feed solutions for both waters were delivered using Masterflex peristaltic pumps (Cole-Parmer, USA) through the RED stack at various flow rates.

A four electrodes configuration allows performance evaluation of the RED stack using an Autolab potentiostats (Metrohm, The Netherlands) in the galvanostatic mode. At each flow rate, the voltage (E) as function of the electrical current (I) was measured. From the measured E-I curves, the gross power generation was calculated. The corrected gross power was determined by subtraction of the power generated in a blank run, which was tested with only one commercial CEM in the stack.

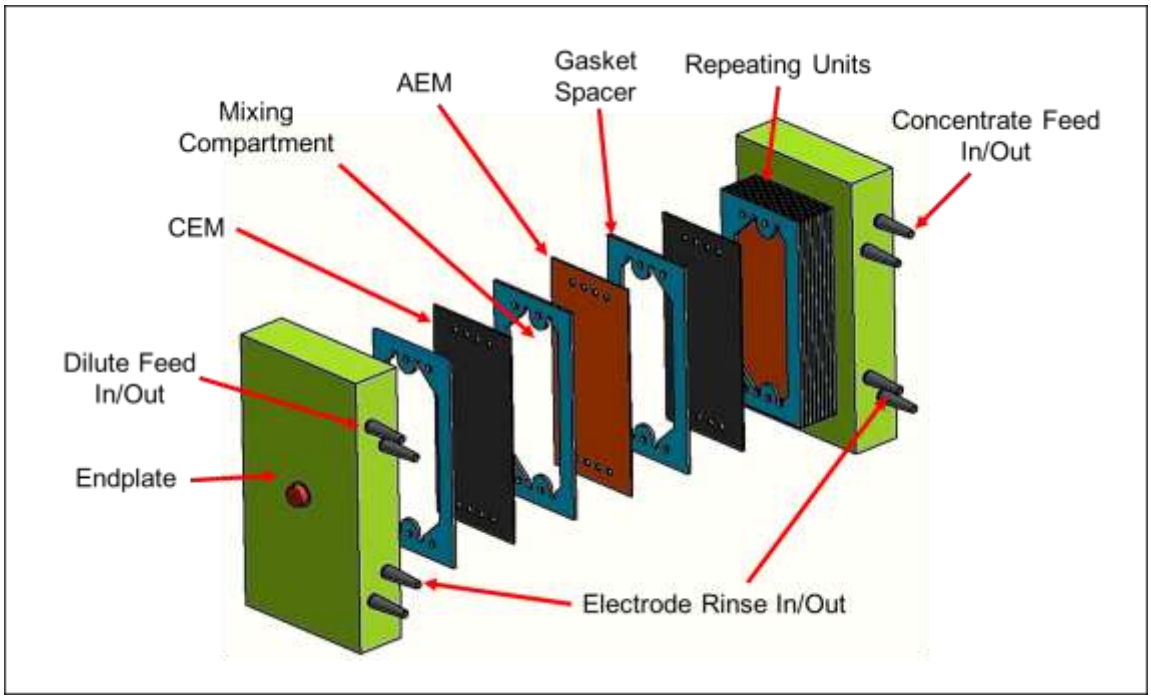

Figure 4.1. Scheme of the RED stack used in performance test. Note that the number of cell pairs used in the performance test is different to what is presented in this illustration.

4.4. Results and discussion

4.4.1. FTIR spectra study

FTIR spectra were obtained from nanocomposite membrane film samples. All the spectra show C-H stretch of CH_2 and CH_3 throughout 2868 and 2970 cm^{-1} and C-O-C stretch at 942 cm^{-1}, which represent the original PPO polymer. As shown in Figure 4.2, the characteristic absorption band for the presence of the $–SO_3H$ substitute to PPO aromatic rings was appeared by the FTIR peak at 1060 cm^{-1} that is formed from the sulfonation reaction. Also a broadband associated with hydrogen reaction between –OH groups and $–SO_3H$ were visible throughout 3300 and 3500 cm^{-1} for all the sPPO membranes. IR vibration bands for the characteristics of S=O stretching for the sulfate (SO_4^{2-}) groups attached to the iron oxide were observed at 1400 cm^{-1} (Figure 4.2 b-f). Overall, these confirm the successful sulfonation of the PPO polymer and iron oxide nanoparticles and the presence of ion exchangeable groups in these organic and inorganic components.

4.4.2. Morphology of the nanocomposite IEMs

The sulfonated iron oxide (Fe_2O_3-SO_4^{2-}) was prepared based on previously reported procedure.[104] The nanoparticles were treated in sulfuric acid before it was mixed with the prepared polymer solution, sPPO. The image of sulfonated Fe_2O_3 particles was observed on a scanning electron microscopy (Figure 4.3), which indicates the particle sizes of 10-50 nm. Nanocomposite membranes were formed by mixing the sulfonated iron oxide (Fe_2O_3-SO_4^{2-}) nanoparticles and the sPPO polymer matrix via blending method and solvent evaporation. SEM was used to observe the morphology of the synthesized Fe_2O_3-PPO cation exchange membranes. Figure 4.4 shows the cross-sectional surface

morphologies of the obtained nanocomposite membranes. It is clearly recognized that the cross-sections were all dense structure without apparent large porosities. Note that settling of the particle in the membrane was not observed.

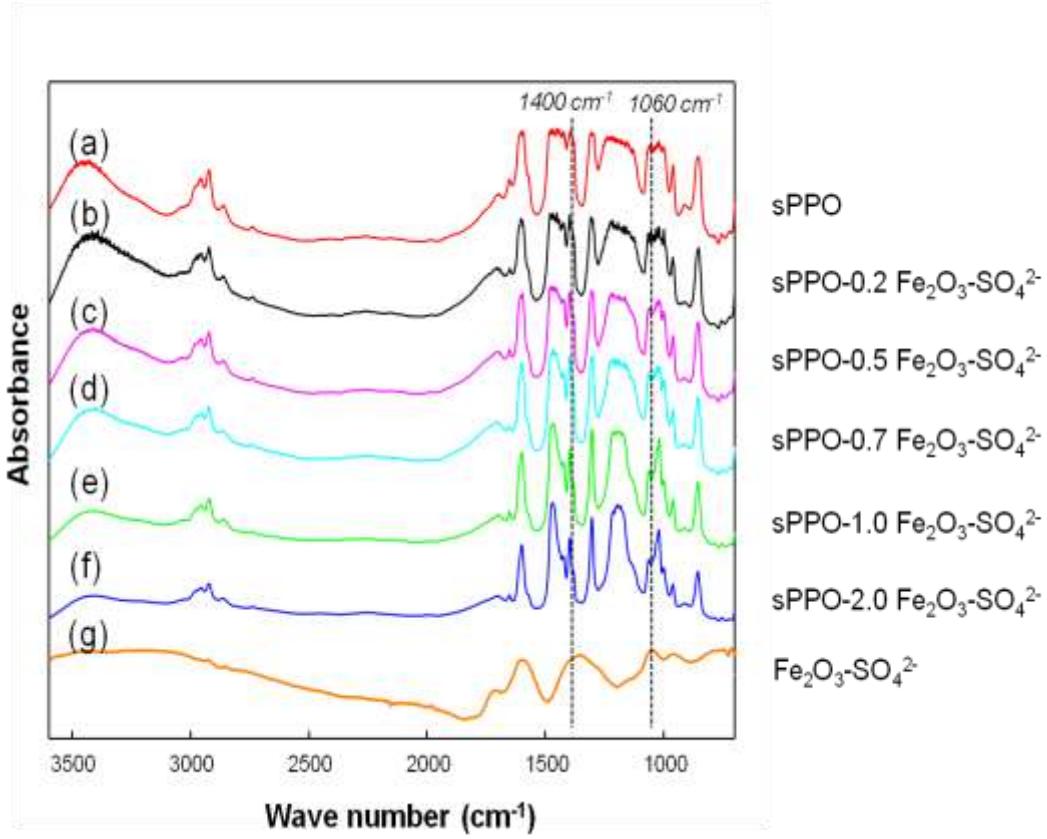

Figure 4.2. FTIR spectra of nanocomposite membranes: (A) Pristine, (B) 0.2 wt% Fe_2O_3-SO_4^{2-}, (C) 0.5 wt% Fe_2O_3-SO_4^{2-}, (D) 0.7 wt% Fe_2O_3-SO_4^{2-}, (E) 1.0 wt% Fe_2O_3-SO_4^{2-}, (F) 2.0 wt% Fe_2O_3-SO_4^{2-}, (G) Fe_2O_3-SO_4^{2-}.

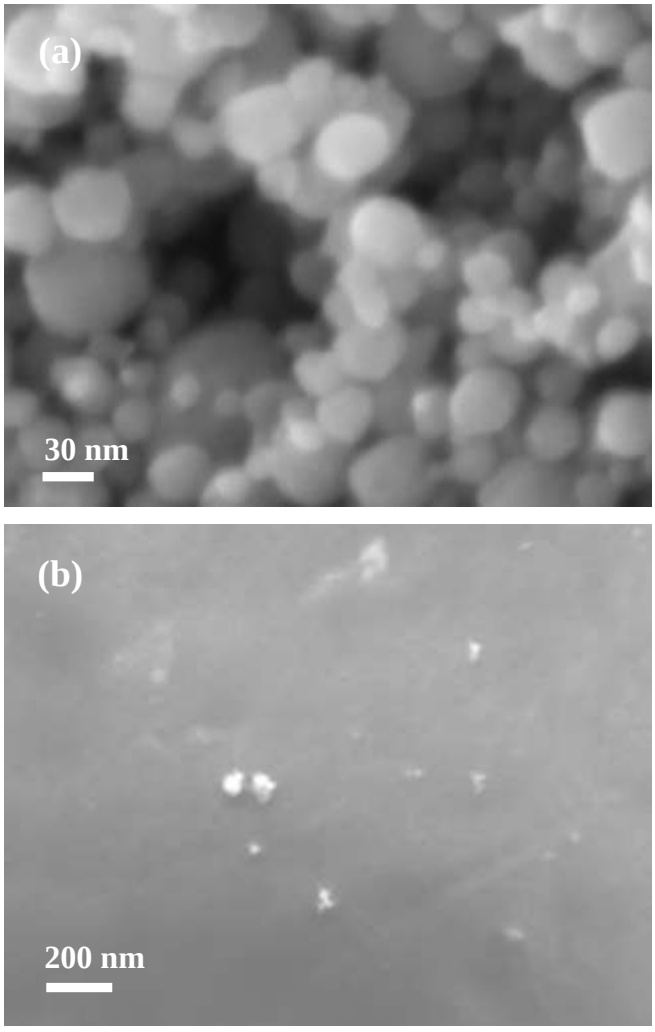

Figure 4.3. SEM micrographs of (a) sulfonated iron oxide particles, Fe_2O_3-SO_4^{2-} and (b) composite membrane with Fe_2O_3-SO_4^{2-}.

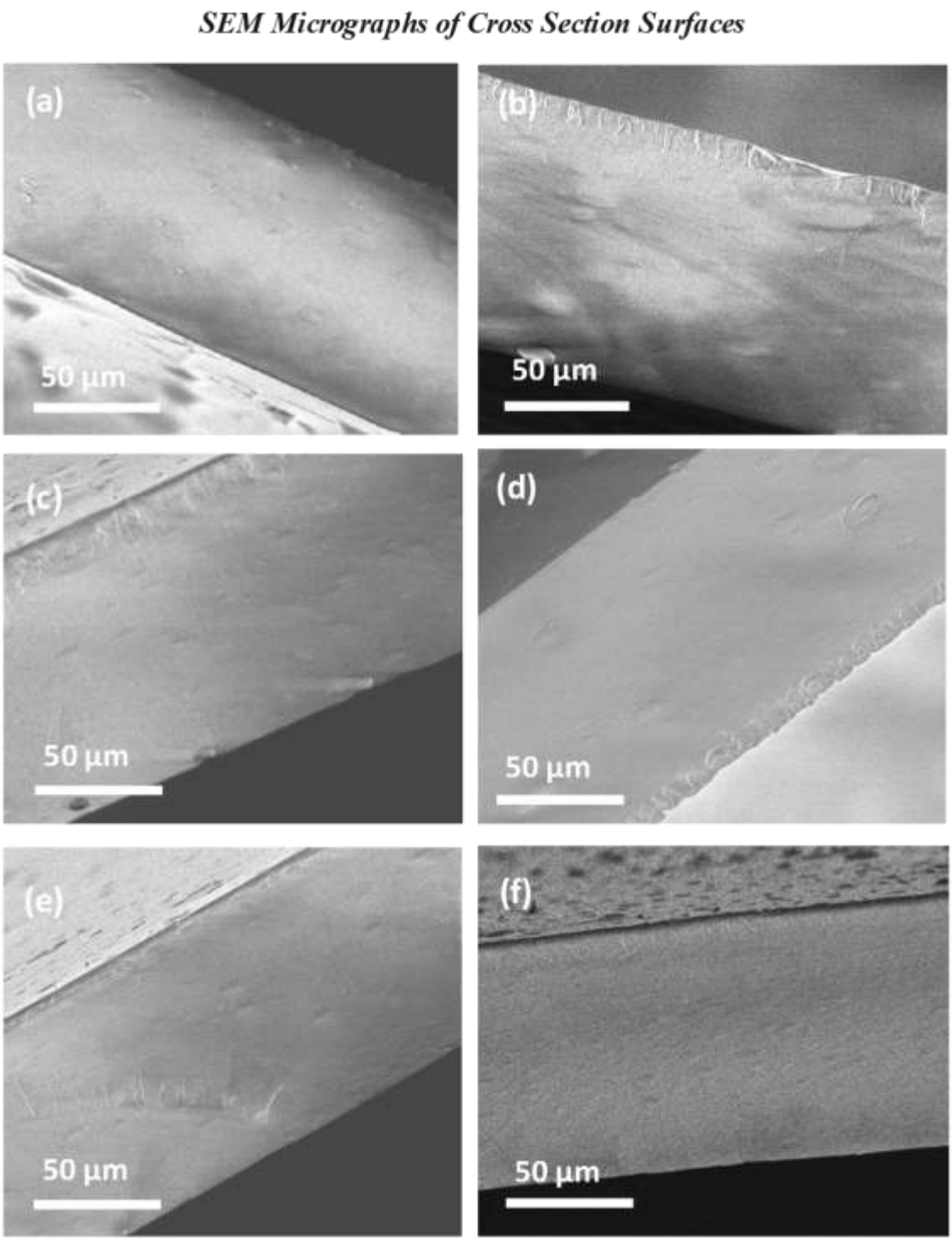

Figure 4.4. SEM micrographs of cross section surfaces: (a) pristine sPPO membrane, (b) composite sPPO-0.2 wt% Fe_2O_3-SO_4^{2-}, (c) composite sPPO-0.5 wt% Fe_2O_3-SO_4^{2-}, (d) composite sPPO-0.7 wt% Fe_2O_3-SO_4^{2-}, (e) composite sPPO-1.0 wt% Fe_2O_3-SO_4^{2-}, and (f) composite sPPO-2.0 wt% Fe_2O_3-SO_4^{2-}.

4.4.3. Effect of nanoparticle loading on electrochemical properties

sPPO membranes were hybridized with Fe_2O_3-SO_4^{2-} at various concentrations between 0.2 and 2.0 wt%. Table 4.1 lists characteristics of the IEMs that are key to investigating their potential performance in a RED system. Prepared nanocomposite membranes were evaluated for permselectivity, area resistance, IEC, SD, and charge density. Each electrochemical property test was performed three times to ensure reliable data, and the values are listed in Table 4.1. The errors are less than 5% and omitted in the table to avoid confusion. In addition, a ratio, P^2/R (also referred to as the performance potential ratio), which derives simply from permselectivity (P^2) over area resistance (R), is also presented. IEMs are often selected on the basis of their high permselectivity and low resistance; thus, we assume that P^2/R is a useful indicator of the best-performing membranes for power generation. Considering that which membrane property dominates RED system performance is not yet fully known and the relationships between these properties are not clearly understood, P^2/R can be an indication only of power generation potential associated with permselectivity and resistance. The properties of the commercial CEM, CSO (Selemion, Japan), were also evaluated for comparison.

The IEC and SD of charged membranes are the key parameters that affect the degree of charge density. The IEC and SD of the membranes increased as the Fe_2O_3-SO_4^{2-} concentration increased within the range of 0–0.7 wt% (Figure 4.5). The increase in SD was expected with the increase of inorganic filler loadings. However, further increase of Fe_2O_3-SO_4^{2-} concentration (> 0.7 wt%) did not continue to increase the swelling degree. This may be attributed to the interaction among the particles that lead

particle aggregation, and thus interrupt the functional groups of the polymer matrix. An increasing trend of IEC with nanoparticle loading can be explained by the increase of negatively charged functional groups in the polymer matrix; attracting more cationic species while repelling anionic species. The increased IEC leads to enhanced ion-conducting character of the nanocomposite. The greater number of fixed charges (negative charges in case of CEM) in the membrane gives rise to enhanced transport properties, which increase the hydrophilic nature of the membrane. Thus, the membrane swells more.[148] In general, the greater swelling can lead to lower mechanical strength and stability; however, several studies have reported that organic-inorganic nanocomposites enhance the mechanical properties of the material. [79, 101, 108] Moreover, the IEC did not continue to increase as more Fe_2O_3-SO_4^{2-} (>0.7 wt%) is incorporated. This phenomenon may stem from the tendency of inorganic nanoparticles to aggregate and thus to disrupt the functional groups of the polymer matrix when excess inorganic nanoparticles are present. Specifically, when inorganic fillers form large cluster, surface of functional groups reduce thus, started to interfere with the charged functional groups of the polymer matrix. Moreover, the ion-exchangeable functional groups contributed from sPPO could also be reduced, as more inorganic nanoparticles agglomerate (>0.7wt% Fe_2O_3-SO_4^{2-}) in the composite. Consequently, the IEC as well as other charge transport properties could be affected by excess nanoparticle loading to decrease the overall membrane performance. [149, 150]

Table 4.1. Characteristics of the prepared membranes compared with a commercial membrane, CSO for RED performance.

Membranes	Permselectivity [%]	Resistance [Ω cm^2]	P^2/R[1]	IEC[2] [meq. g dry^{-1}]	SD[3] [%]	CD[4] [meq. g H_2O^{-1}]
0 Fe_2O_3-SO_4^{2-}	79.13	2.05	3054.4	0.96	21	4.6
0.2 Fe_2O_3-SO_4^{2-}	84.41	1.09	6536.7	1.00	20	5.0
0.5 Fe_2O_3-SO_4^{2-}	87.21	0.87	8742.1	1.12	22	5.1
0.7 Fe_2O_3-SO_4^{2-}	87.65	0.97	7920.1	1.40	26	5.4
1.0 Fe_2O_3-SO_4^{2-}	87.04	1.18	6420.3	1.03	20	5.2
2.0 Fe_2O_3-SO_4^{2-}	68.58	1.58	2976.7	0.87	25	3.4
CSO	92.32	2.26	3771.2	1.04	16	6.4

[1] Performance potential ratio presented by permselectivity (P) over area resistance (R). [2] Ion-exchange capacity. [3] Swelling degree. [4] Charge density.

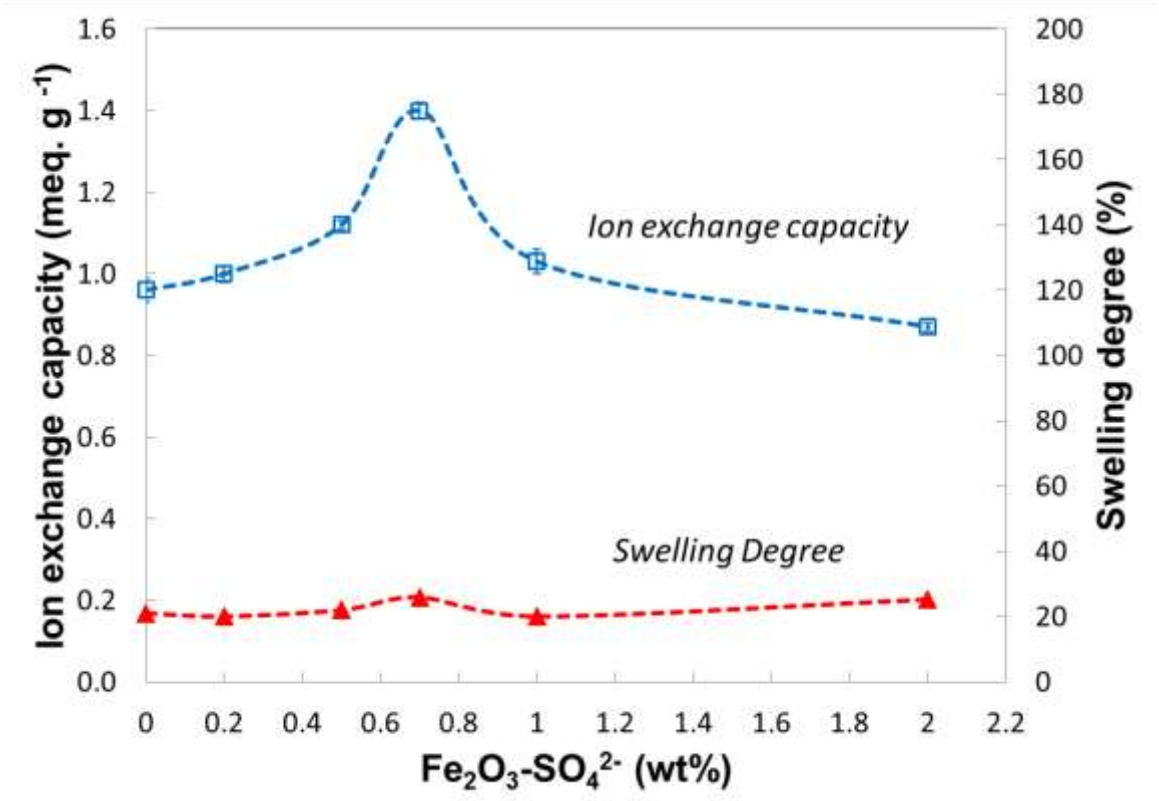

Figure 4.5. Ion-exchange capacity and swelling degree of sPPO membranes as a function of Fe_2O_3-SO_4^{2-} wt%.

The charge density of the membrane has a great effect on its ion permselectivity and area resistance.[25] The number of charged functional groups per water molecule absorbed in the membrane determines the degree of charge density. At a high charge density, more effective ion discrimination is possible (co-ion exclusion). In our experiment, we observed a decrease of area resistance with increasing charge density (Table 4.1). However, we often observe other random behavior that the resistance increases with increasing fixed charge density [25, 42]. This phenomenon may be attributed to a high degree of cross-linking, which improves the mechanical strength of the membranes and thus increases in its resistance. Moreover, the pore formation and surface roughness of the composite have also been reported to affect the transport of ions, permselectivity and conductivity [151]. Thus, such membrane surface properties may contribute to this random tendency. However, the effect of these properties will be further investigated in future studies.

Referring to the result that the IEC increased with the increase of Fe_2O_3-SO_4^{2-} concentrations to certain point (0.7 wt %), the fixed charge density also was increased in similar manner (Table 4.1). As more ionic groups are present (fixed charges), the more swelling occurs, so low area resistances are normally expected with a high swelling degree. However, it is not always the case with a high IEC that results low resistance.[42] 0.7 wt% Fe_2O_3-SO_4^{2-} with the highest IEC and SD showed higher resistance than that of 0.5 wt% Fe_2O_3-SO_4^{2-} (by 11%). The pristine (0 wt%) and 0.2 wt% membranes have reasonable IEC and SD, but with a high area resistance; this can be explained by the relatively low charge density of these membranes. Similarly for the commercial CSO

membrane, having high IEC did not result in low area resistance, which again implies that the relationship of IEC and resistance is not always inversely correlated [25, 42].

The ion permselectivity and area resistance of a membrane are often considered as the most important parameters for the selection of effective IEMs in RED power generation. Although the charge density has great impact on membrane permselectivity and resistance, charge density's relationship with each of these parameters is not always linear, but rather varies according to material [25]. The permselectivity of the composite membranes tended to increase up to 0.7 wt% Fe_2O_3-SO_4^{2-}, as expected based on the increasing charge density (Figure 4.6). The stronger co-ion exclusion with a high charge density increases the membrane permselectivity. Conversely, membranes with a lower charge density have weaker co-ion exclusion and thus lower permselectivity. The membranes with the highest permselectivity were those containing 0.5, 0.7, and 1 wt% Fe_2O_3-SO_4^{2-}. Even though 1 wt% Fe_2O_3-SO_4^{2-} had a comparable permselectivity, the highest area resistance was resulted with a low IEC level among these three membranes. In Figure 4.7, P^2/R is illustrated using the relationship of permselectivity and area resistance. On one hand, the membranes with the highest performance potential were those containing 0.5 and 0.7 wt% Fe_2O_3-SO_4^{2-}, which have the lowest area resistance as well as high permselectivity. On the other hand, the pristine and 2.0 wt% Fe_2O_3-SO_4^{2-} membranes were rated as the least effective owing to their high area resistance. Note that this parameter (P^2/R) may only be used as a reference indicator for power generation and cannot fully demonstrate the overall power generation with such a limited information.

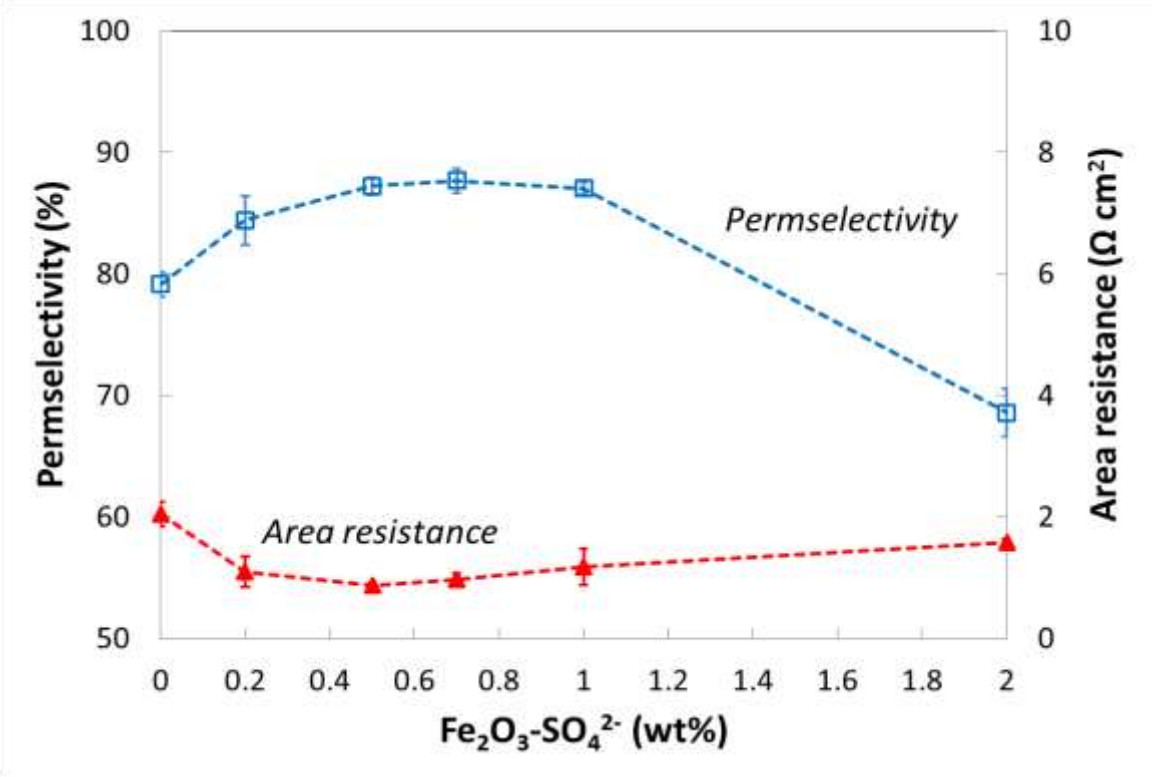

Figure 4.6. Membrane permselectivity and area resistance of sPPO membranes as a function of Fe_2O_3-SO_4^{2-} wt%.

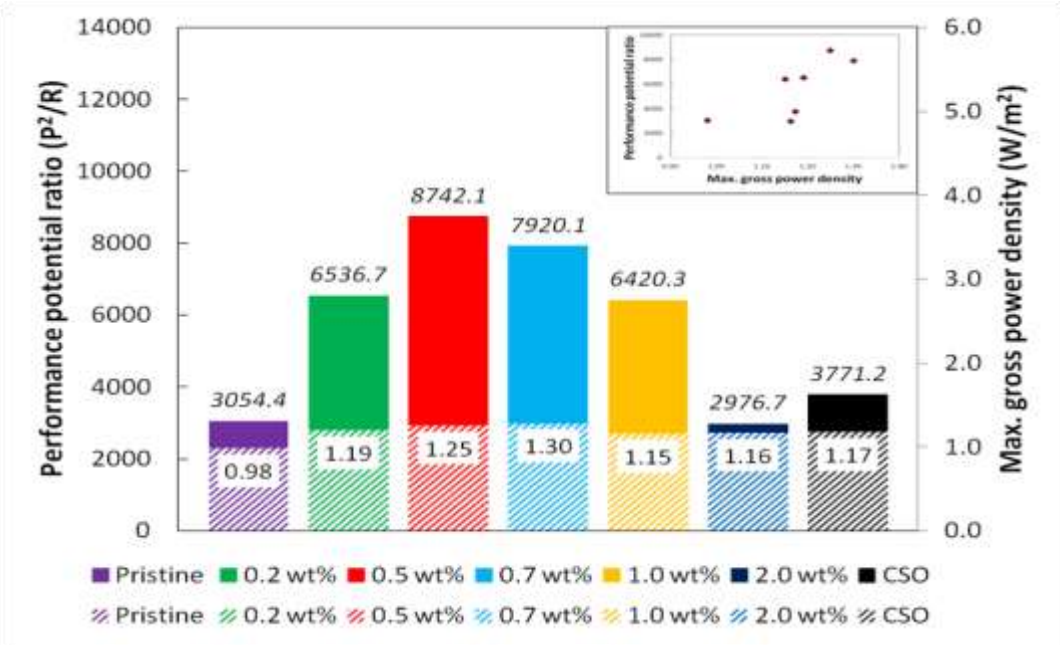

Figure 4.7. Performance potential ratio (P^2/R) (solid bars) vs. maximum gross power density (shaded bars) of nanocomposite membranes.

4.4.4. RED performance of nanocomposite IEMs

All the CEMs under investigation were employed in a RED stack containing an ASV membrane as the AEM. We tested the performance of nanocomposite membranes in RED and compared with the commercial CSO membrane. As mentioned earlier, several researchers stressed the importance of resistance and permselectivity and a direct correlation of area resistance to RED power density [25]. The RED power generation performance was reasonably consistent with the electrochemical properties discussed above. Membrane performance in RED is illustrated using gross power density (W m^{-2}) versus flow velocity (cm s^{-1}) in Figure 4.8. The membranes containing 0.5 and 0.7 wt% Fe_2O_3-SO_4^{2-} exhibited the best performance at various flow rates. A maximum gross power density value of 1.3 W m^{-2} is achieved with 0.7 wt% Fe_2O_3-SO_4^{2-}, which exceeded the level of power density acquired with the commercial CSO membrane. This result aligns well with the electrochemical properties; the high permselectivity of 87.65% and relatively low area resistance of 0.97 Ω cm^2 may play a crucial role in determining the power output. The pristine membrane (0 wt% Fe_2O_3-SO_4^{2-}), however, performed the worst owing to its high resistance (2.05 Ω cm^2) and low permselectivity (79.13%). In addition, the amount of Fe_2O_3-SO_4^{2-} incorporated influences the polymer matrix and its intrinsic membrane properties (IEC, SD, and charge density), and as such may also be a key factor in achieving such a power density. Although, the trend of these properties agreed well in determining the level of RED power density, which factor is most important and the mutual relationship of electrochemical (IEC, SD, charge density, permselectivity and area resistance) and physical properties (porosity, surface roughness) for RED power generation are still unclear. A further investigation on various membrane

materials is necessary to provide a persuasive conclusion on this matter. Nevertheless, the current practice of designing IEMs is a great step toward more practical viability of the RED system to fill the growing energy needs of the world.

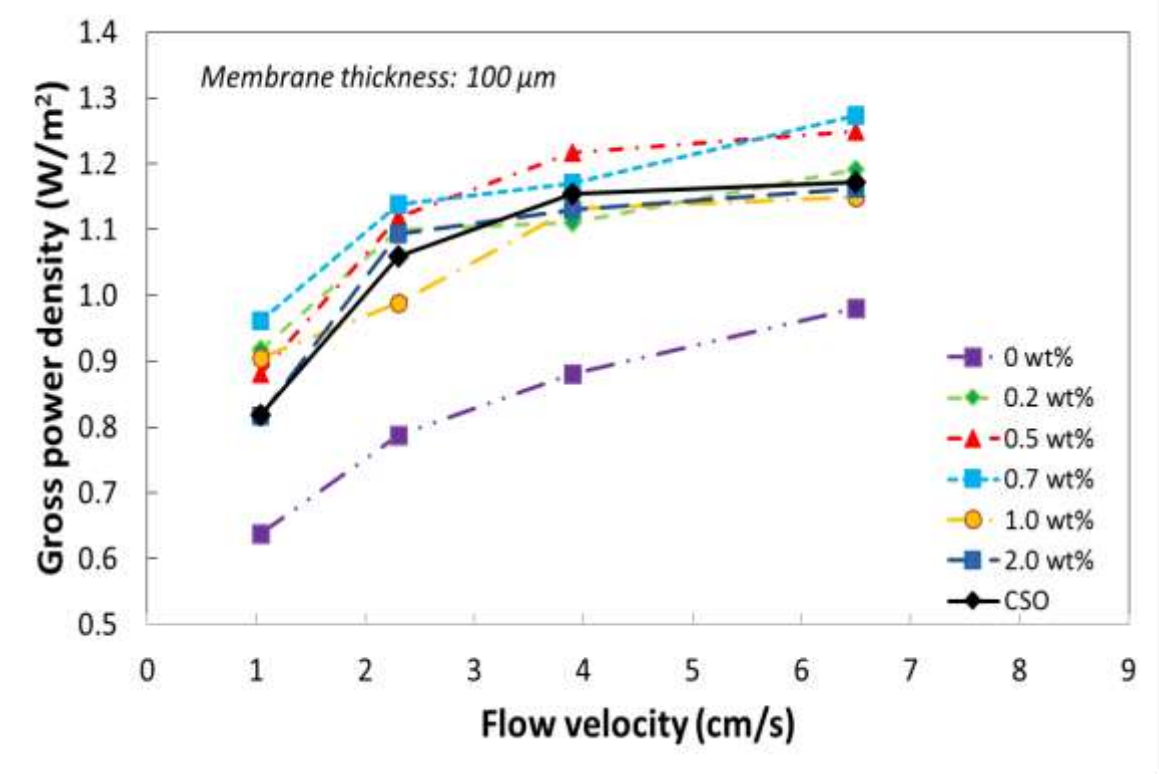

Figure 4.8. Gross power density as a function of flow velocity for the prepared nanocomposite membranes in comparison with the commercial CSO membrane.

4.5. Conclusions

This work emphasizes the importance of membrane role and its characteristics toward the performance of RED system. A new type of organic-inorganic nanocomposite cation exchange membranes was designed and evaluated for electrochemical properties and further tested in a RED stack to investigate its power density generation. We incorporated small amount of sulfonated Fe_2O_3 in sPPO polymer to improve the properties of ion-exchange membranes. In addition, the effect of Fe_2O_3-SO_4^{2-} loading was investigated to optimize the membrane performance in RED. The ion-exchange capacity, swelling degree, area resistance and permselectivity of the membranes were determined for various Fe_2O_3-SO_4^{2-} loadings and were best performed at the range of 0.5-0.7 wt%. By controlling the inorganic filler amount, the nanocomposite membrane was found to be optimized at 0.7 wt% Fe_2O_3-SO_4^{2-} for RED performance, which enables us to generate higher power output than the commercially available CSO membrane. This newly-developed nanocomposite membrane shows the potential to be a feasible candidate for use as ion-exchange membranes in RED power generation. Further investigation to better understand the effect of inorganic fillers on organic polymer as well as the correlation among key membrane properties even in other compositions should be followed in future studies.

CHAPTER 5

EVALUATION OF ELECTROCHEMICAL PROPERTIES AND REVERSE ELECTRODIALYSIS PERFORMANCE FOR POROUS CATION EXCHANGE MEMBRANES WITH SULFATE-FUNCTIONALIZED IRON OXIDE

5.1. Abstract

As IEMs are a key element in a RED system, enhancing their electrochemical characteristics is critical to maximizing system power performance. This chapter presents the preparation of porous nanocomposite cation exchange membranes via a two-step phase inversion technique. The phase inversion process controlled the structural variation (porosity) of the polymeric membranes in the presence of functionalized iron (III) oxide (Fe_2O_3-SO_4^{2-}), which subsequently led to significantly improved electrochemical performance. A porous nanocomposite membrane containing an optimal amount of Fe_2O_3-SO_4^{2-} (0.7 wt%) at a thickness of 30 μm performed best, as it had an area resistance of 0.82 Ω cm^2 and a permselectivity of 85.6%. Application of this membrane in a RED system achieved gross power density of up to 1.4 W m^{-2}, which exceeds the power density obtained with the commercially available CSO (Selemion^{TM}, Japan) membranes. Thus, effective design of ion exchange membranes through structure optimization increases the feasibility of salinity gradient power generation by RED.

5.2. Introduction

Ideal IEMs for optimum RED performance would have high fixed charge density, high ion permselectivity, and low electrical resistance. The fixed charge density is the amount of ion exchange functional groups attached to the membrane per volume of water, and it affects the transport of counter ions through the membranes. The ability to discriminate between ions of opposite charges is required to create chemical potentials and is closely related to the performance of IEMs. Organic-inorganic composite IEMs can adequately provide such properties for RED [37]. However, nanocomposite membranes have gained increasing attention for their remarkable synergized properties as they are expected to have enhanced IEC, conductivity, and permselectivity owing to their homogeneity up to certain level of filler loadings [35]. Although formation of nanocomposites has been well studied, they have not been applied to RED energy generation.

Poly(2,6-dimethyl-1,4-phenylene oxide) (PPO) is a viable candidate for IEMs because it possesses excellent membrane-forming properties, good mechanical and chemical properties, high thermal stability, and low moisture uptake at low cost [152-155]. To enhance the hydrophilicity and IEC of the PPO, a sulfonation reaction was carried out that functionalized the aromatic rings of the polymer chains with charged groups, typically from sulfonic acid. Mixing Nafion® with a variety of inorganic fillers, such as silica, titanium, zirconium phosphates, and ceria, has been widely used for creation of composite membranes, mostly for fuel cell applications [104, 140, 141]. Recently, sulfonated iron (III) oxides (designated as Fe_2O_3-SO_4^{2-} in the following and is not implying 1:1 molar ratio of Fe_2O_3 to SO_4^{2-}) have received increasing attention as inorganic filler materials owing to their versatile characteristics. Sulfonated Fe_2O_3 is strongly hydrophilic

and has large specific surface area owing to the SO_4^{2-} group on the Fe_2O_3 surface, which makes it easier to incorporate the compound into the polymer membrane matrix [139]. In the previous chapter, we used the solvent evaporation technique to prepare a series of new organic-inorganic composite IEMs using Fe_2O_3-SO_4^{2-} nanoparticles in the sPPO polymer matrix. The resulting highly dense structured membranes had fine electrochemical characteristics [37]. Structural modification of a membrane often influences its ionic transport capability and electrochemical performance [58]. In this chapter, we present pore-induced nanocomposite membranes using sulfonated PPO and iron oxide via two-step phase inversion. Highly viscous polymer solutions were used to tailor porous membrane structures of various thicknesses, inorganic nanoparticle loadings, and aging (evaporation) time. We focus on the range of inorganic nanoparticle loadings at 0 ~ 0.7 wt% based on the results of our previous work. The membranes containing 0.7 wt% Fe_2O_3-SO_4^{2-} was best performed in RED stack with enhanced electrochemical properties, but the membrane performance did not continue to improve as more filler loading was incorporated. This phenomenon was found to be the effect of particle aggregation, which disrupted the functional group of the polymer matrix. In addition, two evaporation time was selected to tailor the porosity, expectedly to observe the differences in the degree of pore formation at two distinct aging time, thus better comparison of different pore structure should be expected. The effect of such structural modifications of the nanocomposite membranes on ionic transport characteristics and electrochemical properties was investigated and its impact on RED power generation tested.

5.3. Materials and methods

5.3.1. Preparation of the material

PPO sulfonation was carried out, based on the procedure described elsewhere [37, 156], in a chloroform solvent using chlorosulfonic acid as the sulfonating agent (Figure 5.1). The fine Fe_2O_3 nanoparticle powder (Aldrich, <50 nm) was sulfonated by concentrated sulfuric acid (98%). The required amount of Fe_2O_3 was placed in 0.25 M concentrated H_2SO_4 (98%) at room temperature for 24 h. The sulfonated Fe_2O_3 was then filtered at bottle-top filter unit using a diaphragm pump (2032, Welch) and dried at 80°C in a vacuum oven for 1 h. The dried product was then calcined at 500°C for 3 h and ground in an agate mortar to obtain a fine red powder.

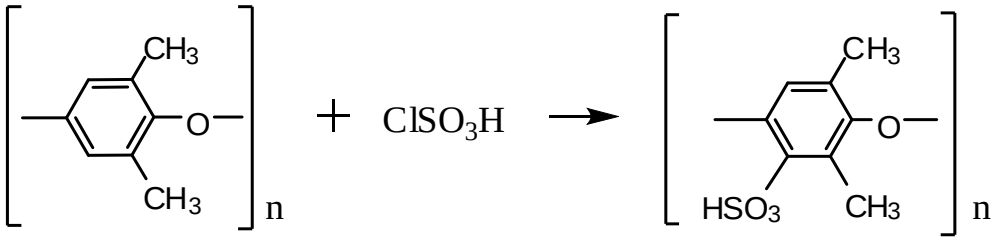

Figure 5.1. Sulfonation of poly(2,6-dimethyl-1,4-phenylene oxide)

5.3.2. Preparation of Fe_2O_3-SO_4^{2-}/sPPO nanocomposite membranes

Fe_2O_3-SO_4^{2-}/sPPO nanocomposite membranes were prepared using a two-step phase inversion method. First, 25 wt% sPPO polymer solutions were prepared using dimethylsulfoxide (DMSO) as the solvent. The sPPO polymer solution was then mixed with various amounts of Fe_2O_3-SO_4^{2-} (0–0.7 wt%) at 40°C for 24 h. The solution was sonicated for 10 min to obtain an optimal dispersion of the particles before it was cast on glass substrates. The doctor blade method was used to obtain the desired thickness of the membrane (30–150 μm). The cast film was then dried in a vacuum oven at 80°C with an aging time of either 10 or 40 min before precipitation in a 60–70°C deionized (DI) water bath. After a few minutes, the film was peeled off the glass substrate. The obtained composite membrane was treated in warm water for 2 h to remove residual solvents and then immersed in 1 M HCl for 24 h. Finally, the membranes were rinsed with DI water and stored in 0.5 M NaCl solution. CEMs with different weight ratios of Fe_2O_3-SO_4^{2-} and thicknesses were prepared and named according to the wt% of Fe_2O_3 added into the polymer matrix and casting film thickness, respectively. The evaporation time was indicated only when it was limited to 10 min (otherwise 40 min). For example, in Table 5.1, sPPO composite membranes containing 0.7 wt% of Fe_2O_3-SO_4^{2-} and having a thickness of 50 μm with 10 min evaporation time were abbreviated as 0.7-50T(10).

5.3.3. Membrane characterization

The physical and electrochemical properties of prepared nanocomposite IEMs were investigated by using procedures described in previous studies to determine their morphology, IEC, SD, charge density, electrical resistance, and permselectivity [34, 38]. The

morphology and structure of the prepared membranes were observed by scanning electron microscopy (SEM, Zeiss Ultra60 FE-SEM).

The IEC was measured using a titration method [53]. Each CEM was immersed in a total of 40 mL of a 1 M HCl for at least 12 h at room temperature and then rinsed with DI water. Note that all the membranes used for this test were at a specific and constant mass. After that, the membrane was immersed in 2 M NaCl solution for 3 h. Subsequently, the hydrogen ions displaced from the membrane were titrated with 0.1 M NaOH solution using phenolphthalein as an indicator. Then the SD was measured by equilibrating the membrane in DI water for at least 24 h before it was wiped with a tissue to remove surface water. The wet weight of the swollen membrane was measured. The membrane was then dried at 50°C in a vacuum oven until a constant dry weight was obtained. The IEC and SD of each membrane were then calculated using equations (1) and (2), respectively. The fixed charge density of the membrane determines co-ion exclusion and counter ion transport (i.e., high ion permselectivity) through the membrane. The fixed charge density, expressed in milliequivalents of fixed groups per gram of water in the membrane (meq. g $_{H2O}^{-1}$), can be determined by dividing the IEC by the SD of the membrane, as shown in equation (3):

$$IEC = \frac{C_{NaOH} \times V_{NaOH}}{W_{dry}} \quad (1)$$

$$SD = \frac{W_{wet} - W_{dry}}{W_{dry}} \times 100\% \quad (2)$$

$$C_{fix} = \frac{IEC}{SD} \quad (3)$$

where C_{NaOH} is the concentration of NaOH solution (M) and V_{NaOH} is the volume of NaOH solution. W_{dry} and W_{wet} are the weight of the dry and the wet membrane, respectively.

A two-compartment cell was used for the electrical resistance of the membrane. The resistance of each membrane was measured at room temperature by impedance spectroscopy (IS) using a Vertex Potentiostat/Galvanostat (Ivium Technologies, The Netherlands) in a frequency range of 10–10^5 Hz with an oscillating voltage of 0.1 V amplitude [45]. Then the membrane resistance was calculated by subtraction of the resistance measured without a membrane from the resistance measured with the membrane under investigation.

The permselectivity of each CEM was determined by a static membrane potential measurement using a two-compartment cell in which the compartments were separated by the membrane under investigation, which had an effective area of 4.8 cm^2. Aqueous solutions of 0.1 M and 0.5 M NaCl were placed in each of the two cell compartments next to the membrane. The potential difference across the membrane was monitored at room temperature using a multimeter (Tektronix, USA) with two Ag/AgCl reference electrodes. The permselectivity of each membrane (α) was calculated from the ratio of the measured potential ($\Delta V_{measured}$) to the theoretical potential ($\Delta V_{theoretical}$) for an ideal 100% permselective membrane, which was estimated to be 37.91 mV from the Nernst equation:

$$\alpha(\%) = \frac{\Delta V_{measured}}{\Delta V_{theoretical}} \times 100 \quad (4)$$

5.3.4. RED stack

The prepared nanocomposite CEMs of various thicknesses were evaluated in a RED stack. The RED stack used in this study contained titanium mesh end electrodes coated with iridium plasma. The RED stack consists of three cell pairs of AEMs (ASV) and CEMs (CSO) (Selemion^{TM}, Japan) and later CEMs were replaced with the prepared nanocomposite CEMs. Each CEM and AEM has an effective area of 4 cm × 9 cm, and an additional CEM was placed at end of the stack as a shielding membrane. An electrode rinse containing 0.05 M $K_4Fe(CN)_6$ and 0.05 M $K_3Fe(CN)_6$ in 0.25 M NaCl was pumped through the cathode and anode compartments at a flow rate of 300 ml min^{-1}. The intermembrane distance was maintained at 250 µm by woven fabric spacers (porosity 60%). The artificial seawater (0.5 M NaCl) and river water (0.017 M NaCl) used as feed solutions were prepared by dissolving NaCl in DI water. The two feed solutions were delivered through the RED stack at flow rates of 38, 115, 191, and 268 ml min^{-1} using Masterflex peristaltic pumps (Cole-Parmer, USA). A four-electrode arrangement with an external Vertex Potentiostat/Galvanostat (Ivium Technologies, The Netherlands) in galvanostatic mode allowed performance evaluation of the RED stack. The voltage (*E*) as a function of the electrical current (*I*) was measured at each flow rate. The gross power generation was calculated from the measured maximum values of *E* and *I*. The gross power output was then corrected by subtraction of the power generated in a blank run with only one CEM in the stack.

5.4. Results and discussion

5.4.1. Membrane morphology

SEM was used to observe the morphology of the synthesized Fe_2O_3-SO_4^{2-}/sPPO CEMs. The top surface (A1-D1) and cross-sectional surface (A2-D2) of the obtained nanocomposite membranes were shown to be porous (Figure 5.2). In general, membrane structures are highly dependent on the preparation method and properties of the casting polymer solution, especially when prepared by phase inversion [58, 157]. Figure 5.2 shows that as membranes contain more inorganic nanoparticles, they exhibit bigger pore sizes and higher porosity. In addition, the membrane prepared with a 10-min evaporation time (Figure 5.2 D1-2) prior to immersion precipitation has significantly larger pore sizes than membranes prepared under the 40-min evaporation condition. The porosity of the prepared membranes (equation 5) also suggests a higher pore volume or free volume fraction in nanocomposite membranes with a higher filler loading amount and shorter evaporation time [58, 103]. The morphology clearly shows the influence on the membrane structure of the inorganic nanoparticles and the two-step phase inversion technique. The effect of membrane structure and thickness on electrochemical properties and thus optimal design is further discussed in the following section.

$$Porosity = \frac{W_{wet} - W_{dry}}{A\delta\rho_w} \tag{5}$$

where W_{wet} and W_{dry} are the weight of the wet and dry membranes, respectively; A is the membrane area; δ is the thickness of the membrane; and ρ_w is the density of water.

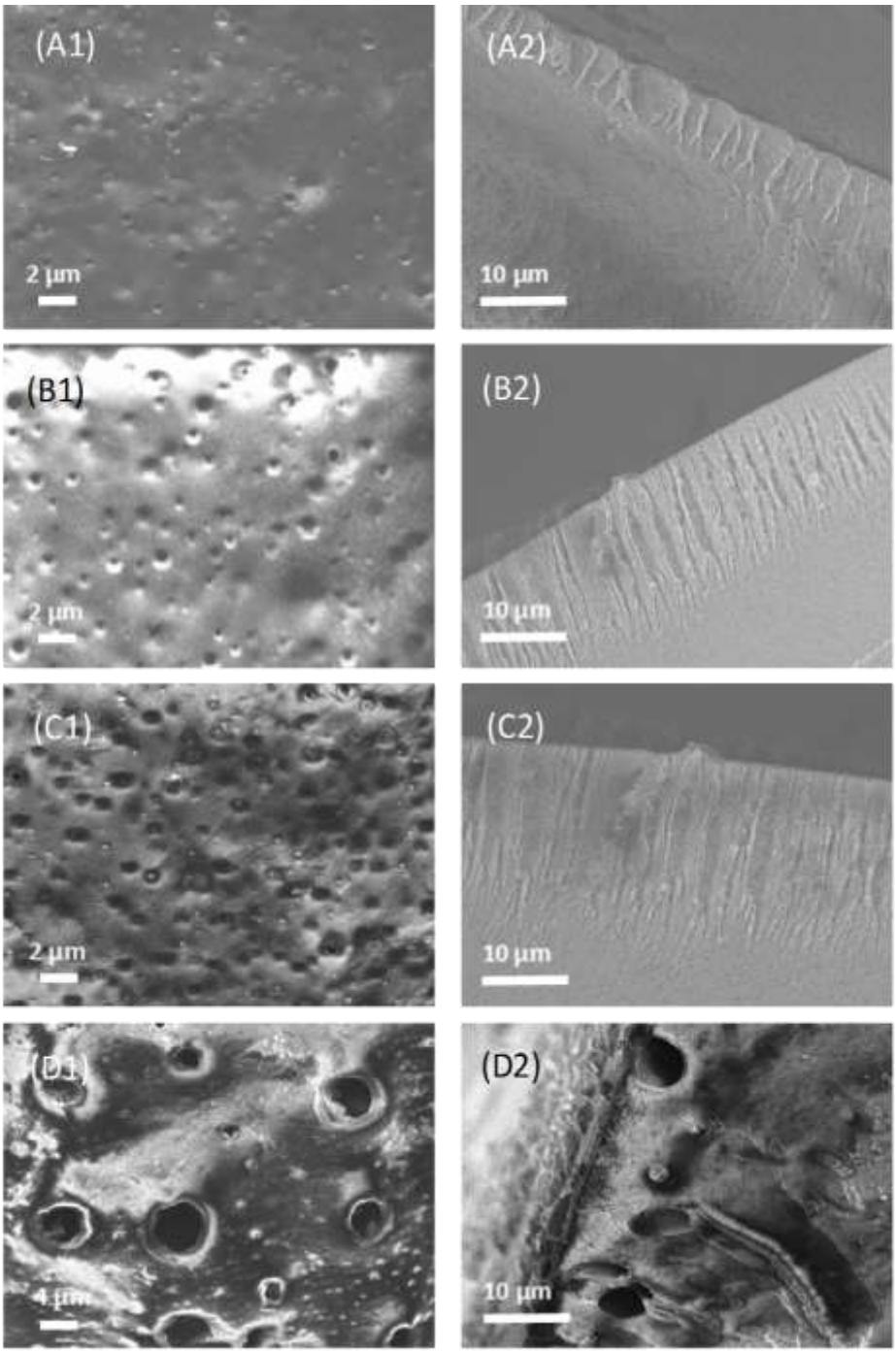

Figure 5.2. SEM micrographs of (A1 and A2) pristine sPPO membrane, (B1 and B2) composite sPPO-0.3 wt% Fe_2O_3-SO_4^{2-}, (C1 and C2) composite sPPO-0.7 wt% Fe_2O_3-SO_4^{2-}, and (D1 and D2) composite sPPO-0.7 wt% Fe_2O_3-SO_4^{2-} with 10 min evaporation time. Note that membranes in (A), (B), and (C) are prepared with 40 min evaporation time.

5.4.2. Electrochemical behavior of the porous nanocomposite IEMs

Nanocomposite sPPO membranes were synthesized with different Fe_2O_3-SO_4^{2-} loadings (0–0.7 wt%) and with various thicknesses (30–150 μm) and their intrinsic electrochemical properties characterized (Table 5.1). As discussed in the previous section, pores formed on the membrane surface during the combined phase inversion processes (i.e., solvent evaporation (dry) and precipitation immersion (wet)), and such pores can affect membrane selectivity and ionic conductivity. Membrane thickness plays an important role in void formation and has a notable impact on electrochemical properties, especially on area resistance [58]. In the previous chapter, nanocomposite membranes loaded with a small amount (0–2 wt%) of functionalized iron oxide (Fe_2O_3-SO_4^{2-}) in their sPPO polymer matrix were synthesized only by solvent evaporation. The 100-μm sPPO membrane with 0.7 wt% Fe_2O_3-SO_4^{2-} nanoparticles exhibited excellent electrochemical characteristics and performed the best in a RED power measurement test. Thus, in this study membranes containing 0.7 wt% Fe_2O_3-SO_4^{2-} were prepared in various thicknesses (i.e., 30, 50, 75, 100, 125, 150 μm) for detailed investigation, whereas membranes containing other concentrations of nanoparticles were prepared in only three different thicknesses (i.e., 30, 75, 100 μm). The permselectivity, area resistance, IEC, SD, and charge density of nanocomposite membranes were studied. Also, the properties of the commercial CEM, CSO (Selemion, Japan), were evaluated for comparison.

IEC and SD are crucial membrane properties that are closely correlated with fixed charge density. A greater quantity of counter ionic groups (fixed charges) present in the membrane leads to higher IEC and enhanced ionic transport properties. As expected, we found that the membranes with higher loadings of Fe_2O_3-SO_4^{2-} exhibited significantly

higher IEC values, whereas the SD values of the membranes varied only slightly at different nanoparticle loadings (Figure 5.3). The membrane thickness did not affect the IEC and SD significantly under different nanoparticle loading conditions. This is because the amount and species of ion exchange groups per unit weight (i.e., capacity) do not depend on membrane thickness. Considering that the SD is determined by the amount of ion exchangeable groups present in the membrane, the similar SDs at different thicknesses is expected. In addition, the IEC and SD of 0.7 wt% Fe_2O_3-SO_4^{2-} membrane with 10 min evaporation time were compared with those of membranes prepared with 40 min evaporation time. As Figure 5.3 shows, the membrane with shorter evaporation time exhibited markedly lower IEC and higher SD. This phenomenon is attributed to the higher porosity of IEMs with shorter evaporation time because high porosity weakens the ability to effectively exclude co-ionic species [158]. Thus, the selectivity of the membrane diminishes and the membrane swells more, which result in lower charge density. However, highly porous membranes often have excellent conductivity (i.e., low area resistance) even as they suffer from low ionic selectivity [58].

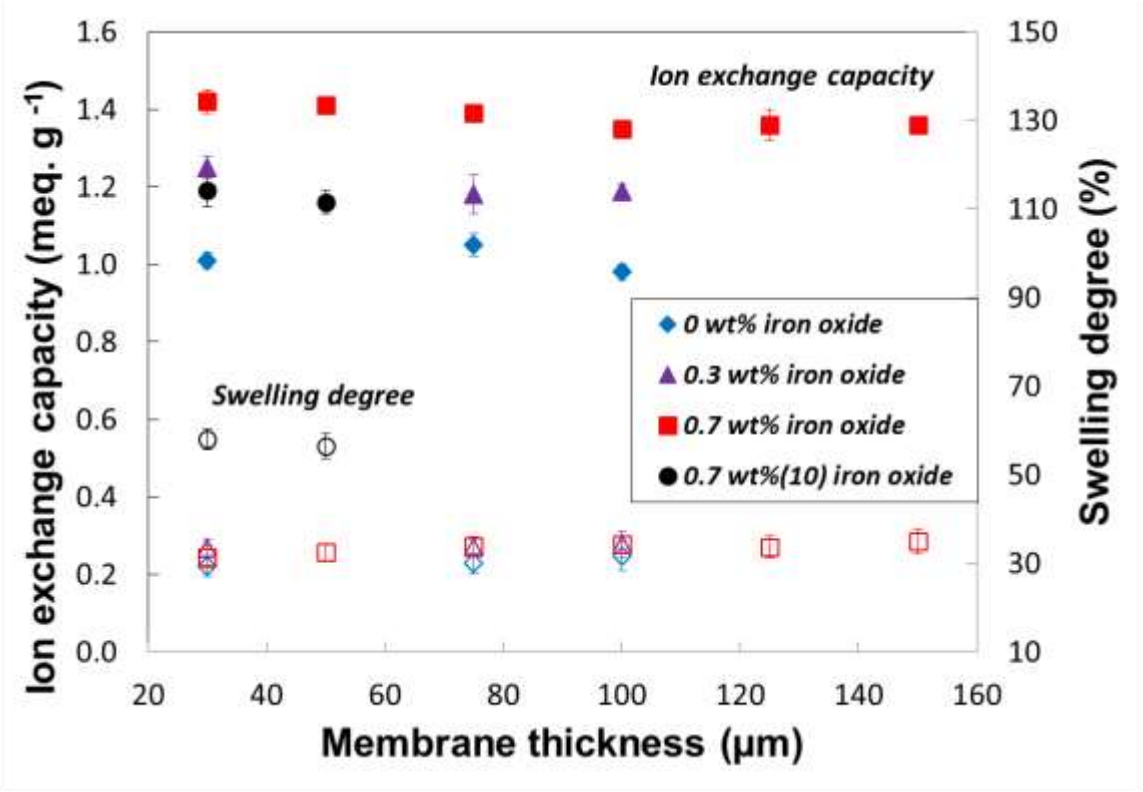

Figure 5.3. Ion exchange capacity (solid symbol) and swelling degree (open symbol) of nanocomposite membranes of various thicknesses. Note that 0.7 wt%(10) represents the membrane with 10 min solvent evaporation time.

The structural variation of IEMs affects their permselectivity and area resistance directly. Prepared nanocomposite membranes of different thicknesses exhibited similar permselectivities, in part because of their similar IECs and SDs, as discussed earlier (Figure 5.4A). This similar permselectivity may also arise because the membranes have the same chemical composition. For instance, membranes with nanoparticle loadings of 0.3, and 0.7 wt% have different membrane thicknesses but comparable permselectivities of approximately 83%, and 85%, respectively (Table 5.1). Additionally, the 0.7 wt%(10) membrane exhibited significantly lower permselectivity than did membranes with longer evaporation time because of its relatively high porosity. The study also supports the hypothesis that membranes with larger pores or higher porosity are generally less selective because the Donnan exclusion of ionic species becomes less valid [58, 158].

However, IEM thickness plays a crucial role in the membrane's ion transport characteristics. Thinner membranes allow faster ion transfer through a conductive medium, and thus low area resistance is expected and is desirable in a RED system [42]. This trend was present in the nanocomposite membranes prepared in this study (Figure 5.4B). Moreover, pore formation within the membrane due to the two-step phase inversion process and functionalized nanoparticles provides more free space in the membrane. These spaces promote the migration of ionic species and thus lower the area resistance of the membrane [150]. As expected, the 0.7 wt% Fe_2O_3-SO_4^{2-} membrane (thickness of 30 μm) exhibited the lowest area resistance and the highest charge density (4.5 meq. g $_{H2O}^{-1}$). The largest area resistance was exhibited by the 0 wt% Fe_2O_3-SO_4^{2-} membrane with a thickness of 100 μm. The area resistance of 0.7 wt% (10) was similar at thicknesses of 30 and 50 μm to those of the membranes with longer evaporation time

(i.e., 40 min). In general, membranes with large pores are more conductive, which leads to a decrease in membrane resistance [58]. However, the low charge density of these membranes (Table 5.1) increases the area resistance even with larger pore formation in the membrane. In addition, the commercial CSO membrane had fine ion transport properties (e.g., IEC and permselectivity), but showed relatively higher area resistance than those of prepared membranes.

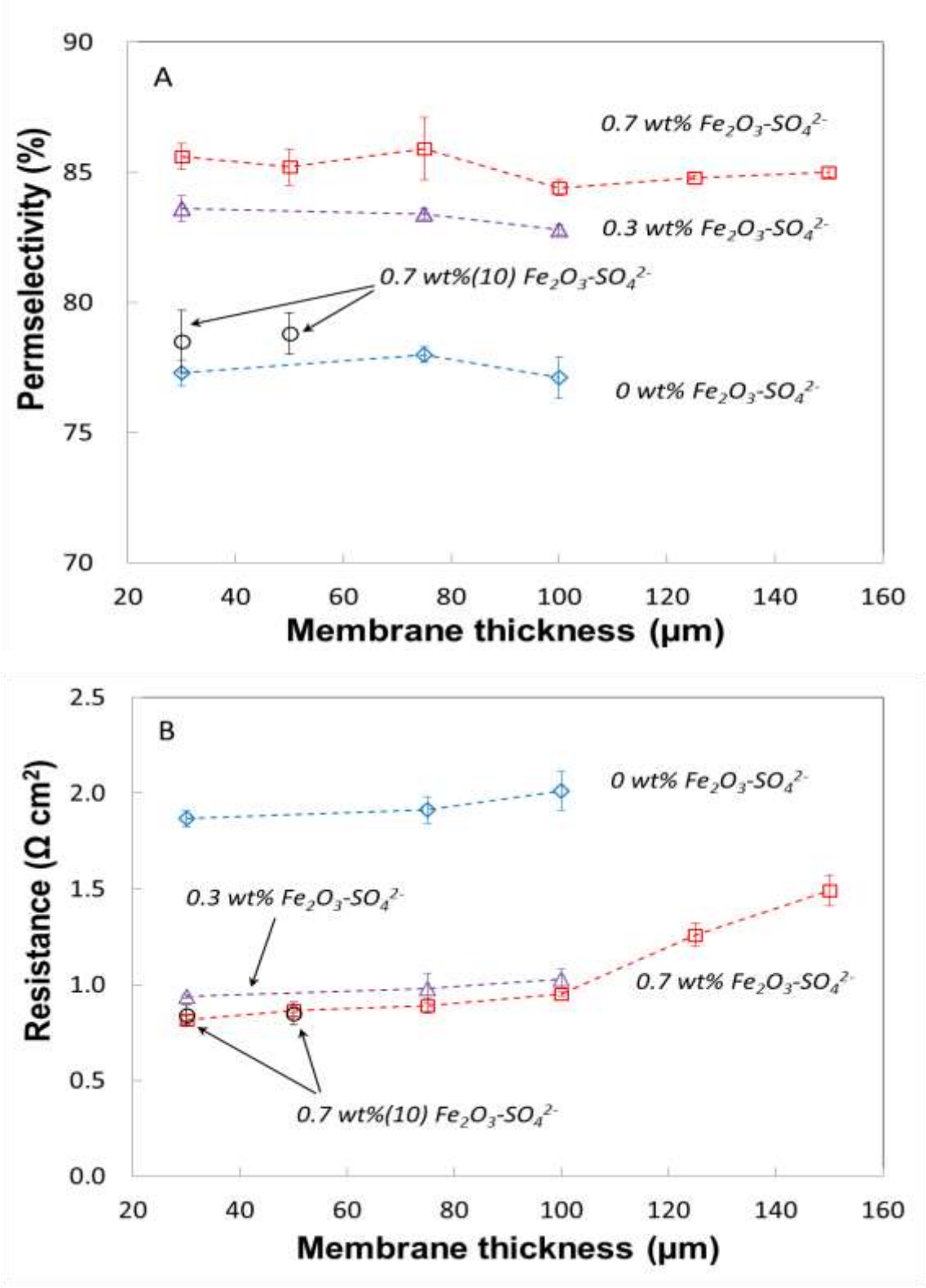

Figure 5.4. Membrane permselectivity (A) and area resistance (B) of nanocomposite membranes at various thicknesses. Note that 0.7 wt%(10) indicates the membrane with 10 min solvent evaporation time and the dotted lines are drawn to guide the eye.

Table 5.1. Characteristics of the prepared membranes relevant for RED performance.

Membranes	IEC [meq. g $_{dry}^{-1}$]	SD [%]	CD [meq. g $_{H2O}^{-1}$]	Permselectivity [%]	Resistance [Ω cm^2]	Porosity
0-30T	1.01	29	3.4	77.3	1.87	0.35
0-75T	1.05	30	3.5	78.0	1.91	0.41
0-100T	0.98	32	3.1	77.1	2.01	0.47
0.3-30T	1.25	33	3.7	83.6	0.94	0.42
0.3-75T	1.18	34	3.7	83.4	0.98	0.45
0.3-100T	1.19	34	3.5	82.8	1.03	0.52
0.7-30T	1.42	32	4.5	85.6	0.82	0.47
0.7-30T(10)[a]	1.19	58	2.0	78.5	0.83	1.09
0.7-50T	1.41	33	4.3	85.2	0.86	0.50
0.7-50T(10)[a]	1.16	56	2.1	78.8	0.85	1.02
0.7-75T	1.39	34	4.1	85.9	0.89	0.53
0.7-100T	1.35	34	3.9	84.4	0.95	0.56
0.7-125T	1.36	34	4.0	84.8	1.26	0.60
0.7-150T	1.36	35	3.9	85.0	1.49	0.62
CSO	1.04	16	6.4	92.3	2.26	N/A

IEC: ion exchange capacity; SD: swelling degree; CD: charge density.

[a] Membranes prepared with 10 min. solvent evaporation time.

At higher charge density, co-ionic species are effectively excluded and membranes are more selective. The larger quantity of ion exchange functionalities leads to higher permselectivity and lower area resistance [38, 58]. We found such interconnected behavior of these properties in the prepared porous nanocomposite CEMs.

In this experiment, we observed a correlation between charge density and permselectivity and area resistance (Figure 5.5): permselectivity increased and area resistance decreased as fixed charge density increased. As shown in Figure 5.5, this direct correlation of intrinsic membrane properties does not depend on membrane thickness. This correlation was expected in the case of the Fe_2O_3-SO_4^{2-}/sPPO composite membranes because they have the same chemistry as well as a comparable degree of IEC, SD, and permselectivity. In other words, when membranes form with different chemistries and degrees of cross-linking, such straightforward relationship may no longer be valid. Moreover, lack of uniformity in charge distribution can also interfere with the transport of counter ions, resulting in independent behavior of the membrane [42, 159].

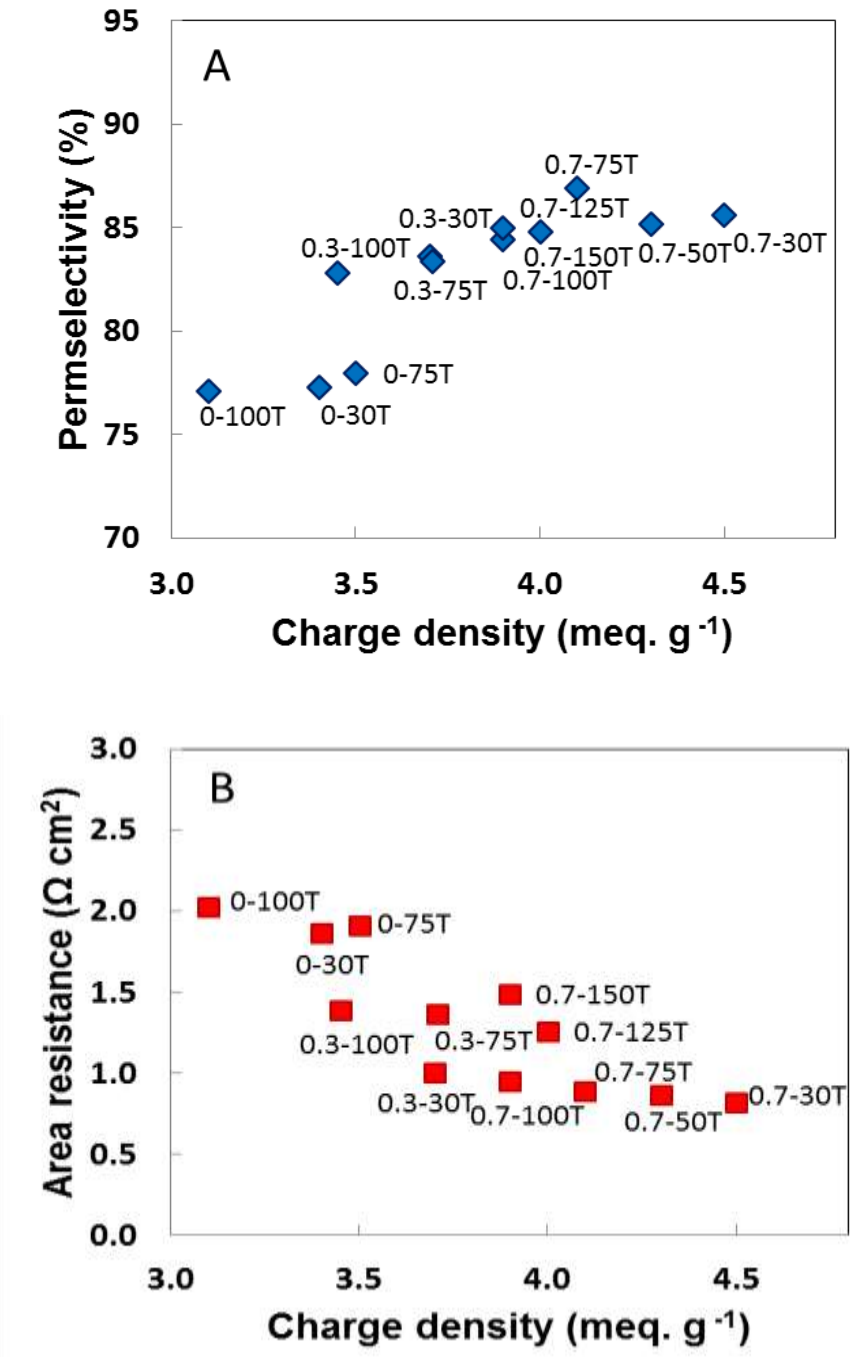

Figure 5.5. Membrane permselectivity (A) and area resistance (B) of nanocomposite membranes as a function of charge density.

5.4.3. RED performance

IEMs are often evaluated on the basis of their permselectivity (high desired) and area resistance (low desired). According to the Nernst equation, the permselectivity (α) and area resistance (R) of the membrane influence the theoretical power density generation (i.e., α^2/R) and thus are often used to determine the power output in a RED system [37, 42]. Figure 5.6 shows the effect of these characteristics of nanocomposite membranes on maximum gross power density generation. The gross power density of the membrane has a more scattered distribution as a function of permselectivity and a more linear relationship versus area resistance (Figure 5.6). This directly reflects the effect of thickness on these characteristics. For example, 0.7-150T, which is located in an outlying region in Figure 5.6A, has high permselectivity but low power density owing to its high area resistance. In the previous section, we observed similar permselectivities for membranes with the same chemical composition (i.e., 0.3, and 0.7 wt% Fe_2O_3-SO_4^{2-}) at different thicknesses. However, we also found a trend of increasing area resistance with increasing membrane thickness and decreasing area resistance with increasing inorganic nanoparticle loading. Therefore, in this work the area resistance plays a more dominant role in power performance and thus has a greater correlation with gross power density (Figure 5.6B).

The membrane performance in RED is presented using gross power density versus flow velocity in Figure 5.7. As expected, the gross power density increased as flow velocity increased because of reduced boundary layer resistance at the membrane surface [39, 42, 160]. Specifically, enhanced mixing at higher flow velocity facilitates more ion transport, and thus lowers internal resistance, which results higher gross power density.

The membrane with a blend ratio of 0.7 wt% Fe_2O_3-SO_4^{2-} with a thickness of 30 μm yielded the highest power density of 1.4 W m^{-2}, which is significantly higher than that of the commercially available CSO membrane. This membrane has excellent electrochemical properties (Table 5.1), which were directly reflected in its high power output, high permselectivity of 85.6%, and relatively low area resistance of 0.82 Ω cm^2. However, the gross power density was reduced by 45% as the membrane thickness increased to 150 μm. In addition to the effect of inorganic nanoparticles on the polymer matrix and physicochemical properties, structural variation was found to be a key driver of the RED power performance.

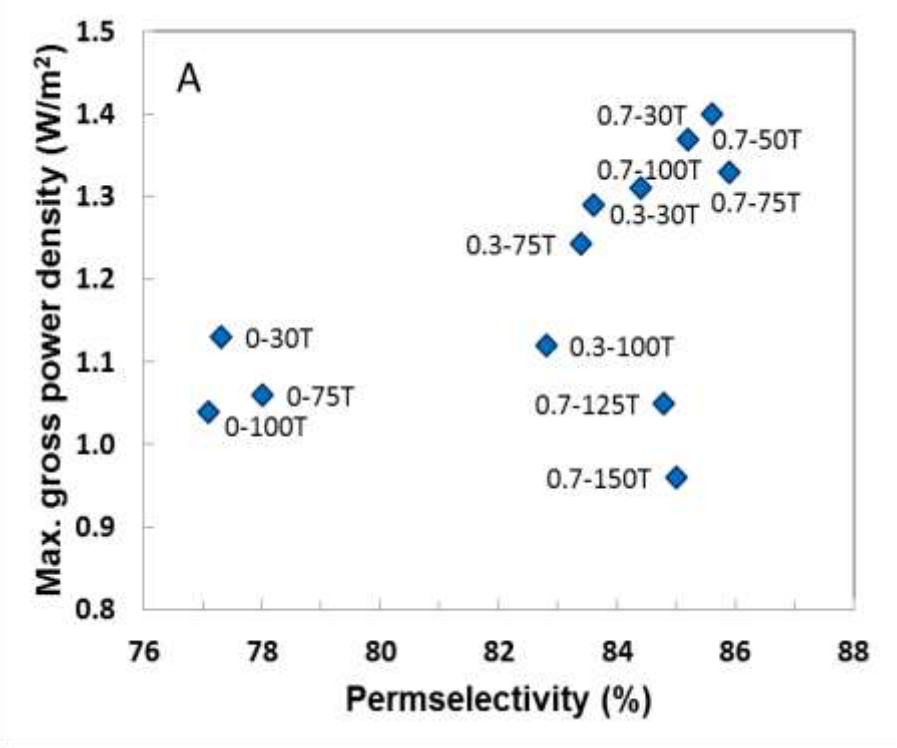

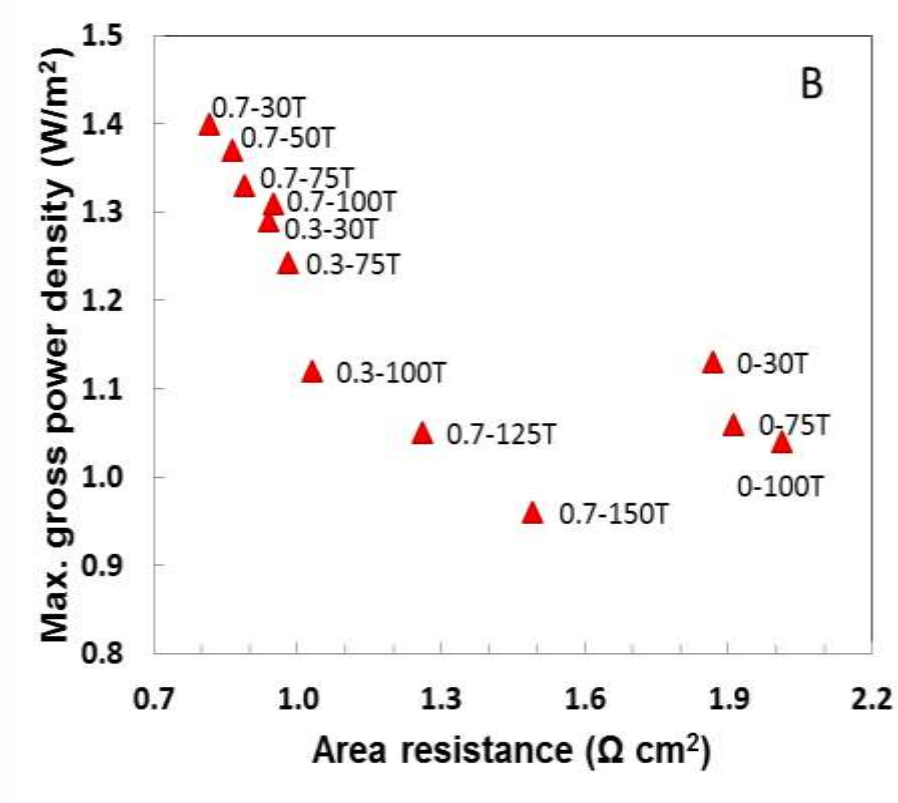

Figure 5.6. Effect of permselectivity (A) and area resistance (B) of nanocomposite membranes on maximum gross power density generation.

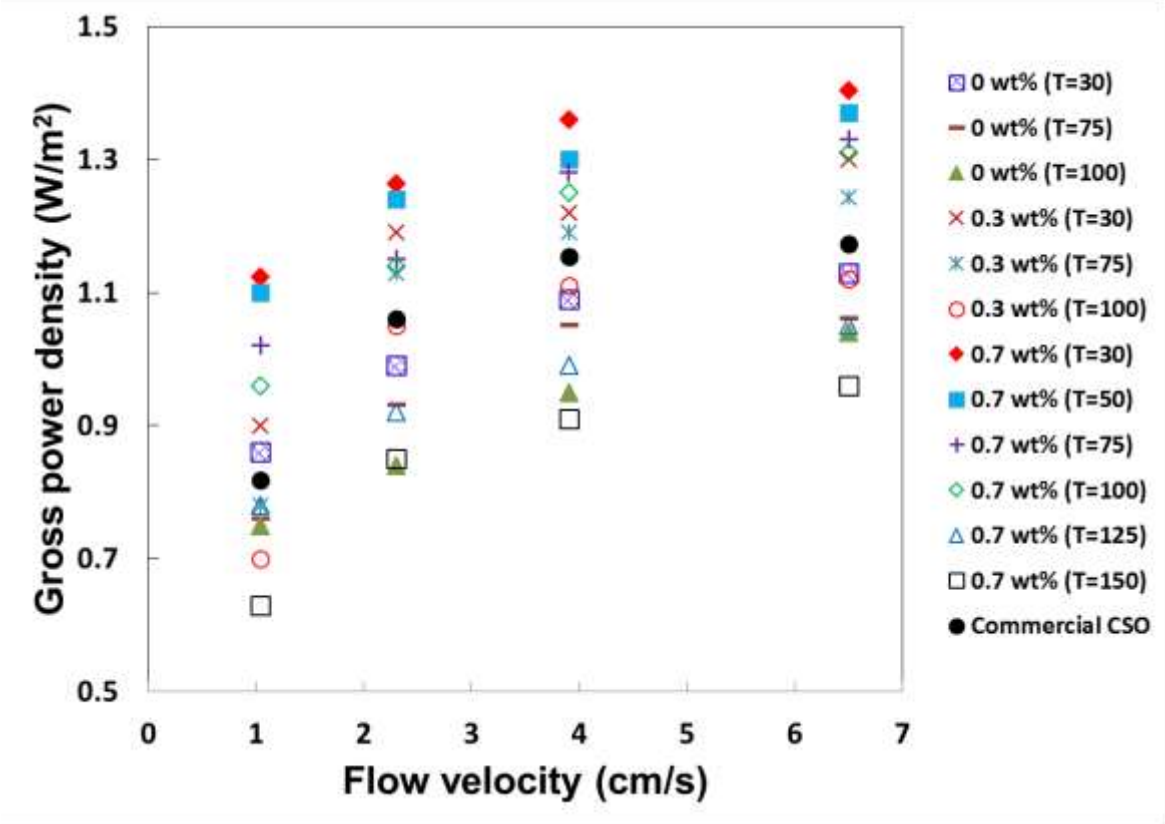

Figure 5.7. Gross power density as a function of flow velocity for the prepared nanocomposite membranes. The performance of the CSO membrane is shown for comparison. T represents the thickness of membranes in micrometers.

5.5. Conclusion

This study demonstrates the importance of tailoring membrane structure and bulk properties for RED power generation. A two-step phase inversion membrane preparation process yielded the desired membrane structure and porosity in the presence of inorganic nanoparticles. Porous nanocomposite membranes were prepared with various thicknesses and evaporation times, and then their electrochemical properties and RED performance were evaluated. The IEC, SD, and permselectivity of the membranes were comparable for various film thicknesses; 0.7 wt% Fe_2O_3-SO_4^{2-} had the most favorable electrochemical properties. Short evaporation time (10 min) led to a structure with markedly large pores but clearly weakened ion transport and selectivity. The membrane's thickness directly affected the area resistance and thus its performance in a RED stack. Relatively lower area resistance was achieved with thinner porous membranes, which had the highest gross power density (1.4 W m^{-2}) in a RED stack. Tailoring key structural properties of the membrane play a significant role in ionic transport, resulting in higher RED power performance. Therefore, structural optimization of the membrane in combination with use of functionalized nanoparticles shows great potential and provides valuable insights as a feasible pathway to IEM development for a RED power generation process.

CHAPTER 6

EFFECT OF INORGANIC FILLER SIZE ON ELECTROCHEMICAL PERFORMANCE OF NANOCOMPOSITE CATION EXCHANGE MEMBRANES FOR SALINITY GRADIENT POWER GENERATION

6.1. Abstract

In this chapter, we present the preparation of organic-inorganic nanocomposite CEMs containing sulfonated polymer, poly (2,6-dimethyl-1,4-phenylene oxide), and sulfonated silica (SiO_2-SO_3H). The effect of silica filler size at various loading concentrations on membrane structures, electrochemical properties, and the RED power performance is investigated. The membranes containing larger fillers (70 nm) at 0.5 wt% SiO_2-SO_3H exhibited a relatively favorable electrochemical characteristic for power performance: an area resistance of 0.85 Ω cm^2, which is around 9.3% lower than the resistance of the membranes with smaller particle fillers (15 nm). The power performance of this nanocomposite CEM in a RED stack showed the highest gross power density of 1.3 W m^{-2}: 10% higher power output compared with the membranes containing small particle size and 21% higher than that of commercially available FKS membrane. The goal of the present work is to develop an effective design for tailor-made CEMs for RED applications. Thus, a further optimized combination of material properties and membrane structure appears to be a viable option for the development of nanocomposite ion exchange materials that could provide greater power production by RED.

6.2. Introduction

The concept of combining organic polymer and inorganic nanoparticles to form composite membranes have gained much interest in the development of IEMs owing to the ability to retain RED-desired properties (e.g., low resistance) from both components. The aim of incorporating inorganic filler materials in polymer-based materials is often to enhance mechanical, chemical, and thermal stability of polymer matrix. However, their synergy can also provide extra ion exchange functional groups to the membrane, which helps more ion migration, and thus allows improved conductivity as a single molecular composite [37, 161]. In fact, the structural properties of the membrane often influences its ionic mobility and electrochemical performance [162]. Organic-inorganic composite IEMs with controlled porosity exhibited significant improvement in IEC, water uptake, conductivity, and permselectivity, while maintaining adequate thermal and mechanical properties of the polymer matrix [152]. The presence of inorganic particle fillers increase the porosity and the pore size of the membrane [40, 150], because a higher particle loading results apparent particle agglomeration, creating larger pores and voids. Such pore formation in the membrane, with the help of additional functional groups (i.e., functionalized nanoparticles) and phase inversion, provides more space with shorter ion channel, which will facilitate enhanced ion migration. Although large pores may weakens the selectivity of the membrane as they can disrupt the functional groups of the polymer matrix, the area resistance of the membrane can be decreased, which is often considered as more critically important in RED [40, 42]. Considering the role of inorganic nanoparticles in forming such free pores when combined with a polymer matrix [58], it is crucial to

understand the effect of particle filler size on the membrane structure and performance in RED applications. The size of inorganic fillers may alter the condition of the membrane structure and pore formation, especially at the polymer-particle interfacial zone [163]. In our previous work, we have developed a series of new nanocomposite IEMs based on sulfonated poly(2,6-dimethyl-1,4-phenylene oxide) (PPO) [37]. PPO carries high film-forming properties, good mechanical, thermal, and chemical stability, and low-moisture uptake [152-155]. For ion exchangeable inorganic materials, silica (SiO_2) has been widely used for the synthesis of composite membranes, mostly for fuel cell and desalination applications [31, 32, 150]. Through suitable surface modification, such inorganic filler material also plays a role as a charge carrier in the composite membrane. The surface of SiO_2 nanoparticle can be modified with $–SO_3H$ group via a sulfonation reaction, which makes the material more hydrophilic and more functional in transporting ionic charges. The studies reported that its versatility due to wide porosities and functionalities allows improved conductivity, water uptake, and mechanical stability of the membranes [161, 164]. In this chapter, we investigate the effect of inorganic particle filler size on the structure and electrochemical performance of silica nanocomposite CEMs for RED power generation. Structural properties of the membranes were tailored by varying nanoparticle loadings and inorganic particle size. The effect of such transformation of interfacial properties in the nanocomposites on physical and electrochemical properties was evaluated and further tested in an RED stack for power production.

6.3. Materials and methods

6.3.1. Materials

Poly (2,6-dimethyl-1,4-phenylene oxide) (PPO) (Aldrich, analytical standard), was used for the polymer membrane. The solvent for PPO was chloroform (Aldrich, anhydrous, 99%). Chlorosulfonic acid (Aldrich, 99%) and sulfuric acid (Aldrich, 98%) were used in sulfonation of the polymer material and the inorganic particle fillers, respectively. Dimethylsulfoxide (DMSO) (ACS grade, 99.9%) was obtained from VWR. Silicon dioxide (SiO_2, silica) nanopowder in two different sizes was used as the inorganic particle fillers: 15 nm SiO_2 (US Research Nanomaterials, 99.5%) and 70 nm (US Research Nanomaterials, 98%). All materials were used as received.

6.3.2. Material preparation

First, the appropriate amount of PPO was added to the chloroform solvent and stirred vigorously to yield a 6 wt% solution at room temperature. Once dissolved, the PPO was sulfonated with an 8 wt% chlorosulfonic acid and chloroform solution. The chlorosulfonic acid-chloroform solution was added dropwise to the PPO-chloroform solution over a time period of 30 minutes with vigorous stirring. During this time, the sulfonated PPO (sPPO) was kept at room temperature as it started to precipitate out of solution. After the sPPO was fully precipitated, it was washed with deionized (DI) water numerous times until the pH was between 5 and 6. The sPPO was then dissolved in methanol over light heating (50 °C) for about an hour. The milky solution was poured into a Pyrex glass tray to form a thin film of about 1 mm thickness. This thin film was allowed to air-dry overnight at room temperature. After 24 hours, the dry sPPO was washed with DI water, left to dry overnight, and then cut into small pieces.

The silica nanopowder was sulfonated with concentrated sulfuric acid (98%). The appropriate amount of SiO_2 was dissolved in 0.25 M H_2SO_4 solution and left soaking for 24 hours. The sulfonated SiO_2 was subsequently filtered and dried at 80 °C in a vacuum oven. Last, to ensure the particles were completely dried, they were calcinated at 500 °C for 3 h to obtain white sulfonated SiO_2 powder.

6.3.3. Synthesis of nanocomposite CEMs

A solvent evaporation method was employed to prepare the nanocomposite cation exchange membranes as described in previous work [37]. 25 wt% solutions of sPPO in DMSO were prepared. When the sPPO was dissolved, 0-1 wt% of sulfonated SiO_2 was mixed with the polymer solution at 60 °C for 24 hours while stirring to properly disperse the particles. The resulting mixture was then cast onto glass plates with a doctor blade to obtain membranes with 30 µm thicknesses. To remove residual solvents, the membranes were dried in a vacuum oven for 24 h at 60 °C then for another 24 hours at 80 °C. The dried membranes were treated in 50 °C warm water for 15 minutes then transferred to a 1 M HCl solution for 24 hours. The final membranes were rinsed with DI water and stored in 0.5 M NaCl solution until testing.

6.3.4. Membrane characterization

FTIR spectroscopy. The chemical structures of silica nanocomposite membranes were investigated using Fourier Transform Infrared (FTIR) Spectra. FTIR spectra of sulfonated SiO_2 and PPO membranes were acquired with FTIR Spectrometer (Spectrum 400,

PerkinElmer), collecting 50 scans per sample at a 4 cm^{-1} resolution and a spectral range of 4000-600 cm^{-1}. The spectrum of ambient air was used as background.

Morphology and structure. The morphology of inorganic particle fillers and structure of the surface and cross section of the prepared membranes were investigated by transmission electron microscopy (TEM, JEOL 100CX II) and scanning electron microscopy (SEM, Zeiss Ultra60 FE-SEM), respectively. For the cross-sectional surface, the samples were prepared in liquid nitrogen and then fractured to obtain a sharp cross-section. Membrane samples were then dried overnight to preserve their structure.

Charge density. IEMs have a fixed number of charged groups in their polymer backbone. This fixed charge density, expressed in units of milliequivalent of fixed groups per gram of water in the membrane (meq g H_2O^{-1}), determines the counter ion transport and ion permselectivity through the membrane. Simplified, the charge density can be determined by dividing the IEC by the SD of the membrane as seen in equation (1):

$$C_{fix} = \frac{IEC}{SD} \quad (1)$$

The IEC and SD of the silica nanocomposite membranes were determined following a previously described procedure [37]. IEC was determined by using a titration method [48]. The samples were first immersed in 1 M HCl for at least 15 hours. Then, the samples were rinsed with DI water to rid them of chloride ions. After rinsing, they were equilibrated in 1 M NaCl solution for at least 6 hours. The resulting solution with displaced hydrogen ions from the membrane was titrated with 0.01 M NaOH solution

using phenolphthalein as an indicator. The IEC of membranes were then calculated by using the following equation:

$$IEC = \frac{C_{NaOH} \times V_{NaOH}}{W_{dry}} \quad (2)$$

where C_{NaOH} is the concentration of NaOH solution, V_{NaOH} is the volume of NaOH solution used and W_{dry} is the dry weight of the membrane.

SD is the extent to which the polymer membrane absorbs moisture. SD is important in determining the mechanical strength and stability of the membrane, as well as being influential in the ability of the membrane to be ion-selective and electrically resistant. It is measured as a percentage of water content per unit weight of dry membrane. To measure SD, a sample was taken from each membrane and immersed in DI water for at least 24 hours. Then, after removing the surface water from the sample, the weight of the swollen membrane was measured. Then, the same sample was air-dried overnight and weighed again to get the dry membrane mass. The SD of a membrane was calculated in weight percent by:

$$SD = \frac{W_{wet} - W_{dry}}{W_{dry}} \times 100\% \quad (3)$$

where W_{wet} and W_{dry} are the weight of the wet and the dry membrane, respectively.

Area resistance. The electrical resistance of the membrane is the ability of the membrane to oppose the passage of electrical current (i.e., low desired). Electrical resistance was measured in a two-compartment cell using 0.5 M NaCl aqueous solutions. The electrodes were made of titanium and coated with Ru-Ir mixed metal oxides (Jing Run Beijing Science and Technology Research Institute Company, China). The resistance of the

membranes was measured at room temperature by impedance spectroscopy (IS) using a Vertex Potentiostat/Galvanostat (Ivium Technologies, The Netherlands) in a frequency range from 10-10^5 Hz with an oscillating voltage of 0.1 V amplitude [45]**.** Then the area resistance was determined by subtraction of the resistance measured without a membrane (blank) from the resistance measured with the membrane under investigation.

Permselectivity. Permselectivity is the ability of the membrane to select for one species over another. The apparent permselectivity of an IEM was determined using a static membrane potential measurement. A two-compartment cell separated by a membrane sample with an effective area of 4.8 cm^2 was used in this experiment. Aqueous solutions of 0.1 M and 0.5 M NaCl were placed in each cell and contact with the test membrane through a small hole in the center of the compartment. Two Ag/AgCl reference electrodes were used to measure the potential difference over the membrane and recorded the potential in a multimeter (Tektronix, USA). The permselectivity is calculated by dividing the measured membrane potential ($\Delta V_{measured}$) by the theoretical membrane potential ($\Delta V_{theoretical}$) as shown below:

$$\alpha(\%) = \frac{\Delta V_{measured}}{\Delta V_{theoretical}} \times 100 \quad (4)$$

where α is the membrane permselectivity (%). Note that the theoretical membrane potential is the membrane potential for an ideal 100% permselective membrane, which is estimated to be 0.0379 V from the Nernst equation [38].

6.3.5. RED power performance

The RED power performance of the synthesized membranes was evaluated in a RED stack. The RED stack contained two titanium mesh end electrodes coated with iridium plasma. It consists of three cell pairs of AEMs (FAS) and CEMs (FKS) (Fumatech, Germany), stacked alternately, and an additional CEM was placed at the end of the stack as a shielding membrane (Figure 6.1). After a measurement was made with the FKS membrane, it was replaced with the synthesized membranes for a comparison. A solution of NaCl (0.25 M) with $K_4Fe(CN)_6$ (0.05 M) and $K_3Fe(CN)_6$ (0.05 M) was used for electrode rinsing and pumped through the electrode compartments at a flow rate of 10.2 cm s^{-1} (300 ml min^{-1}). The stack with membranes also contained woven fabric spacers (thickness: 250 μm, porosity 60%) to form water compartments for the synthetic seawater and river water solutions to pass through. The artificial feed water had a concentration of 0.5 M NaCl for seawater and 0.017 M NaCl for river water. Masterflex peristaltic pumps (Cole-Parmer, USA) delivered the feed solutions for both waters through the RED stack at various flow rates. A four-electrode configuration with an external Vertex Potentiostat (Ivium Technologies, The Netherlands) in galvanostatic mode allowed performance evaluation of the RED stack. The gross power density was estimated from the measured maximum values of voltage (E) and electrical current (*I*), and then corrected by subtraction of the power generated in a blank test with only one CEM in the stack.

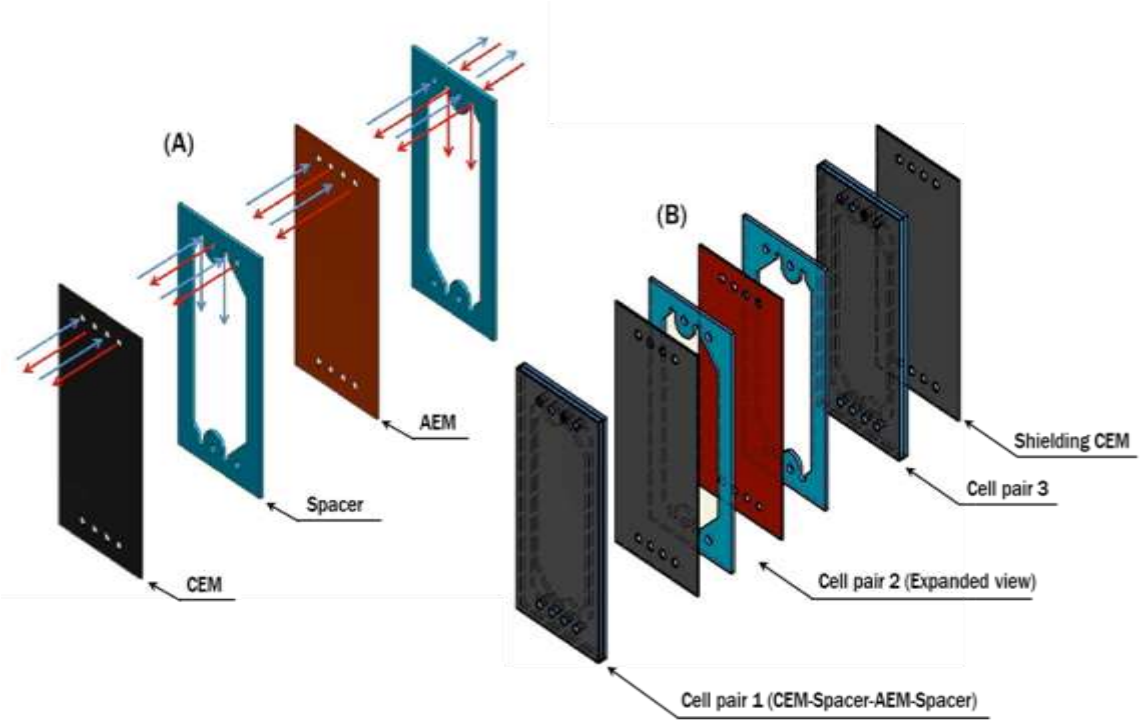

Figure 6.1. Scheme of the membrane configuration in a RED stack used in this performance test: (A) flow schematic for a single RED cell, and (B) Membrane stack consisting of 3 repeating cell pairs. Note that the red and blue arrows in (A) represent two different feed streams (one: saline water, other: fresh water).

6.4. Results and discussion

6.4.1. FTIR spectra study

The FTIR spectra of silica composite membrane films were obtained as seen in Figure 6.2. The spectra of original PPO polymer show C-H stretch of CH_2 and CH_3 throughout 2868 and 2970 cm^{-1} and C-O-C stretch at 942 cm^{-1} in Figure 6.2 a-f. The characteristic absorption peaks at 1060 cm^{-1} are due to the presence of the $–SO_3H$ group that is substituted to PPO aromatic rings after the sulfonation reaction (Figure 6.2 b-f). All the spectra of sPPO membranes show a large band in the range of 3300 and 3500 cm^{-1}, which is attributed to the hydrogen reaction between –OH groups and $–SO_3H$. The symmetric stretching vibration bands for the characteristics of O=Si=O in the SO_3H groups were observed at 1172 cm^{-1} (Figure 6.2 c-g). Overall, these FTIR results demonstrate the successful functionalization of the PPO and SiO_2 nanoparticles with SO_3H groups during the sulfonation process and the presence of ion exchangeable groups in these organic and inorganic components.

6.4.2. Morphology of inorganic particle fillers and membranes

The silica particles of two different sizes (15 and 70 nm) were sulfonated according to a previously reported procedure (Figure 6.3) [109]. The nanoparticles were added to sulfuric acid solution and mixed with the sPPO polymer solution to form nanocomposite membranes via blending method and phase inversion technique. The surface and cross-sectional morphologies of the prepared membranes were observed by scanning electron microscopy (SEM), as seen in Figure 6.4. As inorganic loading increased (~ 1.0 wt%), the higher porosity of the membrane was observed and relatively larger-sized pores were

recognized for those membranes containing bigger particle fillers (70 nm). The increase in pore formation at higher percentage of particle loading is often attributed to the particle agglomeration that leads to larger pores and additional porosity in the matrix. The pore formation at interfacial zone of polymer and filler can also be dependent on inorganic filler sizes [35]. The smaller inorganic fillers are more likely to have better interaction between particles and polymer, which results in less interfacial gap (i.e., small pore size). On the other hand, relatively larger pore sizes and voids for the membranes with the bigger particle fillers can arise because of poor interactions between particles and polymer (i.e., larger interfacial gaps or pores) compared to those membranes with smaller sized particle fillers (15 nm). The energy-dispersive X-ray spectroscopy (EDS) mapping technique was utilized to elucidate the distribution and aggregation of particle fillers in the membranes. Figure 6.5 shows Si mapping of sPPO nanocomposite. In the figure, the particle fillers are well-dispersed throughout the polymer matrix with some signs of particle agglomeration, which is a possible cause of apparent pores formed in the structure.

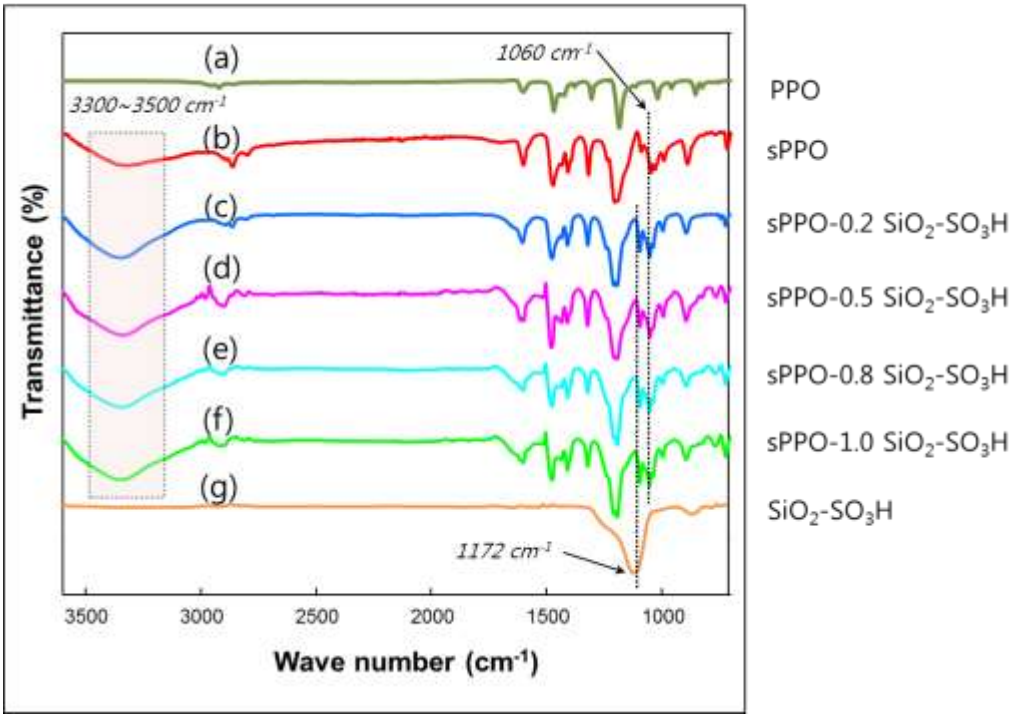

Figure 6.2. FTIR spectra of nanocomposite membranes: (A) Pristine (PPO), (B) Sulfonated PPO (sPPO), (C) 0.2 wt% SiO_2-SO_3H, (D) 0.5 wt% SiO_2-SO_3H, (E) 0.8 wt% SiO_2-SO_3H, (F) 1.0 wt% SiO_2-SO_3H, (G) SiO_2-SO_3H.

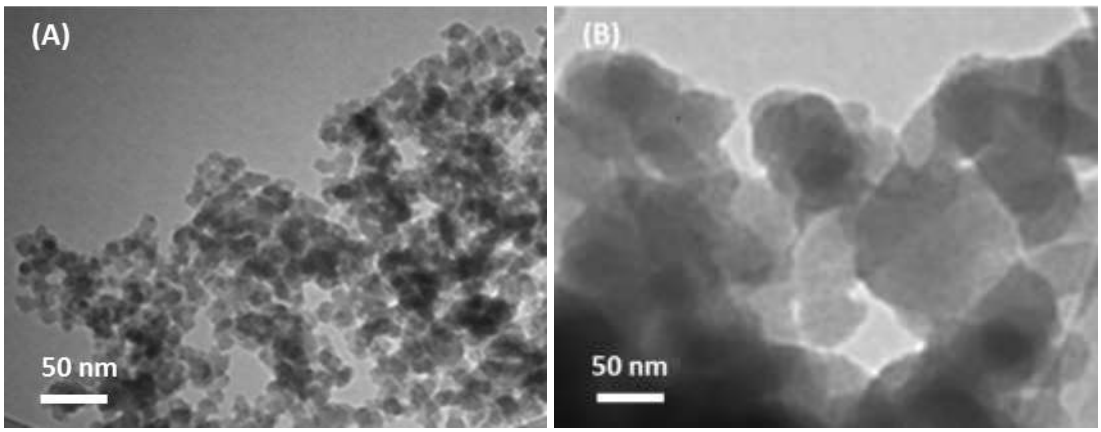

Figure 6.3. TEM images of sulfonated SiO_2 nanoparticles with sizes of (A) 15 nm and (B) 70 nm.

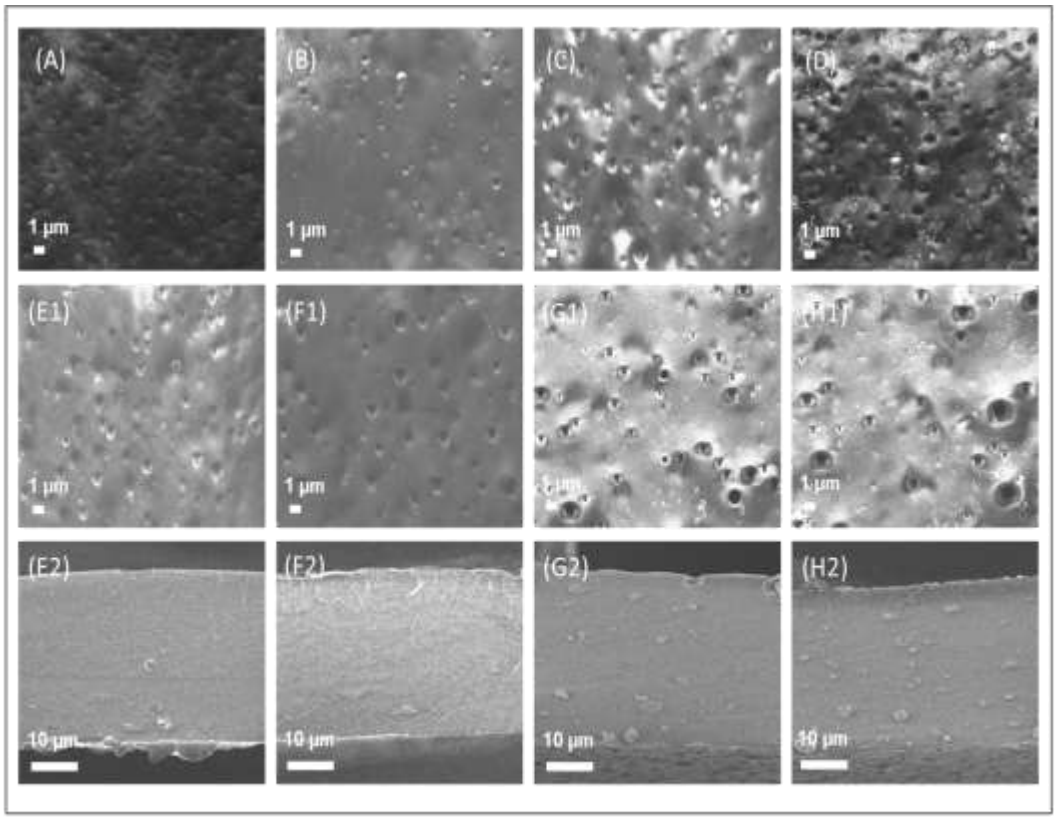

Figure 6.4. SEM micrographs of sPPO composite membranes: (A) 0.2 wt% SiO_2-SO_3H (15 nm), (B) 0.5 wt% SiO_2-SO_3H (15 nm), (C) 0.8 wt% SiO_2-SO_3H (15 nm), (D) 1.0 wt% SiO_2-SO_3H (15 nm), (E1-H1) 0.2, 0.5, 0.8, and 1.0 wt% SiO_2-SO_3H (70 nm), respectively, and (E2-H2) cross-section surfaces of 0.2, 0.5, 0.8, and 1.0 wt% SiO_2-SO_3H (70 nm), respectively.

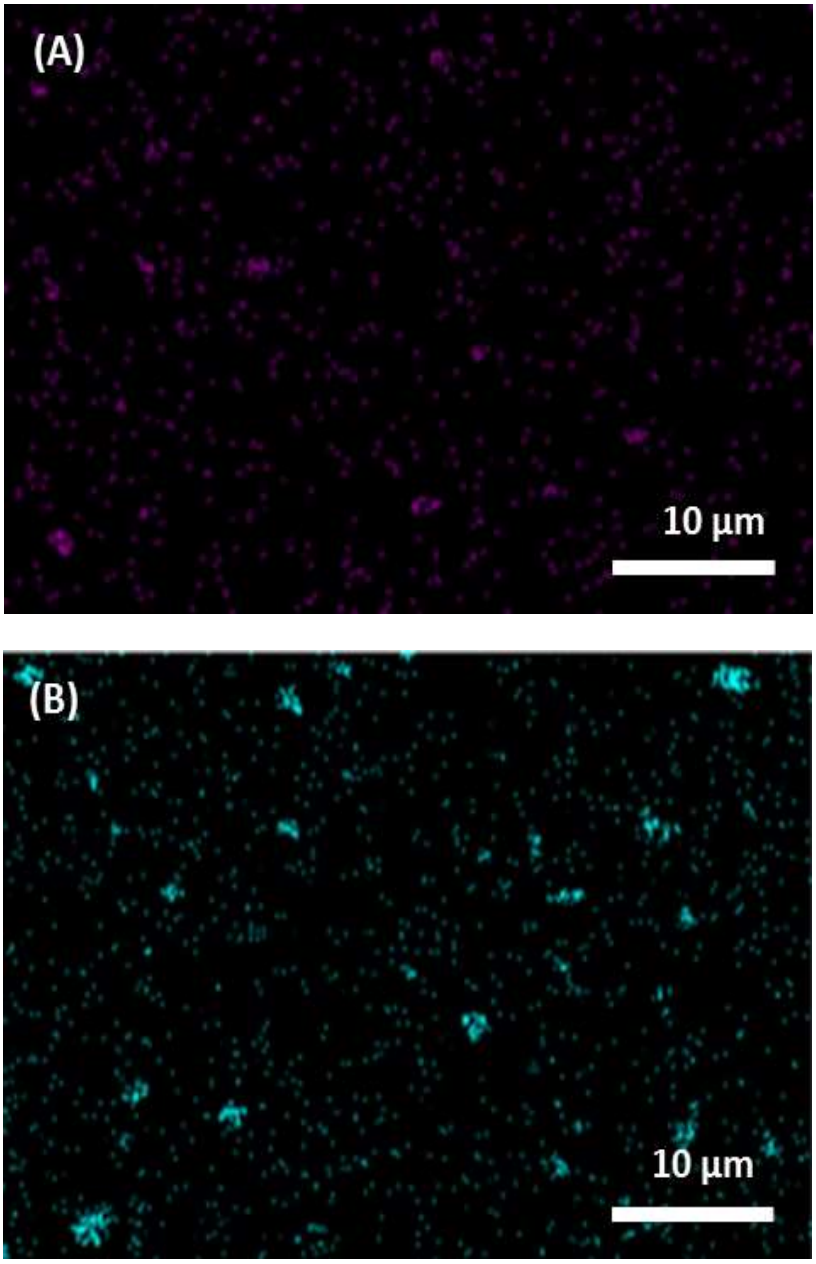

Figure 6.5. EDS-mapping analysis of sPPO composite membranes: (A) 0.5 wt% SiO_2-SO_3H (70 nm), and (B) 1.0 wt% SiO_2-SO_3H (70 nm). Note that pink and cyan dots represent the dispersion of silica nanoparticles on the surface of corresponding membranes.

6.4.3. Physicochemical properties of membranes

SD is typically proportional to IEC and inversely proportional to cross-linkage [165]. As IEC increases, membrane swelling generally increases but other factors, such as ion exchange group species and polymer material, can cause SD to fluctuate. Higher SD can be indicative of low mechanical strength and stability of the membrane. From the data (Figure 6.6(A)), there is a trend of increasing SD with increasing silica nanoparticle size. This can be explained from a microscopic level. As seen in Figure 6.4, bigger nanoparticles allow for larger pores within the membrane. This increase in pore size allows more water molecule to be absorbed by the membrane. On the other hand, the smaller nanoparticles with relatively small pores, are less able to take up water molecules, leading to a lower SD.

IEC is an important characteristic of ion exchange membranes for RED since it affects most of the other properties of the membrane. For both sizes of silica nanoparticles, the trend found from analysis of our IEC results shows an increase until a peak at 0.5 wt% loading. After this peak, the IEC dramatically decreases when 0.8 wt% silica loading is applied then gradually decreases at 1.0 wt%. This can be explained by the fact that an increase in loading of sulfonated silica (0.2-0.5 wt%) increases the functionalized groups within the membrane and allows for optimized exchange of ions. However, further increase of the silica concentration (> 0.8 wt%) can cause agglomeration of the nanoparticles, decreasing the ability of the membrane to productively exchange ions.

Central to this study is the effect of nanoparticle size on membrane performance. The nanocomposite membranes containing the bigger nanoparticles (70 nm) consistently

performed better in IEC tests than those with the smaller nanoparticles. The difference is most apparent for the 0.5 wt% membrane, which could indicate that the loading is interconnected when considering nanoparticle size in relation to ability to exchange ionic species. The nanoparticle size is significant because as the size of the nanoparticle increases, the surface of ion accessible functionalized groups at interfacial (polymer and filler) zone increases (Figure 6.7), and, therefore, an increased ability to exchange ions. The bigger particles with lower degree of agglomeration create larger interface void region (i.e., poor polymer-filler interaction) at interfacial zone of polymer and filler. Thus, the bigger particle based interfacial zone with high accessible surface area and open pore structures provides highly porous channels for easy access of ions. For this reason, the 70 nm-containing membranes exhibited better IEC in all loading percentages. But, there is a limit to this beneficial feature; as shown in Figure 6.6(B), there is a loss of accessible ion exchange groups at higher loading (0.8 ~ 1.0 wt%). The loss of accessible ion exchange groups at high loading is related to a reduction of the surface area of charged groups. This reduction of the surface area of charged groups is largely due to particle agglomeration and indicates poor interaction between the sulfonated silica nanoparticles and the polymer. On the other hand, at low silica loading (0.2 and 0.5 wt%), there might be relatively better interaction between the particle fillers and the polymer, showing higher degree of IEC.

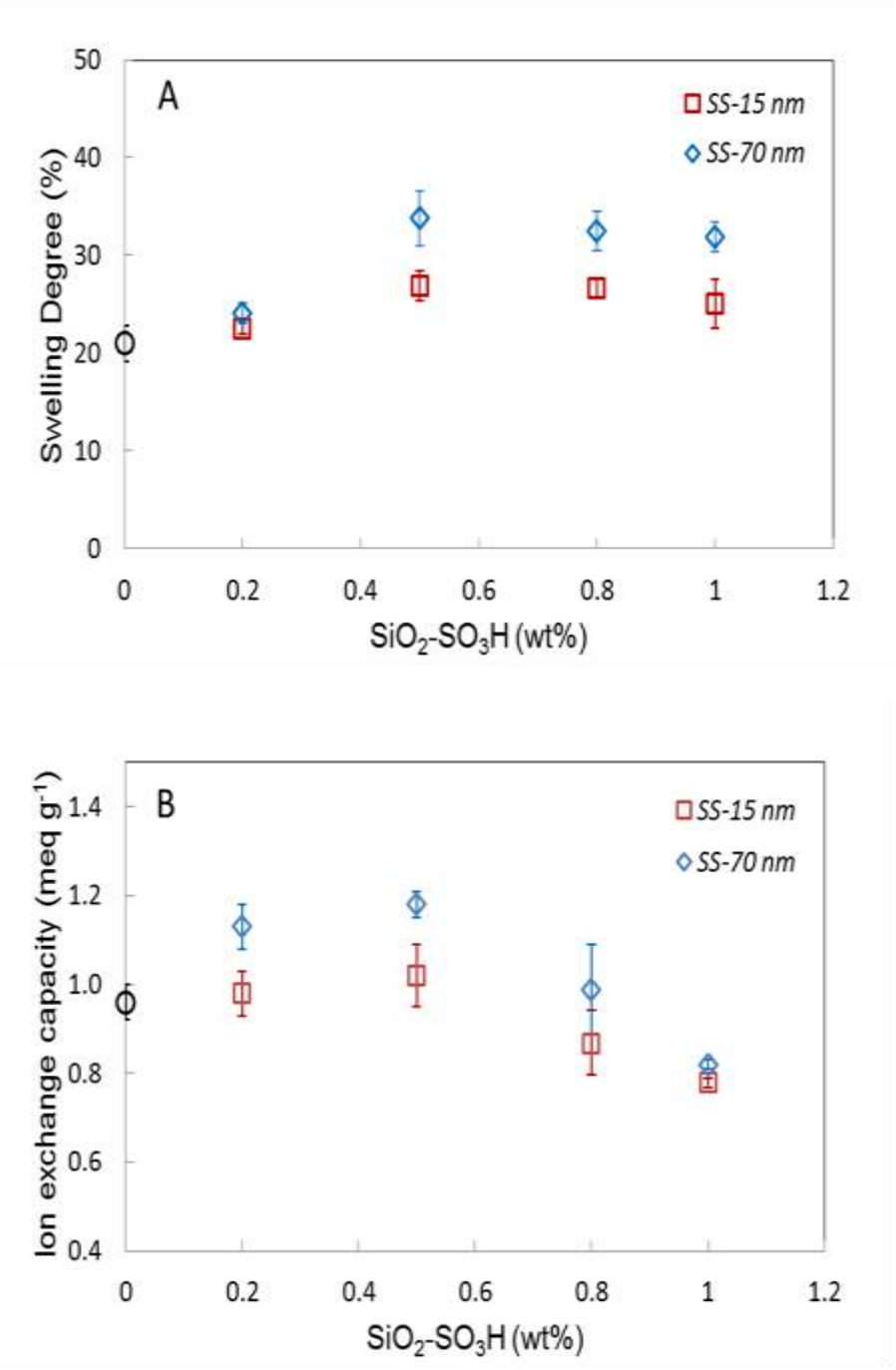

Figure 6.6. Swelling degree (A) and ion exchange capacity (B) of sPPO nanocomposite membranes of different size of inorganic particle fillers at various loading amount. Note that *SS* denotes the sulfonated SiO_2.

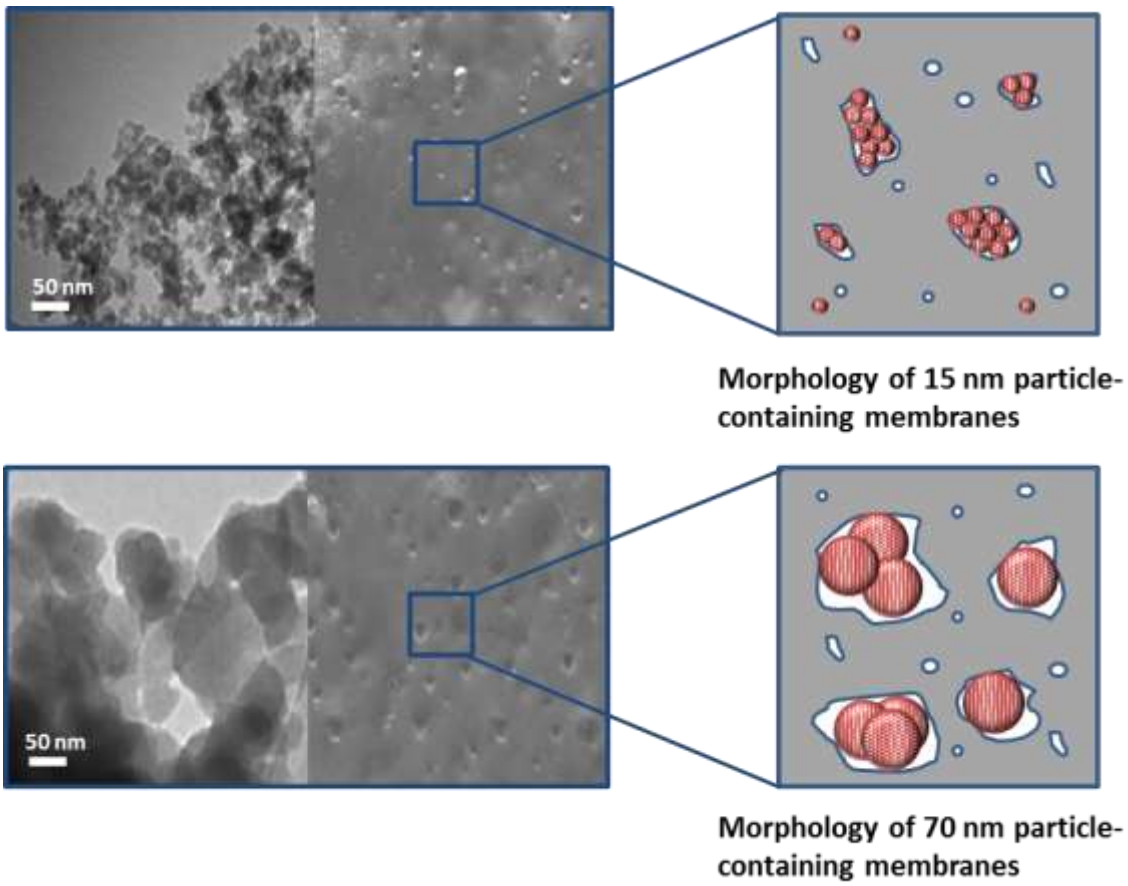

Figure 6.7. Effect of inorganic filler size on membrane morphology.

6.4.4. Electrochemical behavior of membranes

In general, membrane permselectivity and area resistance are dependent upon the degree of IEC and SD of the membranes. Considering the fact that the fixed charge density is determined by the IEC over SD (Eq. 1), permselectivity and area resistance are often related to the fixed charge density. The charge density is an important electrochemical property, which indicates the number of charged functional groups (counter ions) in the membrane. Thus, stronger co-ion exclusion is expected with high charge density. In Figure 6.8, we present the permselectivity and area resistance of the prepared membranes as a function of charge density derived from IEC and SD. The prepared membranes exhibited a slightly increasing trend of permselectivity up to certain degree of CD (i.e., 3.8 meq. g^{-1}). This tendency is the result of effective co-ion exclusion, which facilitates the enhanced counter ion transport, leading to higher permselectivity. A more apparent correlation between charge density and area resistance was observed for the prepared nanocomposite membranes (Figure 6.8). This is often the case for the membranes with same structure and chemistry as well as a comparable degree of cross-linking [40, 42].

The permselectivity of the prepared nanocomposite membranes increased with increasing the inorganic filler loading and peaked at low percentage of sulfonated silica particles, i.e., 0.5 wt% (Figure 6.9A). The lower permselectivity when more sulfonated silica was applied is possibly due to loss of the accessible functional groups in sulfonated silica, which causes low IEC and fixed charge density, resulting in poor selective ion transport of counter ions (Table 6.1). In general, more swelling occurs with more ionic groups present in the matrix, therefore low resistance is normally expected [25, 37]. 0.5 wt%

SiO_2-SO_3H with the highest IEC and SD showed the lowest resistance. As seen in Figure 6.9, nanoparticle size influenced notably on the degree of permselectivity and resistance. The effect of particle size on such ion transport properties may be associated with the structure and pore formation of the membranes, which often depends on the interaction between polymer and particle [35]. As we discussed in previous section, nanoparticle size plays a contrasting role in forming membrane pores or free volume. The resultant larger pores or higher porosity of the membranes containing bigger particle filler (70 nm) lowers the ability to effectively select counter ionic species, leading to lower permselectivity compared to that of membranes with smaller particle filler. On the other hand, the formation of such pore structure with the bigger particle fillers also promotes enhanced migration of ionic species, which, in turn, resulted in relatively lower resistance at all filler loadings (Figure 6.9B). In addition, the membranes with low area resistance often have weaker selectivity due to loosened mechanical structure. However, in this work, 0.5 wt% SiO_2-SO_3H (70 nm) with the highest IEC, SD, and permselectivity exhibited the lowest level of resistance. This phenomenon can be the case that the presence of inorganic particle filler in the membrane structure may lead to sustain its mechanical strength, which results in good permselectivity. The resistance increased as more SiO_2-SO_3H (both particle size, > 0.5 wt%) was incorporated. The increase in the resistance can be explained by the relatively low charge density of those membranes at higher percentage of inorganic filler loading (0.8 and 1.0 wt%).

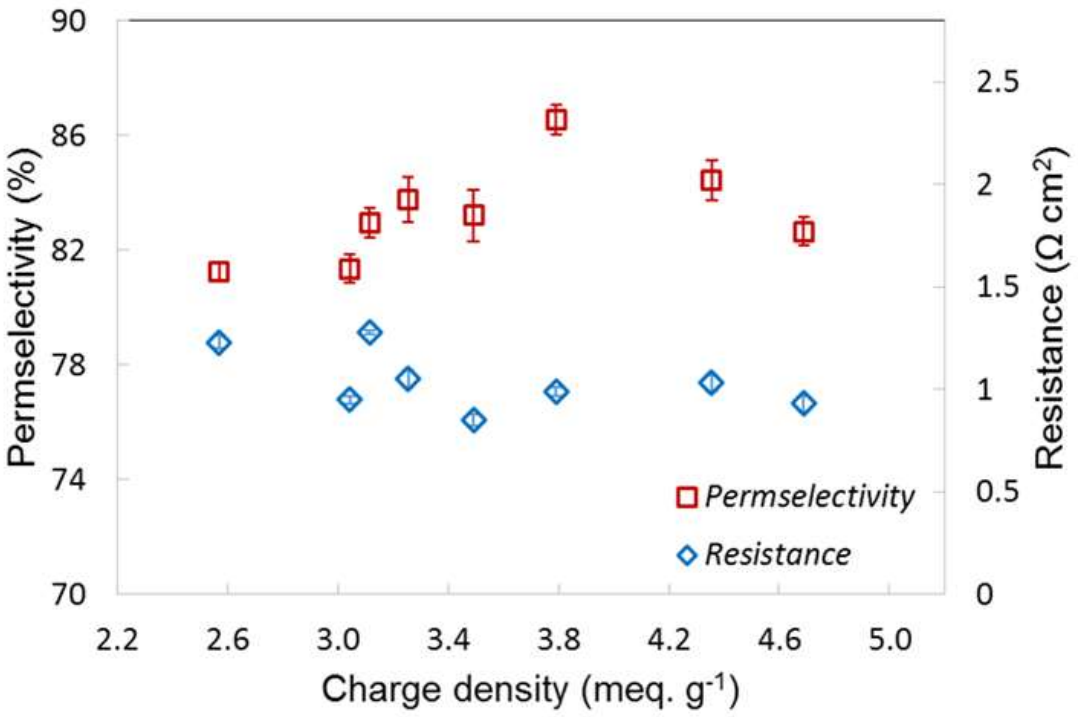

Figure 6.8. Membrane permselectivity (A) and area resistance (B) as a function of charge density.

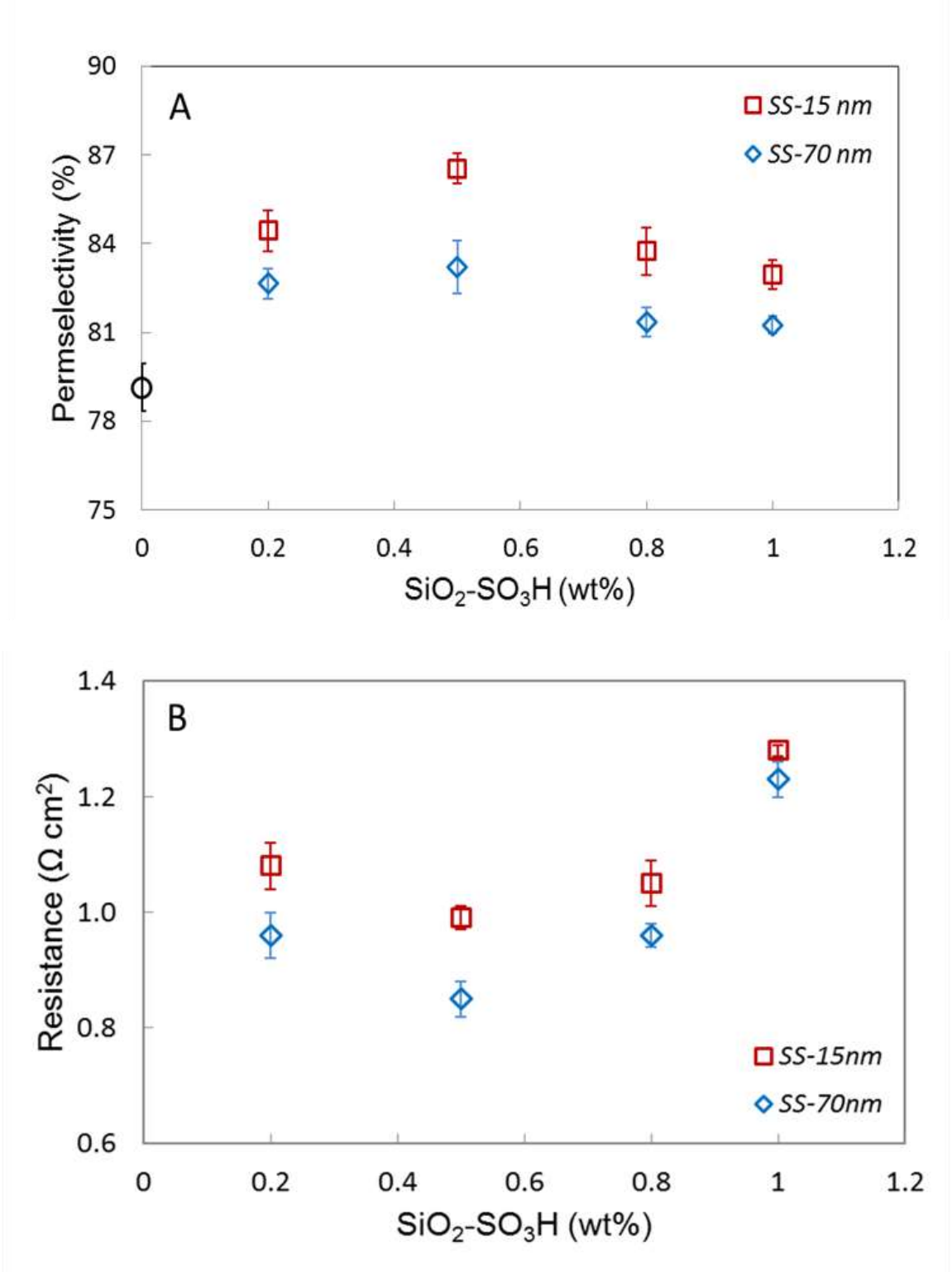

Figure 6.9. Membrane permselectivity (A) and area resistance (B) of the membranes of different size of inorganic particle fillers at various loading amount. Note that *SS* denotes the sulfonated SiO_2 and the resistance data for the pristine membrane (0 wt% SiO_2-SO_3H) lied on outside the axis scale range.

6.4.5. Power density in RED

We compared the gross power density of the CEMs each containing different size nanoparticles at different inorganic loadings with that of a commercial membrane (Fumatech FKS). The Fumatech FAS membrane was used as the reference anion exchange membrane in the RED stack for each test. Figure 6.10 shows the gross power density of the stack with the prepared nanocomposite membranes as a function of the feed flow velocity. As flow velocity increases with rapidly renewed feed waters, more ion transport can be facilitated because of the reduced boundary layer resistance at the membrane surface. Thus, higher gross power density is achieved at resulting low internal electrical resistance with increasing flow velocities. The membrane with a blend ratio of 0.5 wt% SiO_2-SO_3H with a particle size of 70 nm exhibited the highest power density of 1.3 W m^{-2} at the highest feed flow velocity, which is significantly higher than that of the membrane containing smaller nanoparticle (15 nm) (Figure 6.10). In our experiments, higher power densities were observed with those membranes containing the bigger particle filler. This is in agreement with Figure 6.9B that shows relatively lower area resistance with the 70 nm-containing membranes than with the other membranes containing smaller nanoparticles. Although the theoretical power density is proportional to the square of permselectivity (i.e., Power ~ α^2) in RED, the membranes having higher permselectivity do not always perform better [42]. In this work, we also found that the membranes with the 15 nm particle fillers exhibited a higher degree of permselectivity, but their gross power density did not appear to be affected throughout the various inorganic loadings, which is consistent with the literature [42]. Similarly, the commercial FKS membrane showed relatively lower gross power density compared to those

membranes with relatively lower permselectivity as well as lower area resistance. Therefore, in this work, regardless of high selectivity, the area resistance of these prepared membranes dominates and has a significant impact on the overall RED power generation. Overall, the size of inorganic particle fillers affected the power performance of prepared nanocomposite CEMs, showing about a 10% difference (average) at various loading concentrations. The inorganic filler nanoparticle size influences the membrane structure and its electrochemical characteristics (e.g., area resistance), and as such may also be a key driver to achieve high power density in RED stack.

Table 6.1. Physical and electrochemical properties of the prepared membranes.

Membranes	IEC [meq. g dry^{-1}]	SD [%]	CD [meq. g H_2O^{-1}]	Permselectivity [%]	Resistance [Ω cm^2]
0 SS	0.96	21	4.6	79.1	1.87
0.2 SS-15 nm	0.98	23	4.4	84.4	1.03
0.5 SS-15 nm	1.02	27	3.8	86.5	0.99
0.8 SS-15 nm	0.87	27	3.3	83.8	1.05
1.0 SS-15 nm	0.78	25	3.1	83.0	1.28
0.2 SS-70 nm	1.13	24	4.7	82.7	0.93
0.5 SS-70 nm	1.18	34	3.5	83.2	0.85
0.8 SS-70 nm	0.99	33	3.0	81.4	0.95
1.0 SS-70 nm	0.82	32	2.6	81.3	1.23
FKS[a]	1.49	15	9.9	94.0	1.49

IEC: ion exchange capacity; SD: swelling degree; CD: charge density; SS: sulfonated SiO_2.

[a] FKS is a commercial CEM from Fumatech, Germany with a thickness of 30 μm.

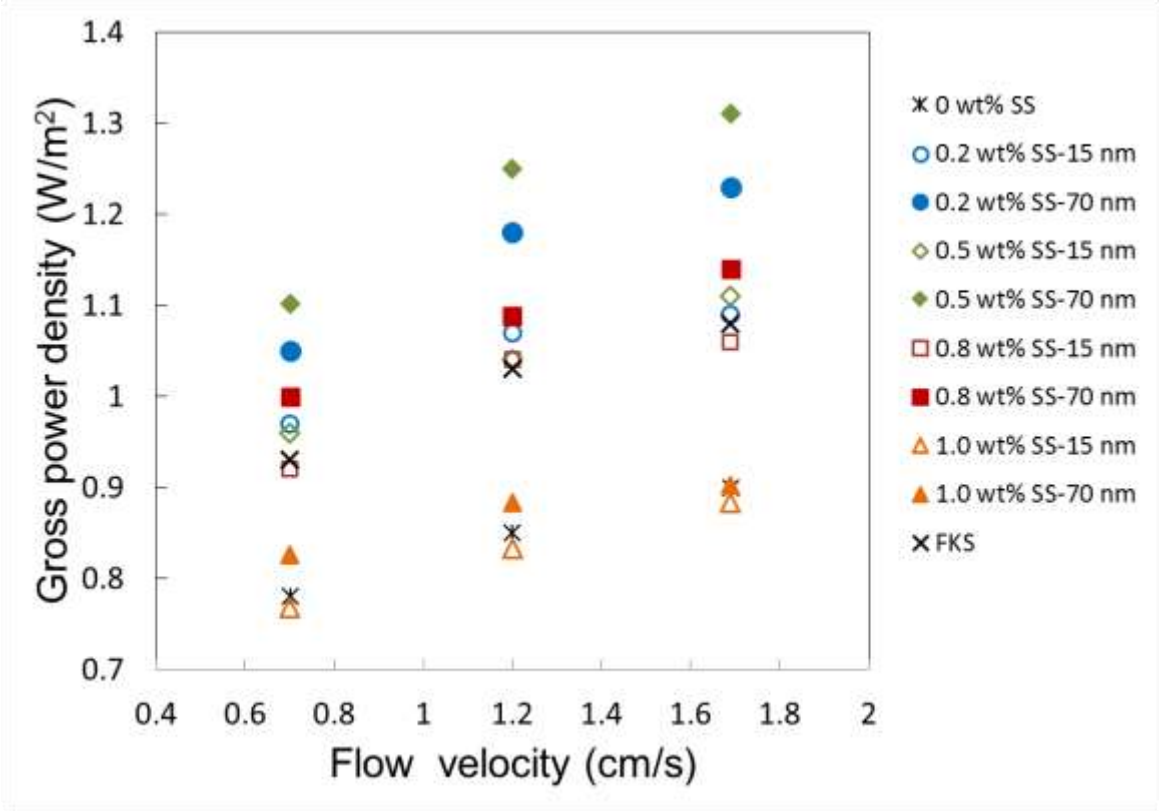

Figure 6.10. Gross power density as a function of flow velocity for the prepared nanocomposite membranes. The performance of the FKS membrane is shown for comparison.

6.5. Conclusion

In this chapter, silica nanocomposite cation exchange membranes were prepared with various nanoparticle loadings at two different inorganic particle sizes by blending, casting, and a solvent evaporation technique. The evaluation of physical and electrochemical properties was discussed. The effect of inorganic particle filler size on silica nanocomposite cation exchange membranes at various nanoparticle loadings on the performance of a reverse electrodialysis (RED) stack was also investigated. Relatively higher IEC and lower area resistance were achieved with the membranes containing the bigger particle filler size (70 nm). The permselectivity, on the other hand, performed better with the 15 nm particle-containing membranes in all loading percentages. This is possibly attributed to the larger-sized pores of the 70nm-containing membranes with low polymer-particle adhesion at their interfacial zone, which allows enhanced ability of ion exchange and transport, but weakens effective co-ionic exclusion. Overall, the most favorable physical and electrochemical characteristics were exhibited at 0.5 wt% SiO_2-SO_3H. The area resistance of the membranes containing the bigger particle filler was around 9.3% lower than those with smaller particle filler, which resulted in a 10% (average) higher gross power density at all loading concentrations. Considering these results, nanocomposite IEMs with further-optimized inorganic filler properties and loadings may enable even greater RED power generation.

CHAPTER 7

MAJOR CONCLUSIONS AND FUTURE WORK

7.1. Major conclusions

The key findings and conclusions of this dissertation are briefly summarized below:

(i) The stack OCV of the RED system was sensitive to flow rate variation in the presence of multivalent ions. The power density obtained with multivalent ions was fairly lower than that when using a monovalent ion (i.e., NaCl) due to higher internal cell resistance. Higher power density was gained by applying higher flow rates in the saline water compartment than in the freshwater compartment. Moreover, RED performance was significantly improved by using a saline water compartment thicker than the freshwater compartment.

(ii) The novel nanocomposite CEMs were designed specifically for RED by incorporation of sulfonated Fe_2O_3 in sPPO polymer matrix. By controlling the inorganic filler amount (i.e., Fe_2O_3-SO_4^{2-}), the nanocomposite membrane was found to be optimized at certain inorganic loadings for RED performance, which enables to generate higher power output than the commercially available CSO membrane. This newly-developed nanocomposite membrane showed the potential to be a feasible candidate for use as ion-exchange membranes in RED power generation.

(iii) A two-step phase inversion membrane preparation process yielded the desired membrane structure and porosity in the presence of inorganic nanoparticles. Porous nanocomposite membranes were prepared with various thicknesses and evaporation times. The IEC, SD, and permselectivity of the membranes were comparable for

various film thicknesses. Short evaporation time led to a structure with markedly large pores but clearly weakened ion transport and selectivity. The membrane's thickness directly affected the area resistance and thus its performance in a RED stack. Relatively lower area resistance was achieved with thinner porous membranes, which had the highest gross power density in a RED stack. Tailoring key structural properties of the membrane play a significant role in ionic transport, resulting in higher RED power performance.

(iv) Silica nanocomposite CEMs were prepared with various nanoparticle loadings at two different inorganic particle sizes by blending, casting, and a solvent evaporation technique. Relatively higher IEC and lower area resistance were achieved with the membranes containing the bigger particle filler size. The permselectivity, on the other hand, performed better with the small-sized particle-containing membranes in all loading percentages. This is attributed to the larger-sized pores of the bigger particle-containing membranes with low polymer-particle adhesion at their interfacial zone, which allows enhanced ability of ion exchange and transport, but weakens effective co-ionic exclusion. The area resistance of the membranes containing the bigger particle filler was lower than those with smaller particle filler, which resulted in higher gross power density at all loading concentrations.

7.2. Future work

Based on the current knowledge and challenges, future work to advance the development of salinity gradient power production using RED process may include the following crucial issues:

(i) Development of predictive models for the key performance-determining properties in RED system. Detailed investigation needs to be aimed at maximizing the power output and efficiency with a particular focus on system constraints and key performance-determining factors such as operating flow pressures, membrane resistance, membrane sizes, and stack design/configuration. The optimization of such components within the RED system can be achieved with the aid of more elaborate mathematical models especially for the large-scale application of real water streams in RED.

(ii) Development of lab-to-scale-up RED membrane modules. Based on the assessment of the model, the fabrication of sophisticated module-scale design and implementation in real sea and river water should be demonstrated with the purpose of stepping up the technology for proper access to commercialization.

(iii) Identify the low-cost IEM materials. The importance of membrane development and optimization for the RED application using cost-competitive materials has been stressed in many studies. A successful launch of large-scale energy conversion by RED depends on effective and inexpensive membranes that uses low-cost and well-developed IEM materials.

(iv) Investigate the innovative membrane preparation methods. In RED application, better quality membrane products ensure better performance, which often can be achieved by improving the physicochemical structure and electrochemical characteristics of the membranes. Specifically, following methods should be based and further explored: 1) copolymerization, 2) use of a crosslinking agent, 3) formation of a hybrid structure (organic-inorganic), 4) controlling the degree of

chemical reactions (e.g., sulfonation and amination), and 5) tailoring the ratio of the polymeric binder or the inorganic filler loading. In addition, effective design of RED membranes should also be focusing on a reduction in fouling and improvements to the fouling resistance by using polymer-grafting techniques to tailor the membrane surface with enhanced anti-biofouling properties for advanced application in natural waters.

(v) Investigate the synergistic impact by combining RED with other technologies. There is even greater potential available once RED is combined with other existing processes such as wastewater treatment, desalination (electrodialysis), microbial fuel cell. Such hybrid technology could be highly efficient and a promising way to conquer the limitations of individual systems. However, combinant technologies are in an early stage of development and practical application of these approaches could be more feasible only with greater development in membranes and system optimization.

REFERENCES

1. Ramon, G. Z.; Feinberg, B. J.; Hoek, E. M. V., Membrane-based production of salinity-gradient power. *Energy & Environmental Science* **2011,** *4*, 4423.
2. Logan, B. E.; Elimelech, M., Membrane-based processes for sustainable power generation using water. *Nature* **2012,** *488*, (7411), 313-319.
3. Pattle, R., Production of electric power by mixing fresh and salt water in the hydroelectric pile. *Nature* **1954,** *174*, 660.
4. Weinstein, J. N.; Leitz, F. B., Electric power from differences in salinity: the dialytic battery. *Science* **1976,** *191*, (4227), 557.
5. Wick, G. L.; Schmitt, W. R., Prospects for Renewable Energy from Sea. *Mar Technol Soc J* **1977,** *11*, (5-6), 16-21.
6. Schnoor, J. L., Salt: The Final Frontier. *Environmental science & technology* **2013**.
7. Post, J. W.; Veerman, J.; Hamelers, H. V. M.; Euverink, G. J. W.; Metz, S. J.; Nymeijer, K.; Buisman, C. J. N., Salinity-gradient power: Evaluation of pressure-retarded osmosis and reverse electrodialysis. *J Membrane Sci* **2007,** *288*, (1-2), 218-230.
8. Dlugolecki, P.; Gambier, A.; Nijmeijer, K.; Wessling, M., Practical potential of reverse electrodialysis as process for sustainable energy generation. *Environmental science & technology* **2009,** *43*, (17), 6888-6894.
9. Post, J. W.; Hamelers, H. V. M.; Buisman, C. J. N., Energy recovery from controlled mixing salt and fresh water with a reverse electrodialysis system. *Environmental science & technology* **2008,** *42*, (15), 5785-5790.
10. Veerman, J.; Saakes, M.; Metz, S. J.; Harmsen, G. J., Electrical Power from Sea and River Water by Reverse Electrodialysis: A First Step from the Laboratory to a Real Power Plant. *Environmental science & technology* **2010,** *44*, 9207-9212.
11. Shaposhnik, V.; Kesore, K., An early history of electrodialysis with permselective membranes. *J Membrane Sci* **1997,** *136*, (1), 35-39.
12. Lacey, R. E., Energy by reverse electrodialysys. *Ocean engineering* **1980,** *7*, (1), 1-47.
13. Jagur-Grodzinski, J.; Kramer, R., Novel process for direct conversion of free energy of mixing into electric power. *Industrial & Engineering Chemistry Process Design and Development* **1986,** *25*, (2), 443-449.
14. Turek, M.; Bandura, B., Renewable energy by reverse electrodialysis. *Desalination* **2007,** *205*, (1), 67-74.
15. Daniilidis, A.; Herber, R.; Vermaas, D. A., Upscale potential and financial feasibility of a reverse electrodialysis power plant. *Applied Energy* **2014,** *119*, 257-265.
16. Elimelech, M.; Phillip, W. A., The future of seawater desalination: energy, technology, and the environment. *Science* **2011,** *333*, (6043), 712-717.
17. Veerman, J.; Saakes, M.; Metz, S.; Harmsen, G., Reverse electrodialysis: evaluation of suitable electrode systems. *Journal of Applied Electrochemistry* **2010,** *40*, (8), 1461-1474.

18. Veerman, J.; Post, J.; Saakes, M.; Metz, S.; Harmsen, G., Reducing power losses caused by ionic shortcut currents in reverse electrodialysis stacks by a validated model. *J Membrane Sci* **2008,** *310*, (1-2), 418-430.
19. Veerman, J.; Saakes, M.; Metz, S.; Harmsen, G., Reverse electrodialysis: A validated process model for design and optimization. *Chemical Engineering Journal* **2011,** *166*, (1), 256-268.
20. Veerman, J.; Saakes, M.; Metz, S.; Harmsen, G., Reverse electrodialysis: Performance of a stack with 50 cells on the mixing of sea and river water. *J Membrane Sci* **2009,** *327*, (1-2), 136-144.
21. Veerman, J.; De Jong, R.; Saakes, M.; Metz, S.; Harmsen, G., Reverse electrodialysis: Comparison of six commercial membrane pairs on the thermodynamic efficiency and power density. *J Membrane Sci* **2009,** *343*, (1-2), 7-15.
22. Dlugolecki, P.; Dabrowska, J.; Nijmeijer, K.; Wessling, M., Ion conductive spacers for increased power generation in reverse electrodialysis. *J Membrane Sci* **2010,** *347*, (1-2), 101-107.
23. Sales, B.; Saakes, M.; Post, J.; Buisman, C.; Biesheuvel, P.; Hamelers, H., Direct Power Production from a Water Salinity Difference in a Membrane-Modified Supercapacitor Flow Cell. *Environmental science & technology* **2010,** *44*, 5661-5665.
24. Vermaas, D. A.; Saakes, M.; Nijmeijer, K., Doubled power density from salinity gradients at reduced inter-membrane distance. *Environmental science & technology* **2011,** *45*, 7089-7095.
25. Dlugolecki, P.; Nymeijer, K.; Metz, S.; Wessling, M., Current status of ion exchange membranes for power generation from salinity gradients. *J Membrane Sci* **2008,** *319*, (1-2), 214-222.
26. Audinos, R., Electric-power produced from 2 solutions of unequal salinity by reverse electrodialysis. *Indian Journal of Chemistry Section a-Inorganic Bio-Inorganic Physical Theoretical & Analytical Chemistry* **1992,** *31*, (6), 348-354.
27. Post, J. W.; Hamelers, H. V. M.; Buisman, C. J. N., Influence of multivalent ions on power production from mixing salt and fresh water with a reverse electrodialysis system. *J Membrane Sci* **2009,** *330*, (1-2), 65-72.
28. Minagawa, M.; Tanioka, A.; Ramirez, P.; Mafe, S., Amino acid transport through cation exchange membranes: Effects of pH on interfacial transport. *Journal of Colloid and Interface Science* **1997,** *188*, (1), 176-182.
29. Shahi, V. K.; Thampy, S. K.; Rangarajan, R., Chronopotentiometric studies on dialytic properties of glycine across ion-exchange membranes. *J Membrane Sci* **2002,** *203*, (1-2), 43-51.
30. Choi, J. H.; Kim, S. H.; Moon, S. H., Recovery of lactic acid from sodium lactate by ion substitution using ion-exchange membrane. *Separation and Purification Technology* **2002,** *28*, (1), 69-79.
31. Lee, C. H.; Min, K. A.; Park, H. B.; Hong, Y. T.; Jung, B. O.; Lee, Y. M., Sulfonated poly(arylene ether sulfone)-silica nanocomposite membrane for direct methanol fuel cell (DMFC). *J Membrane Sci* **2007,** *303*, (1-2), 258-266.
32. Su, Y. H.; Liu, Y. L.; Sun, Y. M.; Lai, J. Y.; Wang, D. M.; Gao, Y.; Liu, B. J.; Guiver, M. D., Proton exchange membranes modified with sulfonated silica nanoparticles for direct methanol fuel cells. *J Membrane Sci* **2007,** *296*, (1-2), 21-28.

33. Seo, D. W.; Lim, Y. D.; Lee, S. H.; Islam, M. M.; Jin, H. M.; Lee, K. H.; Jang, H. H.; Kim, W. G., Nano Composite membranes of Sulfonated Amine-Poly(ether sulfone)s and SiO(2) for Fuel Cell Application. In *Eco-Materials Processing and Design Xi*, Kim, H. S.; Yang, J. F.; Sekino, T.; Anpo, M.; Lee, S. W., Eds. 2007; Vol. 658, pp 392-395.
34. Klaysom, C.; Marschall, R.; Wang, L. Z.; Ladewig, B. P.; Lu, G. Q. M., Synthesis of composite ion-exchange membranes and their electrochemical properties for desalination applications. *Journal of Materials Chemistry* **2010,** *20*, (22), 4669-4674.
35. Klaysom, C.; Moon, S. H.; Ladewig, B. P.; Lu, G. Q. M.; Wang, L. Z., The Influence of Inorganic Filler Particle Size on Composite Ion-Exchange Membranes for Desalination. *Journal of Physical Chemistry C* **2011,** *115*, (31), 15124-15132.
36. Scialdone, O.; Guarisco, C.; Grispo, S.; D' Angelo, A.; Galia, A., Investigation of electrode material - Redox couple systems for reverse electrodialysis processes. Part I: Iron redox couples. *Journal of Electroanalytical Chemistry* **2012,** *681*, 66-75.
37. Hong, J. G.; Chen, Y., Nanocomposite reverse electrodialysis (RED) ion-exchange membranes for salinity gradient power generation. *J Membrane Sci* **2014,** *460*, 139-147.
38. Guler, E.; Zhang, Y. L.; Saakes, M.; Nijmeijer, K., Tailor-Made Anion-Exchange Membranes for Salinity Gradient Power Generation Using Reverse Electrodialysis. *Chemsuschem* **2012,** *5*, (11), 2262-2270.
39. Guler, E.; Elizen, R.; Saakes, M.; Nijmeijer, K., Micro-structured membranes for electricity generation by reverse electrodialysis. *J Membrane Sci* **2014,** *458*, (0), 136-148.
40. Hong, J. G.; Chen, Y., Evaluation of electrochemical properties and reverse electrodialysis performance for porous cation exchange membranes with sulfate-functionalized iron oxide. *J Membrane Sci* **2015,** *473*, (0), 210-217.
41. Forgacs, C., Generation of electricity by reverse electrodialysis. *R&D Authority, Ben Gurion University, Beer Sheva, Israel* **1978**.
42. Guler, E.; Elizen, R.; Vermaas, D.; Saakes, M.; Nijmeijer, K., Performance-determining membrane properties in reverse electrodialysis. *Journal of Membrane Science* **2013**.
43. Post, J. W.; Goeting, C. H.; Valk, J.; Goinga, S.; Veerman, J.; Hamelers, H. V. M.; Hack, P., Towards implementation of reverse electrodialysis for power generation from salinity gradients. *Desalination and Water Treatment* **2010,** *16*, (1-3), 182-193.
44. Wilhelm, F. G.; van der Vegt, N. F. A.; Strathmann, H.; Wessling, M., Comparison of bipolar membranes by means of chronopotentiometry. *J Membrane Sci* **2002,** *199*, (1-2), 177-190.
45. Nagarale, R. K.; Gohil, G. S.; Shahi, V. K., Recent developments on ion-exchange membranes and electro-membrane processes. *Advances in Colloid and Interface Science* **2006,** *119*, (2-3), 97-130.
46. Elattar, A.; Elmidaoui, A.; Pismenskaia, N.; Gavach, C.; Pourcelly, G., Comparison of transport properties of monovalent anions through anion-exchange membranes. *J Membrane Sci* **1998,** *143*, (1-2), 249-261.
47. Volodina, E.; Pismenskaya, N.; Nikonenko, V.; Larchet, C.; Pourcelly, G., Ion transfer across ion-exchange membranes with homogeneous and heterogeneous surfaces. *J Colloid Interf Sci* **2005,** *285*, (1), 247-258.
48. Sata, T., *Ion Exchange Membranes: Preparation, Characterization, Modification and Application*. The Royal Society of Chemistry: Cambridge, UK, 2004.

49. Vermaas, D. A.; Saakes, M.; Nijmeijer, K., Doubled Power Density from Salinity Gradients at Reduced Intermembrane Distance. *Environmental Science & Technology* **2011,** *45*, (16), 7089-7095.
50. Feldheim, D. L., Lawson, Del R., and Martin, Charles R., Influence of the sulfonate countercation on the thermal stability of Nafion perfluorousulfonate membranes. *Journal of Polymer Science: Part B: Polymer Physics* **1993,** *31*, (8), 953-957.
51. Brandon, N. P.; Skinner, S.; Steele, B. C. H., Recent advances in materials for fuel cells. *Annu Rev Mater Res* **2003,** *33*, 183-213.
52. Kontturi, K., Murtomäki, L., Manzanares, J. A., *Ionic Transport Processes in Electrochemistry and Membrane Science*. Oxford University Press: 2008.
53. Strathmann, H., *Ion-exchange membrane separation processes*. Elsevier Science Limited: 2004; Vol. 9.
54. Strathmann, H.; ScienceDirect (Online service), Ion-exchange membrane separation processes. In *Membrane science and technology series,*, 1st ed.; Elsevier,: Amsterdam ; Boston, 2004; pp xi, 348 p.
55. Helfer, F.; Lemckert, C.; Anissimov, Y. G., Osmotic power with Pressure Retarded Osmosis: Theory, performance and trends - A review. *J Membrane Sci* **2014,** *453*, 337-358.
56. Koter, S.; Piotrowski, P.; Kerres, J., Comparative investigations of ion-exchange membranes. *J Membrane Sci* **1999,** *153*, (1), 83-90.
57. Geise, G. M.; Hickner, M. A.; Logan, B. E., Ionic Resistance and Permselectivity Tradeoffs in Anion Exchange Membranes. *Acs Applied Materials & Interfaces* **2013,** *5*, (20), 10294-10301.
58. Klaysom, C.; Moon, S. H.; Ladewig, B. P.; Lu, G. Q. M.; Wang, L. Z., Preparation of porous ion-exchange membranes (IEMs) and their characterizations. *J Membrane Sci* **2011,** *371*, (1-2), 37-44.
59. Galama, A. H.; Post, J. W.; Stuart, M. A. C.; Biesheuvel, P. M., Validity of the Boltzmann equation to describe Donnan equilibrium at the membrane-solution interface. *J Membrane Sci* **2013,** *442*, 131-139.
60. Kumar, M.; Singh, S.; Shahi, V. K., Cross-Linked Poly(vinyl alcohol)-Poly(acrylonitrile-co-2-dimethylamino ethylmethacrylate) Based Anion-Exchange Membranes in Aqueous Media. *J Phys Chem B* **2010,** *114*, (1), 198-206.
61. Khare, A. R.; Peppas, N. A., Swelling Deswelling of Anionic Copolymer Gels. *Biomaterials* **1995,** *16*, (7), 559-567.
62. Strathmann, H.; Grabowski, A.; Eigenberger, G., Ion-Exchange Membranes in the Chemical Process Industry. *Ind Eng Chem Res* **2013,** *52*, (31), 10364-10379.
63. Nouri, S.; Dammak, L.; Bulvestre, G.; Auclair, B., Comparison of three methods for the determination of the electrical conductivity of ion-exchange polymers. *European Polymer Journal* **2002,** *38*, (9), 1907-1913.
64. Geise, G. M.; Curtis, A. J.; Hatzell, M. C.; Hickner, M. A.; Logan, B. E., Salt Concentration Differences Alter Membrane Resistance in Reverse Electrodialysis Stacks. *Environmental Science & Technology Letters* **2013,** *1*, (1), 36-39.
65. Dlugolecki, P.; Anet, B.; Metz, S. J.; Nijmeijer, K.; Wessling, M., Transport limitations in ion exchange membranes at low salt concentrations. *J Membrane Sci* **2010,** *346*, (1), 163-171.

66. Dlugolecki, P.; Ogonowski, P.; Metz, S. J.; Saakes, M.; Nijmeijer, K.; Wessling, M., On the resistances of membrane, diffusion boundary layer and double layer in ion exchange membrane transport. *J Membrane Sci* **2010,** *349*, (1-2), 369-379.
67. Galama, A. H.; Vermaas, D. A.; Veerman, J.; Saakes, M.; Rijnaarts, H. H. M.; Post, J. W., Membrane resistance: the effect of salinity gradients over a cation exchange membrane. *J Membrane Sci* **2014,** *467*, 279-291.
68. Sistat, P.; Pourcelly, G., Chronopotentiometric response of an ion-exchange membrane in the underlimiting current-range. Transport phenomena within the diffusion layers. *J Membrane Sci* **1997,** *123*, (1), 121-131.
69. Audinos, R.; Pichelin, G., Characterization of Electrodialysis Membranes by Chronopotentiometry. *Desalination* **1988,** *68*, (2-3), 251-263.
70. Moya, A. A.; Sistat, P., Chronoamperometric response of ion-exchange membrane systems. *J Membrane Sci* **2013,** *444*, 412-419.
71. Park, J. S.; Choi, J. H.; Woo, J. J.; Moon, S. H., An electrical impedance spectroscopic (EIS) study on transport characteristics of ion-exchange membrane systems. *J Colloid Interf Sci* **2006,** *300*, (2), 655-662.
72. Karpenko, L. V.; Demina, O. A.; Dvorkina, G. A.; Parshikov, S. B.; Larchet, C.; Auclair, B.; Berezina, N. P., Comparative study of methods used for the determination of electroconductivity of ion-exchange membranes. *Russian Journal of Electrochemistry* **2001,** *37*, (3), 287-293.
73. Nikonenko, V. V.; Kozmai, A. E., Electrical equivalent circuit of an ion-exchange membrane system. *Electrochimica Acta* **2011,** *56*, (3), 1262-1269.
74. Helfferich, F. G., *Ion exchange*. McGraw-Hill: New York,, 1962; p 624 p.
75. Veerman, J.; Post, J. W.; Saakes, M.; Metz, S. J.; Harmsen, G. J., Reducing power losses caused by ionic shortcut currents in reverse electrodialysis stacks by a validated model. *J Membrane Sci* **2008,** *310*, (1–2), 418-430.
76. Grabowski, A.; Zhang, G. Q.; Strathmann, H.; Eigenberger, G., The production of high purity water by continuous electrodeionization with bipolar membranes: Influence of the anion-exchange membrane permselectivity. *J Membrane Sci* **2006,** *281*, (1-2), 297-306.
77. Strathmann, H., Electrodialysis, a mature technology with a multitude of new applications. *Desalination* **2010,** *264*, (3), 268-288.
78. Zhang, M.; Kim, H. K.; Chalkova, E.; Mark, F.; Lvov, S. N.; Chung, T. M., New polyethylene based anion exchange membranes (PE–AEMs) with high ionic conductivity. *Macromolecules* **2011,** *44*, (15), 5937-5946.
79. Xu, T. W., Ion exchange membranes: State of their development and perspective. *J Membrane Sci* **2005,** *263*, (1-2), 1-29.
80. Gupta, B. D.; Chapiro, A., Preparation of ion-exchange membranes by grafting acrylic acid into pre-irradiated polymer films—2. Grafting into teflon-FEP. *European Polymer Journal* **1989,** *25*, (11), 1145-1148.
81. Aouadj, S.; Chapiro, A., Preparation of hydrophilic membranes by grafting acrylic acid onto pre-irradiated teflon-FEP films. *Die Angewandte Makromolekulare Chemie* **1996,** *235*, (1), 73-80.
82. Hegazy, E. S. A.; Taher, N.; Ebaid, A., Preparation and some properties of hydrophilic membranes obtained by radiation grafting of methacrylic acid onto fluorinated polymers. *Journal of applied polymer science* **1990,** *41*, (11-12), 2637-2647.

83. Saito, K.; Saito, K.; Sugita, K.; Tamada, M.; Sugo, T., Convection-aided collection of metal ions using chelating porous flat-sheet membranes. *Journal of Chromatography A* **2002,** *954*, (1–2), 277-283.
84. Xu, T. W.; Yang, W. H.; He, B. L., Effect of solvent composition on the sulfonation degree of poly(phenylene oxide) (PPO). *Chinese Journal of Polymer Science* **2002,** *20*, (1), 53-57.
85. Komkova, E. N.; Stamatialis, D. F.; Strathmann, H.; Wessling, M., Anion-exchange membranes containing diamines: preparation and stability in alkaline solution. *J Membrane Sci* **2004,** *244*, (1–2), 25-34.
86. Yee, R. S. L.; Rozendal, R. A.; Zhang, K.; Ladewig, B. P., Cost effective cation exchange membranes: A review. *Chem. Eng. Res. Des.* **2012,** *90*, (7), 950-959.
87. Zhao, C.; Ma, W.; Sun, W.; Na, H., Preparation of anion exchange membrane based on homogeneous quaternization of bromomethylated poly (arylene ether sulfone). *Journal of Applied Polymer Science* **2013**.
88. Hibbs, M. R.; Fujimoto, C. H.; Cornelius, C. J., Synthesis and characterization of poly (phenylene)-based anion exchange membranes for alkaline fuel cells. *Macromolecules* **2009,** *42*, (21), 8316-8321.
89. Vinodh, R.; Ilakkiya, A.; Elamathi, S.; Sangeetha, D., A novel anion exchange membrane from polystyrene (ethylene butylene) polystyrene: synthesis and characterization. *Materials Science and Engineering: B* **2010,** *167*, (1), 43-50.
90. Herman, H.; Slade, R. C. T.; Varcoe, J. R., The radiation-grafting of vinylbenzyl chloride onto poly(hexafluoropropylene-co-tetrafluoroethylene) films with subsequent conversion to alkaline anion-exchange membranes: optimisation of the experimental conditions and characterisation. *J Membrane Sci* **2003,** *218*, (1–2), 147-163.
91. Sata, T.; Yamane, Y.; Matsusaki, K., Preparation and properties of anion exchange membranes having pyridinium or pyridinium derivatives as anion exchange groups. *Journal of Polymer Science Part A: Polymer Chemistry* **1998,** *36*, (1), 49-58.
92. Zhang, Q. G.; Liu, Q. L.; Zhu, A. M.; Xiong, Y.; Ren, L., Pervaporation performance of quaternized poly (vinyl alcohol) and its crosslinked membranes for the dehydration of ethanol. *J Membrane Sci* **2009,** *335*, (1), 68-75.
93. Sata, T.; Tsujimoto, M.; Yamaguchi, T.; Matsusaki, K., Change of anion exchange membranes in an aqueous sodium hydroxide solution at high temperature. *J Membrane Sci* **1996,** *112*, (2), 161-170.
94. Xu, T. W.; Wu, D.; Wu, L., Poly(2,6-dimethyl-1,4-phenylene oxide) (PPO)-A versatile starting polymer for proton conductive membranes (PCMs). *Progress in Polymer Science* **2008,** *33*, (9), 894-915.
95. Xu, T. W.; Yang, W. H.; He, B. L., Ionic conductivity threshold in sulfonated poly (phenylene oxide) matrices: a combination of three-phase model and percolation theory. *Chemical Engineering Science* **2001,** *56*, (18), 5343-5350.
96. Wu, Y.; Wu, C.; Xu, T.; Lin, X.; Fu, Y., Novel silica/poly(2,6-dimethyl-1,4-phenylene oxide) hybrid anion-exchange membranes for alkaline fuel cells: Effect of heat treatment. *J Membrane Sci* **2009,** *338*, (1-2), 51-60.
97. Wu, Y. H.; Hao, J. W.; Wu, C. M.; Mao, F. L.; Xu, T. W., Cation exchange PVA/SPPO/SiO2 membranes with double organic phases for alkali recovery. *J Membrane Sci* **2012,** *423*, 383-391.

98. Yang, C. C.; Chiu, S. J.; Chien, W. C.; Chiu, S. S., Quaternized poly(vinyl alcohol)/alumina composite polymer membranes for alkaline direct methanol fuel cells. *Journal of Power Sources* **2010,** *195*, (8), 2212-2219.
99. Siracusano, S.; Baglio, V.; Navarra, M.; Panero, S.; Antonucci, V.; Aricò, A., Investigation of Composite Nafion/Sulfated Zirconia Membrane for Solid Polymer Electrolyte Electrolyzer Applications. *International Journal of Electrochemical Science* **2012,** *7*, (2).
100. Yun, S.; Im, H.; Heo, Y.; Kim, J., Crosslinked sulfonated poly(vinyl alcohol)/sulfonated multi-walled carbon nanotubes nanocomposite membranes for direct methanol fuel cells. *J Membrane Sci* **2011,** *380*, (1-2), 208-215.
101. Zuo, X. T.; Yu, S. L.; Xu, X.; Bao, R. L.; Xu, J.; Qu, W. M., Preparation of organic-inorganic hybrid cation-exchange membranes via blending method and their electrochemical characterization. *J Membrane Sci* **2009,** *328*, (1-2), 23-30.
102. Wang, Z.; Tang, H. L.; Zhang, H. J.; Lei, M.; Chen, R.; Xiao, P.; Pan, M., Synthesis of Nafion/CeO2 hybrid for chemically durable proton exchange membrane of fuel cell. *J Membrane Sci* **2012,** *421*, 201-210.
103. Arsalan, M.; Khan, M. M. A.; Rafiuddin, A comparative study of theoretical, electrochemical and ionic transport through PVC based Cu-3(PO4)(2) and polystyrene supported Ni-3(PO4)(2) composite ion exchange porous membranes. *Desalination* **2013,** *318*, 97-106.
104. Sun, L. L.; Wang, S. L.; Jin, W.; Hou, H. Y.; Jiang, L. H.; Sun, G. Q., Nano-sized Fe2O3-SO42- solid superacid composite Nafion (R) membranes for direct methanol fuel cells. *International Journal of Hydrogen Energy* **2010,** *35*, (22), 12461-12468.
105. Hosseini, S. M.; Madaeni, S. S.; Heidari, A. R.; Amirimehr, A., Preparation and characterization of ion-selective polyvinyl chloride based heterogeneous cation exchange membrane modified by magnetic iron-nickel oxide nanoparticles. *Desalination* **2012,** *284*, 191-199.
106. Nagarale, R. K.; Shahi, V. K.; Rangarajan, R., Preparation of polyvinyl alcohol-silica hybrid heterogeneous anion-exchange membranes by sol-gel method and their characterization. *J Membrane Sci* **2005,** *248*, (1-2), 37-44.
107. Jeong, Y. G.; Park, H. S.; Seo, D. W.; Choi, S. W.; Kim, W. G., Nano Composite Membranes of Sulfonated Poly (2, 6-Dimethyl-1, 4-Phenylene Oxide)/Poly (2, 6-Diphenyl-1, 4-Phenylene Oxide) Copolymer and SiO2 for Fuel Cell Application. *Advanced Materials Research* **2007,** *26*, 835-838.
108. Nagarale, R. K.; Gohil, G. S.; Shahi, V. K.; Rangarajan, R., Organic-inorganic hybrid membrane: Thermally stable cation-exchange membrane prepared by the sol-gel method. *Macromolecules* **2004,** *37*, (26), 10023-10030.
109. Wang, F. H.; Lu, Z.; Zhu, H.; Zhang, X. W.; Guo, Z. J.; Wei, Y. S., Preparation and Characterization of Nafion/Sulfonated SiO2 Molecular Sieve Composite Membranes. *Composite Interfaces* **2011,** *18*, (3), 237-249.
110. Ke, C. C.; Li, X. J.; Shen, Q. A.; Qu, S. G.; Shao, Z. G.; Yi, B. L., Investigation on sulfuric acid sulfonation of in-situ sol-gel derived Nafion/SiO2 composite membrane. *International Journal of Hydrogen Energy* **2011,** *36*, (5), 3606-3613.
111. Kim, J. Y.; Mulmi, S.; Lee, C. H.; Park, H. B.; Chung, Y. S.; Lee, Y. M., Preparation of organic–inorganic nanocomposite membrane using a reactive polymeric

dispersant and compatibilizer: Proton and methanol transport with respect to nano-phase separated structure. *J Membrane Sci* **2006,** *283*, (1–2), 172-181.
112. Wu, C. M.; Xu, T. W.; Gong, M.; Yang, W. H., Synthesis and characterizations of new negatively charged organic-inorganic hybrid materials Part II. Membrane preparation and characterizations. *J Membrane Sci* **2005,** *247*, (1-2), 111-118.
113. Rahimpour, A.; Madaeni, S. S.; Taheri, A. H.; Mansourpanah, Y., Coupling TiO2 nanoparticles with UV irradiation for modification of polyethersulfone ultrafiltration membranes. *J Membrane Sci* **2008,** *313*, (1-2), 158-169.
114. Li, J. F.; Xu, Z. L.; Yang, H.; Yu, L. Y.; Liu, M., Effect of TiO2 nanoparticles on the surface morphology and performance of microporous PES membrane. *Applied Surface Science* **2009,** *255*, (9), 4725-4732.
115. Wu, Z.; Sun, G.; Jin, W.; Hou, H.; Wang, S.; Xin, Q., Nafion® and nano-size TiO2–SO42− solid superacid composite membrane for direct methanol fuel cell. *J Membrane Sci* **2008,** *313*, (1), 336-343.
116. Baglio, V.; Arico, A. S.; Di Blasi, A.; Antonucci, V.; Antonucci, P. L.; Licoccia, S.; Traversa, E.; Fiory, F. S., Nafion-TiO2 composite DMFC membranes: physico-chemical properties of the filler versus electrochemical performance. *Electrochimica Acta* **2005,** *50*, (5), 1241-1246.
117. Sairam, M.; Patil, M. B.; Veerapur, R. S.; Patil, S. A.; Aminabhavi, T. M., Novel dense poly(vinyl alcohol)-TiO2 mixed matrix membranes for pervaporation separation of water-isopropanol mixtures at 30 degrees C. *J Membrane Sci* **2006,** *281*, (1-2), 95-102.
118. Li, W.; Sun, X.; Wen, C.; Lu, H.; Wang, Z., Preparation and characterization of poly (vinylidene fluoride)/TiO2 hybrid membranes. *Frontiers of Environmental Science & Engineering* **2013,** *7*, (4), 492-502.
119. Pourjafar, S.; Rahimpour, A.; Jahanshahi, M., Synthesis and characterization of PVA/PES thin film composite nanofiltration membrane modified with TiO2 nanoparticles for better performance and surface properties. *Journal of Industrial and Engineering Chemistry* **2012,** *18*, (4), 1398-1405.
120. Apichatachutapan, W.; Moore, R.; Mauritz, K. A., Asymmetric nafion/(zirconium oxide) hybrid membranes via in situ sol-gel chemistry. *Journal of applied polymer science* **1996,** *62*, (2), 417-426.
121. Zhai, Y. F.; Zhang, H. M.; Hu, J. W.; Yi, B. L., Preparation and characterization of sulfated zirconia(SO42-/ZrO2)/Nafion composite membranes for PEMFC operation at high temperature/low humidity. *J Membrane Sci* **2006,** *280*, (1-2), 148-155.
122. Bottino, A.; Capannelli, G.; Comite, A., Preparation and characterization of novel porous PVDF-ZrO2 composite membranes. *Desalination* **2002,** *146*, (1-3), 35-40.
123. Sacca, A.; Gatto, I.; Carbone, A.; Pedicini, R.; Passalacqua, E., ZrO2–Nafion composite membranes for polymer electrolyte fuel cells (PEFCs) at intermediate temperature. *Journal of power sources* **2006,** *163*, (1), 47-51.
124. Navarra, M. A.; Abbati, C.; Croce, F.; Scrosati, B., Temperature-dependent Performances of a Fuel Cell Using a Superacid Zirconia-doped Nafion Polymer Electrolyte. *Fuel Cells* **2009,** *9*, (3), 222-225.
125. Długoł˛ecki, P.; Nymeijer, K.; Metz, S.; Wessling, M., Current status of ion exchange membranes for power generation from salinity gradients. *J Membrane Sci* **2008,** *319*, (1), 214-222.

126. Morf, W. E., *The principles of ion-selective electrodes and of membrane transport*. Elsevier New York:: 1981; Vol. 446, p 432.
127. *Clauser, C., Numerical simulation of reactive flow in hot aquifers*. Springer: *2003*; Vol. 9.
128. Ling, L. P.; Leow, H. F.; Sarmidi, M. R., Citric acid concentration by electrodialysis: ion and water transport modelling. *J Membrane Sci* **2002,** *199*, (1), 59-67.
129. Sadrzadeh, M.; Mohammadi, T., Treatment of sea water using electrodialysis: Current efficiency evaluation. *Desalination* **2009,** *249*, (1), 279-285.
130. Nightingale Jr, E., Phenomenological theory of ion solvation. Effective radii of hydrated ions. *The Journal of Physical Chemistry* **1959,** *63*, (9), 1381-1387.
131. Weast, R. C.; Astle, M. J.; Beyer, W. H., *CRC handbook of chemistry and physics*. CRC press Boca Raton, FL: 1988; Vol. 69.
132. Samson, E.; Marchand, J.; Snyder, K., Calculation of ionic diffusion coefficients on the basis of migration test results. *Materials and Structures* **2003,** *36*, (3), 156-165.
133. Vermaas, D. A.; Saakes, M.; Nijmeijer, K., Power generation using profiled membranes in reverse electrodialysis. *J Membrane Sci* **2011,** *385-386*, 234-242.
134. Luo, X.; Cao, X.; Mo, Y.; Xiao, K.; Zhang, X.; Liang, P.; Huang, X., Power generation by coupling reverse electrodialysis and ammonium bicarbonate: Implication for recovery of waste heat. *Electrochemistry Communications* **2012,** *19*, 25-28.
135. Wu, D.; Wu, L.; Woo, J. J.; Yun, S. H.; Seo, S. J.; Xu, T. W.; Moon, S. H., A simple heat treatment to prepare covalently crosslinked membranes from sulfonated poly(2,6-dimethyl-1,4-phenylene oxide) for application in fuel cells. *J Membrane Sci* **2010,** *348*, (1-2), 167-173.
136. Yu, H.; Xu, T. W., Fundamental studies of homogeneous cation exchange membranes from poly(2,6-dimethyl-1,4-phenylene oxide): Membranes prepared by simultaneous aryl-sulfonation and aryl-bromination. *Journal of Applied Polymer Science* **2006,** *100*, (3), 2238-2243.
137. Kruczek, B.; Matsuura, T., Development and characterization of homogeneous membranes de from high molecular weight sulfonated polyphenylene oxide. *J Membrane Sci* **1998,** *146*, (2), 263-275.
138. Khodabakhshi, A.; Madaeni, S.; Xu, T.; Wu, L.; Wu, C.; Li, C.; Na, W.; Zolanvari, S.; Babayi, A.; Ghasemi, J., Preparation, optimization and characterization of novel ion exchange membranes by blending of chemically modified PVDF and SPPO. *Separation and Purification Technology* **2012,** *90*, 10-21.
139. Magnacca, G.; Cerrato, G.; Morterra, C.; Signoretto, M.; Somma, F.; Pinna, F., Structural and surface characterization of pure and sulfated iron oxides. *Chemistry of Materials* **2003,** *15*, (3), 675-687.
140. Colomer, M. T.; Zenzinger, K., Mesoporous alpha-Fe2O3 membranes as proton conductors: Synthesis by microwave-assisted sol-gel route and effect of their textural characteristics on water uptake and proton conductivity. *Microporous and Mesoporous Materials* **2012,** *161*, 123-133.
141. Hasanabadi, N.; Ghaffarian, S. R.; Hasani-Sadrabadi, M. M., Magnetic field aligned nanocomposite proton exchange membranes based on sulfonated poly (ether sulfone) and Fe2O3 nanoparticles for direct methanol fuel cell application. *International Journal of Hydrogen Energy* **2011,** *36*, (23), 15323-15332.

142. Gu, B.; Schmitt, J.; Chen, Z.; Liang, L.; McCarthy, J. F., Adsorption and desorption of natural organic matter on iron oxide: mechanisms and models. *Environmental science & technology* **1994,** *28*, (1), 38-46.
143. Sabbatini, P.; Yrazu, F.; Rossi, F.; Thern, G.; Marajofsky, A.; Fidalgo de Cortalezzi, M., Fabrication and characterization of iron oxide ceramic membranes for arsenic removal. *Water research* **2010,** *44*, (19), 5702-5712.
144. Karnik, B. S.; Davies, S. H.; Baumann, M. J.; Masten, S. J., Fabrication of catalytic membranes for the treatment of drinking water using combined ozonation and ultrafiltration. *Environmental science & technology* **2005,** *39*, (19), 7656-7661.
145. Honghai, W.; Yiying, L.; Jiayi, W.; Lixuan, Z.; Dingcai, Z.; Juan, D., Surface adsorption of iron oxide minerals for phenol and dissolved organic matter. *Earth Science Frontiers* **2008,** *15*, (6), 133-141.
146. Harman, B. I.; Koseoglu, H.; Yigit, N. O.; Beyhan, M.; Kitis, M., The use of iron oxide-coated ceramic membranes in removing natural organic matter and phenol from waters. *Desalination* **2010,** *261*, (1-2), 27-33.
147. Hong, J. G.; Zhang, W.; Luo, J.; Chen, Y., Modeling of power generation from the mixing of simulated saline and freshwater with a reverse electrodialysis system: The effect of monovalent and multivalent ions. *Applied Energy* **2013,** *110*, 244-251.
148. Wijers, M.; Jin, M.; Wessling, M.; Strathmann, H., Supported liquid membranes modification with sulphonated poly (ether ether ketone): permeability, selectivity and stability. *J Membrane Sci* **1998,** *147*, (1), 117-130.
149. Park, Y. I.; Piao, Y.; Lee, N.; Yoo, B.; Kim, B. H.; Choi, S. H.; Hyeon, T., Transformation of hydrophobic iron oxide nanoparticles to hydrophilic and biocompatible maghemite nanocrystals for use as highly efficient MRI contrast agent. *Journal of Materials Chemistry* **2011,** *21*, (31), 11472-11477.
150. Klaysom, C.; Marschall, R.; Moon, S. H.; Ladewig, B. P.; Lu, G. Q. M.; Wang, L. Z., Preparation of porous composite ion-exchange membranes for desalination application. *Journal of Materials Chemistry* **2011,** *21*, (20), 7401-7409.
151. Choi, J. H.; Moon, S. H., Pore size characterization of cation-exchange membranes by chronopotentiometry using homologous amine ions. *J Membrane Sci* **2001,** *191*, (1-2), 225-236.
152. Klaysom, C.; Germain, L.; Burr, S.; Ladewig, B. P.; Wang, L. Z.; Da Costa, J. D.; Lu, G. Q. M., Preparation of new composite membranes for water desalination using electrodialysis. In *Smart Materials V*, Voelcker, N. H.; Thissen, H. W., Eds. 2008; Vol. 7267.
153. Colomer, M. T.; Zenzinger, K., Mesoporous alpha-Fe2O3 membranes as proton conductors: Synthesis by microwave-assisted sol-gel route and effect of their textural characteristics on water uptake and proton conductivity. *Microporous and Mesoporous Materials 161*, 123-133.
154. Gohil, G. S.; Binsu, V. V.; Shahi, V. K., Preparation and characterization of mono-valent ion selective polypyrrole composite ion-exchange membranes. *J Membrane Sci* **2006,** *280*, (1-2), 210-218.
155. Gui, L.; Wang, H.; Shentu, B.; Weng, Z., Synthesis and characterization of low-molecular-weight poly(2,6-dimethyl-1,4-phenylene oxide) in water. *Journal of Applied Polymer Science* **2012,** *128*, (5), 2919-2926.

156. Huang, R. Y. M.; Kim, J. J., Synthesis and transport-properties of thin-film composite membranes .1. Synthesis of poly(phenylene oxide) polymer and its sulfonation. *Journal of Applied Polymer Science* **1984,** *29*, (12), 4017-4027.
157. Wang, M.; Wu, L.-G.; Mo, J.-X.; Gao, C.-J., The preparation and characterization of novel charged polyacrylonitrile/PES-C blend membranes used for ultrafiltration. *J Membrane Sci* **2006,** *274*, (1), 200-208.
158. Sollner, K., An outline of the basic electrochemistry of porous membranes. *Journal of dental research* **1974,** *53*, (2), 267-279.
159. Jones, L.; Pintauro, P. N.; Tang, H., Coion exclusion properties of polyphosphazene ion-exchange membranes. *J Membrane Sci* **1999,** *162*, (1), 135-143.
160. Dlugolecki, P.; Ogonowski, P.; Metz, S. J.; Saakes, M.; Nijmeijer, K.; Wessling, M., On the resistances of membrane, diffusion boundary layer and double layer in ion exchange membrane transport. *J Membrane Sci* **2010,** *349*, (1), 369-379.
161. Wilhelm, M.; Jeske, M.; Marschall, R.; Cavalcanti, W. L.; Tölle, P.; Köhler, C.; Koch, D.; Frauenheim, T.; Grathwohl, G.; Caro, J.; Wark, M., New proton conducting hybrid membranes for HT-PEMFC systems based on polysiloxanes and SO3H-functionalized mesoporous Si-MCM-41 particles. *J Membrane Sci* **2008,** *316*, (1–2), 164-175.
162. Berezina, N. P.; Kononenko, N. A.; Dyomina, O. A.; Gnusin, N. P., Characterization of ion-exchange membrane materials: Properties vs structure. *Advances in Colloid and Interface Science* **2008,** *139*, (1–2), 3-28.
163. Nalwa, H. S., Handbook of organic-inorganic hybrid materials and nanocomposites. **2003**.
164. Gomes, D.; Marschall, R.; Nunes, S. P.; Wark, M., Development of polyoxadiazole nanocomposites for high temperature polymer electrolyte membrane fuel cells. *J Membrane Sci* **2008,** *322*, (2), 406-415.
165. Shammas, N. K.; Wang, L. K.; Hung, Y.-T., *Advanced Physicochemical Treatment Processes*. Humana Press: 2006.